Stereotactic Radiation Treatment of Lung Cancer by VMAT.

Johanna Austrheim Hundvin

NORWEGIAN UNIVERSITY OF SCIENCE AND
TECHNOLOGY, NTNU

MASTER'S THESIS

Stereotactic Radiotherapy
of Lung Cancer by VMAT

Norwegian Title:
STEREOTAKTISK STRÅLEBEHANDLING AV KREFT I LUNGE VED BRUK AV VMAT

Supervisors:
Pål Erik Goa
Marcin Paweł Sikora
Tone Nybø

Author:
Johanna Austrheim Hundvin

June 25, 2015

Preface

This thesis is written during the spring semester of 2015, as the completion of my Master's Degree in Biophysics and medical technology at the Norwegian University of Science and Technology (NTNU). The work has been performed in cooperation with Haukeland University Hospital (HUH) in Bergen.

Abstract

Radiotherapy of early stage non-small cell lung cancer (NSCLC) is a challenging treatment due to the varying tissue densities in the irradiated volume and the moving target. At Haukeland University Hospital (HUH) the treatment is performed by stereotactic body radiotherapy (SBRT) using the conventional technique with flattening filter (FF) included. Advances in treatment planning and delivery facilitates the use of volumetric arc modulated therapy (VMAT) with the flattening filter removed, with the potential of a more conformal dose distribution, elevated target dose for increased tumour control and shorter delivery time. However, the requirement of clinical dose accuracy is crucial for the treatment outcome, and has to be taken into account with the utmost care. The aim of this study is to establish a method for robust SBRT treatment of NSCLC using the FFF VMAT technique.

Five patients with NSCLC earlier treated with SBRT at HUH have been used as patient material of the investigation. The patients had prescribed doses of 54 or 55 Gy, tumours with a craniocaudal motion larger than 5 mm and an ITV size in the range of 1.7 cm^3 to 58.6 cm^3. The Analytical Anisotropic Algorithm (AAA) have been evaluated in comparison to a newly developed in-house Monte Carlo (MC) algorithm using phantom simulations and measurements on the *Delta4* phantom (ScandiDos AB, Uppsala, Sweden). Three different CT bases have been used in the treatment planning process (*MIP*, *AI* and *density overwrite*). For each patient, FFF VMAT treatments plans with energy of 6 MV and 10MV were generated in $Eclipse^{TM}$ by AAA for each of the three CT bases, resulting in six new plans per patient. All plans were then recalculated by the MC algorithm. For verification, the MC dose of each phase of the 4D CT scan was accumulated using a deformable registration program (*Matcher3D*) developed by Söhn et. al. [47].

The 6 MV FFF and 10 MV FFF beams showed good agreement in water density, with symmetric errors up to 2 % relative to the maximum dose. The AAA density handling in homogeneous matter was suitable, while heterogeneous media lead to prominent deviations due to the lateral electronic disequilibrium (LED) effect. The deviation between the AAA and MC calculated dose distributions tended to increase with increasing energy. The density overwrite basis lead to good correspondence between the AAA and MC calculated dose distributions, but resulted in remarkably deviations between the planned and accumulated doses. For the MIP and AI CT bases, the deviation between planned and accumulated dose was smaller, in addition to an in general smaller variation. The largest tumours investigated showed to have results best predicted by the planning algorithm. For the smallest tumour evaluated with an ITV volume of 1.7 cm^3 none of the bases gave adequate results, and planning optimisation by MC instead of AAA is recommended.

The method of robust SBRT NSCLC FFF VMAT treatment planning and verification still needs further developments of the MC algorithm, in addition to automated procedure steps for time reduction. The FFF VMAT treatment of NSCLC lead to dose distributions of higher conformity index, higher target dose and lower dose to adjacent tissue than then conventional treatments, validated by MC calculations and dose accumulation.

Sammendrag

Strålebehandling av tidlige stadier av ikke-småcellet lungekreft (NSCLC) er en avansert behandling grunnet den varierende vevstettheten i det bestrålte volumet og et målvolum i bevegelse. Ved Haukeland Universitetssykehus (HUS) utføres behandlingen i dag ved bruk av stereotaktisk (SBRT) 3D-konform stråleterapi (3D-CRT) med flathetsfilter inkludert. Utvikling innen behandlingsplanlegging og doselevering har muliggjort bruken av flathetsfilterfri (FFF) volumetrisk modulert stråleterapi (VMAT), som har potensial til å øke konformiteten til dosefordelingen, redusere bestrålingstiden og øke målvolumdosen. Dette kan innebære økt tumorkontroll og bedre behandlingsresultat. Imidlertid er det viktig å understreke at behandlingen er helt avhengig av presisjonen til den kliniske dosen for å oppnå det ønskede resultatet. Målet med dette studiet er å etablere en metode for robust behandling av NSCLC ved bruke av SBRT FFF VMAT teknikk.

Fem pasienter med NSCLC tidligere behandlet ved bruk av SBRT ved HUS ble brukt som pasientgrunnlag for undersøkelsen. Pasientene hadde mottatt behandlinger med foreskrevet dose satt til enten 54 eller 55 Gy. Alle tumorer hadde en craniocaudal bevegelse på mer enn 5 med mer og et ITV på mellom 1.7 cm^3 of 58.6 cm^3. Den Analystisk Anisotropisk Algoritme (AAA) brukt for doseberegning i planbehandlingssystemet $Eclipse^{TM}$ ble evaluert med hensyn til en nylig utviklet Monte Carlo (MC) algoritme ved bruk av fantomsimuleringer og målinger på $Delta4$ fantomet (ScandiDos AB, Uppsala, Sweden). Tre forskjellige CT grunnlag ble brukt i behandlingsplanleggingsprosessen (*MIP*, *AI* og *density overwrite*(basis basert på tetthetsoverskriving)). FFF VMAT behandlingsplaner med energi på 6 MV og 10 MV ble generert i $Eclipse^{TM}$ for hvert av de tre CT grunnlagene for hver pasient, dvs. seks nye planer per pasient. Alle planer ble så rekalkulert med MC algoritmen. For å verifisere planene ble MC dosen beregnet for hver fase av 4D CT settet akkumulert ved hjelp av et deformasjonsregistreringsprogram (*Matcher3D*) utviklet av Söhn et. al. [47].

6 MV FFF og 10 MV FFF strålene viste god overensstemmelse i vanntetthet, med symmetriske feil opp til 2 % relativt til maksiumsdosen. Håndteringen av tetthet i homogent materie viste tilfredsstillende resultater for AAA, mens heterogent medium førte til tydelige forskjeller mellom AAA og MC grunnet mangel på lateral elektronlikevekt. Forskjellen mellom AAA og MC beregnede doser hadde en tendens til å øke med økende energi. *Density overwrite* CT-grunnlaget førte til samsvarende AAA og MC dosefordelinger, men resulterte i store avvik mellom planlagt og akkumulert dose. De største tumorene som ble undersøkt viste simuleringsresultatene som samsvarte mest med planlagt dose for både MIP og AI CT-grunnlaget. For den minste tumoren undersøkt i studiet, med et ITV volum på 1.7 cm ^{3}, gav ingen av CT-grunnlagene tilfredsstillende resultater. En løsning på dette problemet kan være å bruke MC algoritmen for å optimere planen i stedet for AAA.

Metoden for robust SBRT NSCLC FFF VMAT behandlingsplanlegging og verifikasjon har fremdeles behov for videre utvikling av MC algoritmen, i tillegg til flere automatiserte steg under prosedyren for å minke tidsforbruket. SBRT FFF VMAT behandling av NSCLC førte til dosefordelinger med høyere konformitetsindeks, høyere måldose og lavere dose til nærliggende vev enn hva de konvensjonelle planene presterte, hvor resultatene er validert ved bruk av MC beregninger og doseakkumulering.

Contents

List of Central Abbreviations

3D-CRT   3D Conformal Radiotherapy, page 7

AAA   Analytical Anisotropic Algorithm, page 13

AI   Averaged Intensity, page 12

CPE   Charged Particle Equilibrium, page 15

CT   Computed tomography, page 11

CTV   Clinical target volume, page 9

DO   Density Override, page 12

DTA   Distance to agreement, page 16

DVH   Dose-Volume Histogram, page 9

EGS   Electron Gamma Shower, page 23

FF   Flattening filter, page 5

FFF   Flattening filter free, page 5

FSU   Functional subunit, page 8

GTV   Gross tumour volume, page 9

HUH   Haukeland University Hospital, page 1

ITV   Internal target volume, page 9

LED   Lateral Electronic Disequilibrium, page 15

Linac   Linear accelerator, page 3

MC   Monte Carlo, page 14

MIP   Maximum Intensity Projection, page 12

MLC   Multileaf collimator, page 5

NSCLC   Non-small cell lung carcinoma, page 1

OAR   Organ at risk, page 9

PRV   Planning OAR volume, page 9

PTV   Planning target volume, page 9

SBRT   Stereotactic Body Radiotherapy, page 7

SSD   Source-Surface-Distance, page 22

TERMA   Total Energy Released per Mass, page 13

TPS   Treatment Planning System, page 8

VMAT   Volumetric modulated arc therapy, page 7

1 Introduction

Worldwide, lung cancer is the most common cancer in men and the third most common in women. Due to a low survival rate, incidence rates have similar patterns as the tendencies of mortality, irrespective of level of resource within a given country (2012). Historically, small cell lung carcinoma has been distinguished from non-small cell lung carcinoma (NSCLC), however, lung cancers are increasingly classified due to further insight in genetics and therapy responses [45].

Increased radiation dose improve tumour control, i.e. cancer cell death caused by radiation. However, concerns about radiation-induced injury to organs at risk (OARs) limits the high doses per treatment. During the last years, technical advancements in highly conformal treatment planning, image-guided radiotherapy, and delivery technologies have enabled a safer delivery of very large fractional doses of radiation, though further improvements are still requested [23].

Compared to the standard treatment, stereotactic body radiotherapy (SBRT) of lung cancer have the potential of increasing the survival rate for in-operable early stage cancer cases[49]. In addition, using RapidArc (Varian Medical Systems, Palo Alto, CA), which is a type of volumetric modulated arc therapy (VMAT), the delivery time of lung SBRT can be significantly reduced compared with static 3-dimensional conformal radiotherapy (3D-CRT) or intensity modulated radiotherapy (IMRT)[31]. Removing the flattening filter (FF) in the treatment apparatus enable the use of higher dose rates, which is another possibility of reducing the treatment time [52]. Especially for small fields along the central axis (CAX), commonly met in SBRT, the removal of the FF can be advantageous, as the dosimetric properties remains the same while the dose rate can be considerably elevated [32]. At Haukeland University Hospital (HUH) 3D-CRT is currently used for SBRT of NSCLC, but the aim is to implement VMAT with FFF beams during 2015. This requires establishing a method for both planning and verification of the treatment. Organ motion combined with large tissue heterogeneities in the thorax make this challenging. Planning is usually based on a static CT basis generated from a fast CT at exhalation and/or a 4D CT of the patient. Modifying the density of the static CT based on the 4D-CTs has shown to give a more realistic final dose distribution that might enhance the predictability and conformity of the treatment[54]. The aim of the current project was thus to investigate the use of different CT bases at planning and compare these with the static exhale CT which is currently used clinically for these patients.

In order to compare the different planning strategies, a method to account for tissue hetergeneities and organ motion in verification of the planned treatments had to be established. HUH uses $Eclipse^{TM}$ as treatment planning system (TPS), including a 3D pencil beam convolution superposition algorithm, Analytical Anisotropic Algorithm (AAA), as intermediate dose optimiser. Regarding the heterogeneities in the lung area, a more time demanding Monte Carlo (MC) algorithm can improve the accuracy of the dose calculation[37]. Previous to the current project, an in-house MC algorithm had been developed for this purpose. The aim of the current project was to benchmark and apply this algorithm to verify uncertainties caused by inaccurate modelling of tissue heterogeneities by AAA [29].

To account for organ motion in treatment verification it is relevant to estimate the dose accumulated over all breathing phases of a 4D-CT. This requires both deformable registration of corresponding anatomical points and summing of dose to these points. A method based on the work by Söhn et al. [47] had been implemented prior to this project. This method was tested and employed within the current project. As the procedures to obtain our aims has not been performed at HUH before, method development has been a major part of the study.

2 Theory

The fundamental idea of radiotherapy is to destroy the tumour cells by ionising radiation without causing intolerable damage to adjacent normal tissues [11]. The *therapeutic ratio* describes the relationship between tumour control probability and normal tissue complication probability (figure 2.1), and the continuous development within the field of radiotherapy seeks to maximise this ratio.
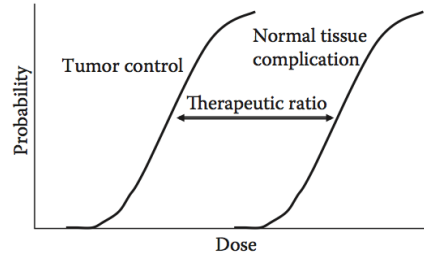
Figure 2.1: Therapeutic ratio [11].

In the following a general explanation of the radiation physics and biological effects related to radiotherapy will be presented, as well as a description of important aspects concerning dose planning and verification.

2.1 The linear accelerator

A *linear accelerator* (linac) is utilised in external radiotherapy to produce the therapeutic radiation. The device accelerates charged particles, such as electrons, to high energies through a linear tube using high-frequency electromagnetic waves. For superficial tumours the high-energy electron beam itself irradiates the patient. When treating deep-seated tumours, the irradiation beam consists of X-rays, produced by impinging the electrons on a target [21]. There are several types of linear accelerators, where typical components are illustrated in figure 2.2 and a design is shown in figure 2.3.
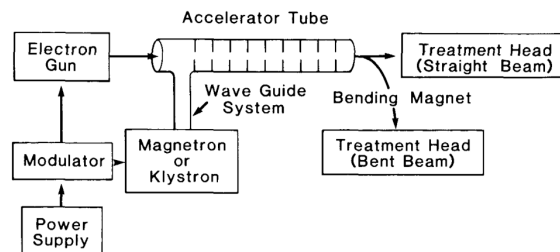
Figure 2.2: A block diagram of the typical components of a linac [21].

3
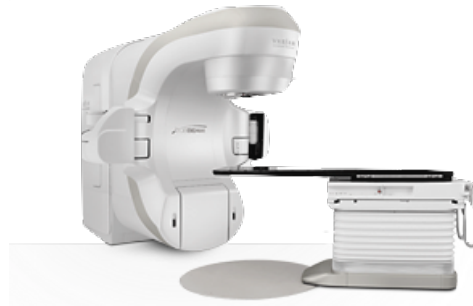
Figure 2.3: Linear accelerator and treatment couch produced by Varian Medical Systems (from official web-site).

2.1.1 The X-ray Beam

The X-rays exiting the treatment head of the linac are bremsstrahlung radiation beams produced due to the interaction between the electrons and the target, which is composed of a high-Z material such as tungsten. The process of bremsstrahlung involves a high-speed electron that interact with a nucleus, illustrated in figure 2.4a. When the electron passes near a nucleus, Coulomb forces of attraction may deflect the electron's path, which subsequently loses a part or all of its energy in the form of an electromagnetic radiation named bremsstrahlung. As the electron may have more than one interaction in the material, the energy of the striking electron is converted into a spectrum of X-ray energies with a possible maximum energy equal to its initial energy. Hence, while the electron energy can be discretely designated with MeV, the unit of the heterogeneous X-ray energy spectrum is MV, which is the potential of the electric field accelerating the electrons. However, even though a 10 MV linac has the potential to produce photons with energies up to 10 MeV, the average photon energy of the beam is only approximately one third of the maximum energy. Further, the direction of the resulting bremsstrahlung beam depends on the energy of the incoming electrons. The higher kinetic energy of the electrons, the more forward peaked the X-ray emission will be, illustrated in figure 2.4b [21].
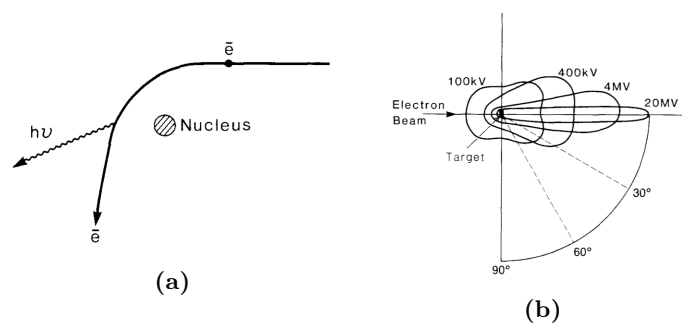
Figure 2.4: Illustration of (a) the characteristics of bremsstrahlung and (b) the spatial distribution of X-rays around a thin target [21].

2.1.2 The Flattening Filter

The generation of X-ray beams takes place in the treatment head, whose components are illustrated in figure 2.5. When the X-rays are heading towards the patient, several collimators and wedges

are shaping the beam to fit the structure of the desired volume to be irradiated, while an ion chamber monitors the dose rate, integrated dose, and field symmetry. The *multileaf collimator* (MLC) is a common type of collimation, where a large number of collimating blocks or leaves can be driven automatically and independently of each other to generate a field of the desired irregular shape [21]. In addition, "jaw tracking" can be applied to support the MLC leaves by giving extra shielding where the MLC leaves are closed over a rectangular area. Further, a *flattening filter* (FF) can be utilised to make the beam intensity uniform across the field, illustrated in figure 2.6 (recall figure 2.4b). Conventionally, such cone-shaped FFs was used to flatten the energy fluence across the field for simple dose calculation algorithms based on look-up table. However, improved treatment planning systems (TPSs) allows precise modelling of the unflattened beams and several papers indicate that *flattening filter free* (FFF) treatments are beneficial concerning dose rate, scattered radiation, and dose delivery time [10] [16] [30] [52].
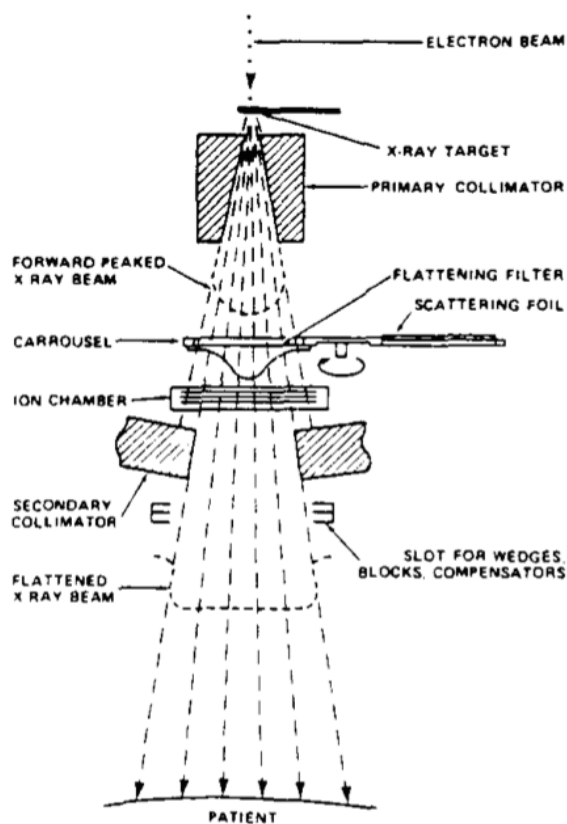
Figure 2.5: Components of the treatment head [21].

Figure 2.7 shows typical FFF beams for four different fields sizes, all measured at 10 cm depth. The coloured numbers indicate the peak ratio, defined as the dose difference between the maximum dose and the dose at 80 % of the respective field size. The graph clearly illustrates how the 10 MV beam results in a steeper or more forward peaked beam profile than the 6 MV beam [16].
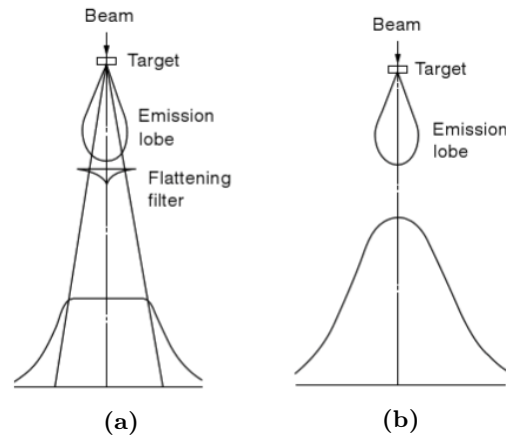
Figure 2.6: Intensity curve of a beam from a linear accelerator (a) with and (b) without a flattening filter [26].
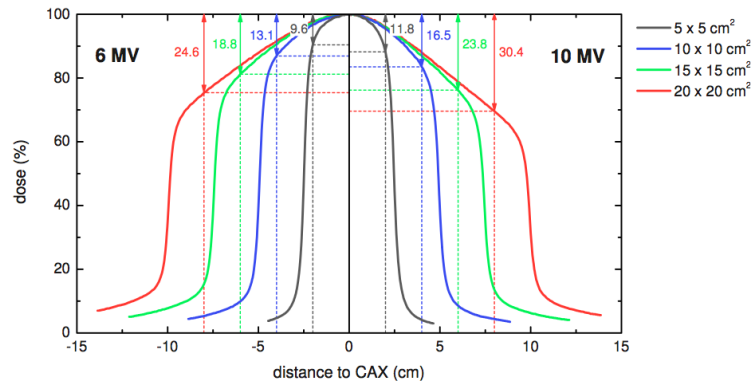
Figure 2.7: Beam profile, comparing FFF 6 MV and 10 MV beams for various field sizes. The coloured numbers are the peak ratios [16].

Beam Quality

To describe the radiation, the *beam quality* can be defined in various ways. For energies in the keV range, it can be defined as the beam's ability to penetrate matter. In the case of MeV radiation beams, an *ionisation ratio* (TPR_{10}^{20}) can be utilised. The TPR_{10}^{20} is defined as the ratio of dose measured at 20 cm depth to that measured at 10 cm depth for a constant distance between source and detector and a 10×10 cm^2 field [21]:

$$TPR_{10}^{20} = \frac{D_{20}}{D_{10}}$$

2.2 Developments

In conventional radiotherapy, or *3D conformal radiotherapy* (3D-CRT), treatment machines are designed to deliver static fields of uniform and wedged beams, where a small number of fields are combined to obtain the desired dose distribution. Even though these beams can be collimated to the projection of the target, only convex high-dose volumes can be created.

2.2.1 IMRT and VMAT

A solution to the convexity problem was the introduction of the *intensity modulated radiotherapy* (IMRT). This treatment is performed with several intensity modulated beams delivering a non-uniform dose to the target. However, when the beams are incident from different directions and superimposed, the desired homogeneous dose distribution in the target can be achieved [8]. A further development of the IMRT is the rotational IMRT, or *volumetric modulated arc therapy* (VMAT). By continuously moving the gantry one or more arcs around the patient, the technique offers a possibility of an efficiency improvement and increased dose conformity compared with the discrete number of fixed beam directions [33].

The IMRT and VMAT techniques both differ from the conventional technique in the way the treatments are planned. In the latter case *forward planning* is utilised, that is, the field is adjusted by an expert until the best achievable dose distribution is obtained. The treatment planning when using IMRT or VMAT is, on the other hand, performed by *inverse planning*. In that case, computer algorithms are given a list of criteria by the planner, which they try to fulfil by optimising beam intensity and field formation. The resulting dose distribution is then the one that minimise the difference between the criteria and the obtained distribution [8].

The "Tongue and Groove" Effect

The dynamic dose delivery by the VMAT technique is obtained through a number of static beams, where the instantaneous MLC configuration is defined at each position. To minimise the leakage between adjacent leaves, the MLC leaves are designed so that their sides partially overlap. However, underdosage in overlapping areas can occur, called the "tongue and groove" effect [12], illustrated in figure 2.8. Conventionally, this effect has been reduced by rotating the collimator during treatment. Regarding the many fields and MLC configurations the effect is expected to be clinically insignificant for VMAT treatments due to the smearing of individual fields[12].

2.2.2 Stereotactic Body Radiotherapy

Due to the different characteristics of the tumour and the healthy tissue, the radiation dose is normally delivered in fractions of about 2 Gy once a day per weekday until the desired dose level is reached. However, conforming the dose tightly around the tumour, increasing the dose per fraction may improve tumour control without increasing normal tissue toxicity. A technique based on this principle is *stereotactic body radiotherapy* (SBRT), also known as stereotactic ablative radiotherapy (SABR), and was first introduced in the mid-1990s. Generally, the radiation per fraction using this technique is in the range of 8-20 Gy and is normally delivered in 1-5 fractions, although up to 10 fractions may be used. With SBRT a highly conform isodose distribution with a very rapid dose fall-off can be obtained, thus rendering it possible to deliver a proper dose to the tumour while sparing the adjacent healthy tissue as much as possible [23]. An example of the potential in
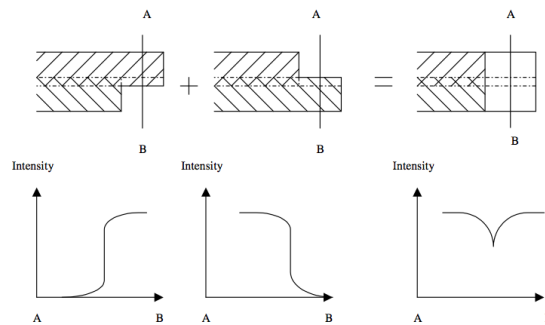
Figure 2.8: Illustration of the "tongue and groove" effect. The MLC leaves are seen from the beam's eye view with the respective intensity curve below. In case of large differences in MLC position, this effect can lead to an underdosage of the target area, as the overlappig area will always be shielded [12].

this technique was shown in 2010, when Timmerman et al. reported a survival rate of 55.8% at 3 years in the case of inoperable early stage NSCLCs using SBRT, in comparison with the 3-year survival of 20-35% with the standard treatment [49].

2.3 Radiobiology

Normal tissue can be described as a composition of small individual functional subunits (FSUs), where there are a large population of well-differentiated functional cells and a much smaller population of clonogenic cells [55]. When cells die off, these clonogenic cells can produce new cells to replace the former. In relation to radiotherapy this mechanism is advantageous, as e.g. radiation damaged areas in a lung may be repaired by the migration of the clonogenic cells within each FSU. However, if the lung receives a dose above the organ's critical threshold all the clonogenic cells within each FSU in the irradiated region might be killed, and the whole region will lose its function. As some FSUs, such as the ones in the lungs, are structurally defined, the clonogenic cells in FSUs outside the region cannot migrate to the lungs and rescue its function when it is overexposed to radiation [23].

2.4 Treatment Planning

A *treatment planning system* (TPS) is utilised to plan the radiotherapy treatment courses. The system requires accurate information about the volume to be irradiated, concerning both anatomical structures and density values delivered by the medical images. Based on the input and user defined criteria, dose calculation and optimisation algorithms calculates the optimal dose distribution to be delivered, which then is verified by a phantom measurement or independent dose calculation algorithms.

2.4.1 Volume Definitions

The International Commission on Radiation Units and Measurements (ICRU) [27] has defined volumes related to the treatment planning to make it possible to prescribe, record, and report the absorbed dose across different institutions. In table 2.1 a list of the central definitions is given,

whose illustration is shown in figure 2.9.

Table 2.1: Definition of volumes in treatment plannng [27].

Volume	Abbrevation	Description
Gross tumour volume	GTV	Volume of demonstrable tumour extent.
Clinical target volume	CTV	Volume of known and/or suspected tumour infiltration.
Internal target volume	ITV	Geometric volume taking into account the internal uncertainties.
Planning target volume	PTV	Geometric volume taking into account the internal and setup uncertainties.
Organ at risk	OAR	Volume of normal tissue that if irradiated could suffer significant morbidity and thus might influence the treatment planning.
Planning OAR volume	PRV	Total margin added to the OAR to compensate for uncertainties in internal movement and setup deviations.

The dose conformity in radiotherapy is restricted by uncertainties in treatment delivery. The most important interfractional geometric uncertainties when treating the thorax are tumour shrinkage or growth, patient setup errors, and shifts in respiration levels, while the intrafractional geometric uncertainties are due to respiratory and cardiac motion [56]. Eliminating or decreasing the geometric uncertainties, enables the use of smaller margins to the planning volumes and thereby increases the sparing of normal tissue. However, during conventional fractionated lung cancer treatment, pleural effusion and atelectasis (i.e. failure of part of the lung to expand) can cause considerable anatomical changes[40]. This can cause an error so large that it cannot be handled by margins, but needs to be accounted for by *adaptive radiotherapy*, i.e. renewal of treatment plan during the treatment course [28].

Dose-Volume Histogram

The dose distribution can be evaluated by the use of dose-volum histograms (DVHs), which is a cumulative histogram of the relative volume of a specific structure receiving a dose equal to or above a given dose *d*. DVHs are often utilised to investigate the homogeneity of the dose distribution, however, they do not give any information about where the possible underdosage or overdosage occur [22]. The spatial dose distribution inside a given structure is therefore often evaluated by also inspecting the CT images including the dose simulation.

Conformity index

How well the volume of a radiosurgical dose distribution conforms to the size and shape of a target volume can be measured by a *conformity index*. By convention, the perfect conformity score is
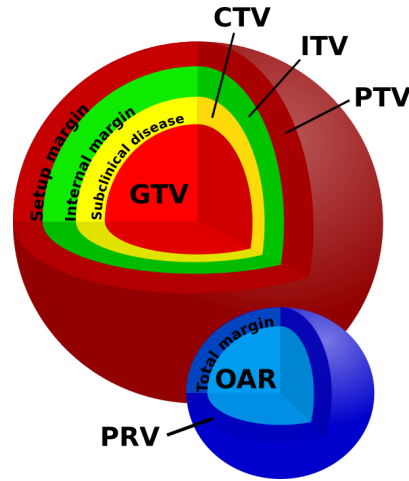
Figure 2.9: Schematic illustration of the volume definitions given in table 2.1 [3].

unity, although there are several different ways of defining the index. A conformity index proposed by Paddick [35] is defined as follows:

$$\text{conformity index} = \frac{TV_{PIV}}{TV} \times \frac{TV_{PIV}}{PIV} = \frac{TV_{PIV}{}^2}{TV \times PIV},$$

where TV is the target volume, PIV is the prescription isodose volume, and TV_{PIV} is the volume of the target covered by the prescription isodose. Hence, the first term represents the under-treatment ratio, while the second term represents the overtreatment radtio. An illustration of the different ratios are given in figure 2.10.

Figure 2.10: Illustration of different ways of defining the conformity index[35]

2.4.2   Patient Immobilisation

There are several different designs of immobilisation devices such as fixation masks and frames, which can be applied depending on the treatment device used and the body site treated. The positioning system should be comfortable throughout the longer treatment sessions, to lower the risk of patient movement during treatment, and also promote a highly reproducible position. In lung SBRT, the different motion control devices can be defined in three general categories: dampening, gating, and chasing. The dampening category includes among other things the systems of abdominal compression to reduce motion related to the diaphragm, and breath-hold manoeuvres to freeze the tumour in a reproducible stage of the respiratory cycle. The gating systems use a surrogate to follow the respiratory cycle and then trigger the beam to deliver radiation only during a specific segment. When using a tracking system, the radiation beam is designed to follow the moving target [50].

The Interplay Effect

With improved conformity of the IMRT and VMAT techniques, the greater need of tumour position accuracy follows. An *interplay effect* can occur if there is a correlation between the breathing motion and MLC leaf motion, which might lead to underdosage of the tumour. Intra-fraction target motion due to the patient's breathing is considered a random error, and would normally lead to a "blurring" of dose using the conventional treatment with many fractions. Using FFF SBRT the number of fractions and delivery time is significantly reduced, making the error more prominent [7]. However, results obtained by Ong et. al. [30] by phantom measurements indicate that the use of more than two fractions and more than one arc makes the interplay effect unlikely to be clinically significant.

2.4.3   Imaging

Tumours and organs at risk are localised with 3D imaging techniques. Computed tomography (CT) is a common tool, as it has the beneficial potential to quantitatively characterise the physical properties of heterogeneous tissue in terms of electron densities which is essential for dose calculation [39]. When imaging the lungs, normal breathing can cause severe motion artifacts. For diagnostic scans, the scanning can be performed during breath hold to minimise internal motion. However, in radiotherapy, the time span of each treatment can be too long for a patient to maintain a stable breath hold throughout the treatment session. Therefore, the CT images used for planning need to be generated for the entire respiratory cycle. A common method is to perform a very slow acquisition process that is correlated to the respiratory signal through an external surrogate, such as a pressure measuring belt or a laser devise for optical monitoring of the abdominal motion. Retrospectively, the respiratory cycle can be presented by binning the acquired data into the respective phases. This procedure is referred to as *four-dimensional computed tomography*, or *4D-CT* [18].

An efficient acquisition mode is the *low pitch helical scan*, where each slice of the desired volume remains illuminated for at least the duration of one respiratory cycle, due to an ultra low couch speed or very low pitch factor. Then, during the binning process, the different slices from the CT scan are binned together with other slices that were acquired at the same phase of the respiratory cycle, illustrated in figure 2.11 [18].
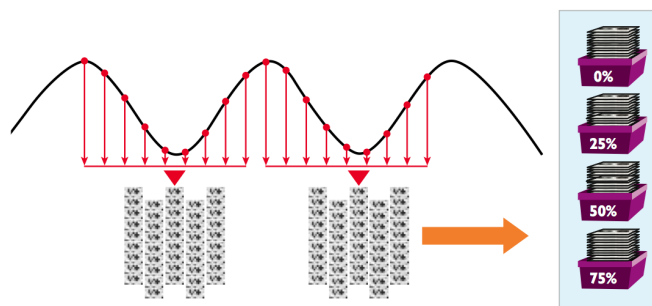
Figure 2.11: Illustration of multi-phase acquisition on a multi-slice scanner. The 0% phase is the local maximum and represents the maximum inhale CT, while the 50% phase is the local minimum and represents the maximum exhale CT [18].

There are several methods of combining the information from each breathing phase, which leads to different approaches to obtain a realistic static image of the tumour localisation and the extent of ITV. The routine clinical use of 4D CT scans requires that the GTV is contoured in up to 10 phases of respiration [9]. The resulting workload is a major drawback, thus post-processing tools such as maximum intensity projection (MIP), averaged intensity (AI) 4D CT images, and density override (DO) techniques are commonly used instead.

A maximum intensity projection (MIP) is used in combination with a CT image taken when the patient is keeping his or hers breath after exhalation, as the patient's breathing most probably stays the longest in this phase. The MIP image reflects the highest data value encountered along the viewing ray for each pixel of volumetric data during the breathing cycle [51], as illustrated in figure 2.12b. Matching the MIP image to the static breath-hold image, the ITV can be delineated during the planning process. Then, when simulating the dose distribution, only the static image is utilised, but with an ITV given by the MIP.

The average intensity (AI) image is a superposition of all the images in the 4D CT scan, where each voxel has a density equal to the weighted average of the Hounsfield values from all breathing phases [43]. The resulting image is used both during delineation and dose distribution planning, thus no static breath-hold CT image is required. Following instructions on how to breath can be challenging for a patient, and hence lead to unnatural breathing cycles that are difficult to reproduce. The fact that AI imaging can be performed during free breathing is therefore a great advantage. In figure 2.12c the production of an AI image is illustrated.

In addition to the MIP and AI techniques there are different *density override* (DO) models. To mimic the effective density during free breathing irradiation, the densities of specific structures in the static CT image are adjusted. This can be performed by e.g. overriding densities in the PTV volume lower than a certain threshold value or smoothing the density within selected volumes [43] [54]. The edited image is used for both delineation and dose distribution planning.

It is also common practice to take a cone beam CT scan just before the treatment starts. This is to verify that the position of both the tumour and surrounding tissue are in accordance with the treatment to be delivered.
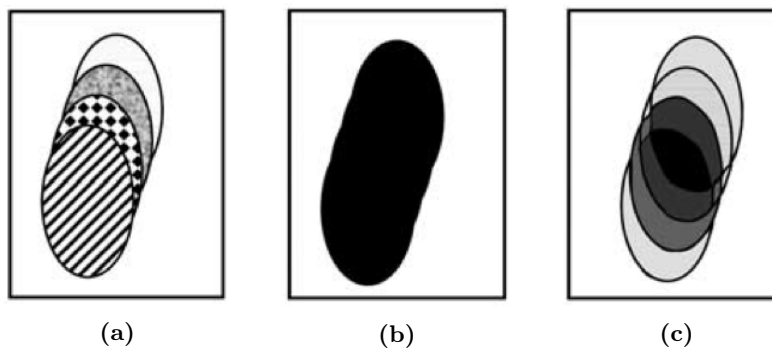
Figure 2.12: Illustration of the pixel-based intensity projection protocols from 4D CT data sets of a tumor in motion. The separate phases are illustrated in (a), whereas the MIP and AI images are shown in (b) and (c), respectively [51].

2.4.4 Dose Calculation

Of central importance to radiotherapy is the accurate calculation of a 3D dose distribution within the patient, as dose-effect relations can map dose to outcome of treatment. Three main categories of dose calculations are *correction based methods*, *model-based algorithms* and *Monte Carlo simulations*. The calculation models have two main tasks, which is to model the properties of the particles emerging from the treatment head, and to calculate the energy transport through the patient. Even though the modern treatment techniques are posing increasing demands on the accuracy of the dose algorithms, clinical use involve that this cannot be achieved at the expense of lengthy computation times. The Monte Carlo simulations are very accurate, but thereby also very time consuming. Correction-based methods, on the other hand, are very fast, but too inaccurate for many purposes. Therefore, the time-accuracy compromise underlying the model-based algorithms makes them a common tool in the clinic today [39].

The Analytical Anisotropic Algorithm (AAA)

Model-based algorithms consider the primary photon fluence (i.e. the fluence of photons emerging from the linear accelerator) as an input for the subsequent calculation of the energy absorption and transport within the patient. First, the absorption, expressed by the "total energy released per mass" (TERMA), is calculated. Then, the introduction of "dose kernels" accounts for the transportation of this energy via secondary electrons and photons. These kernels describe the energy transport and deposition in water caused by a defined set of primary tissue interactions. When producing CT images, the anatomy of the patient is represented by the Hounsfield numbers. Thus, by scaling by density, the inhomogeneities can be taken into account, as illustrated in figure 2.13. This provides a realistic description of the dose distribution in both homogeneous and heterogeneous media [39].

The *Analytical Anisotropic Algorithm* (AAA), which is a 3D pencil beam convolution superposition algorithm based on Monte-Carlo-determined basic physical parameters, compromises accuracy and efficiency. It allows analytical convolution, which suppresses the computation time significantly. After separate modelling of primary photons, scattered extra-focal photons, and electrons scattered from the beam limiting devices, the total dose distribution is obtained by superposition of the doses from the photon and electron convolutions [42].

The TPS *Eclipse*^{TM} has the opportunity of using the AAA algorithm. Regarding the support
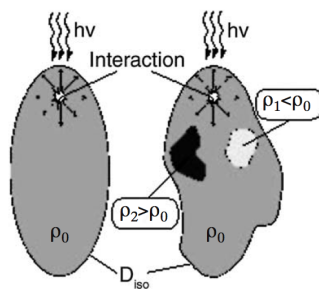
Figure 2.13: Density scaling in homogeneous and heterogeneous media [39].

structures, the couch structure is accounted for in the AAA calculation by an attenuation factor.

Monte Carlo Simulations

The Monte Carlo (MC) simulation is considered as the most powerful tool when modelling and analysing radiation transport for radiotherapy applications due to its advantageous handling of multiple dimensions [41], and can provide a dose calculation accuracy of 2%-3%[44] [37]. By tracing millions of photons and secondary particles, the dose deposition is calculated based on the physics of their interaction with matter. The MC technique can in general be defined as follows:

> *Monte Carlo is a numerical method to solve equations or*
> *to calculate integrals based on random number sampling.*

The MC numerical integration is applied when it is impossible to integrate an equation analytically. It is based on a sequence of uniformly distributed random numbers in the given interval or volume, and, due to its long convergence time, is best suited for problems with many dimensions.

For dose calculation, multidimensional numerical integration is necessary to solve the problem of coupled transport equations. In theory, the problem has an infinite number of dimensions because the number of secondary photons and electrons is physically unlimited when it starts with a primary particle of definite energy. Practically, due to the limited region of interest and the fact that the simulation is set to stop if the particle energy falls below a minimum value, the dimensionality is limited.

A schematic illustration of an MC radiation transport simulation is given in figure 2.14. It shows an example of a *particle history*, which is a shower of secondary particles generated by a primary particle including all daughter particles. The simulation starts with a primary particle emitted from a particle source. The geometry of the problem, e.g. the geometry of the linac head and patient anatomy given by technical specifications and the CT images, and the material transport properties, given by cross section data, are both taken into account during the simulation. Distance to interaction, type of interaction, and the angles and energies of the secondary particles are determined based on cross sections of the medium and probability distributions. Then, this is repeated until the primary and secondary particles have left the simulation geometry or the particle energy is lower than the given cut off value. When these steps are performed for a sufficient number of particle histories, the dose is calculated by accumulating the absorbed energy per region.
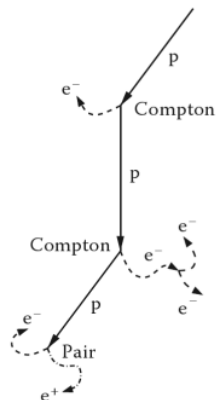
Figure 2.14: Example of a particle history. The starting particle is a primary photon p that, via Compton interactions and pair production events, leads to secondary photons p and secondary electrons e^- and positrons e^+. In the energy range of radiotherapy, the four most common type of interactions are *photoelectric absorption*, *Raleigh scatter*, *Compton scatter*, and *pair production* [41].

To reduce noise, a huge number of particle histories has to be simulated, which results in very long computation times. However, the time is often reduced by the *condensed history technique* in the case of charged particles, where the collisions are divided, based on their kinetic energy (E_c) transfer, into soft (low E_c) and hard (high E_c) collisions. The soft collisions are calculated implicitly by continuous energy transfer onto the matter surrounding the particle track and a direction change determined by one large multiple scatter angle, instead of many small angles. The hard collisions are simulated explicitly, as described by figure 2.14.

Electronic Equilibrium

If a charged particle of a given type and energy leaving an irradiated volume V is replaced by an identical particle of the same energy entering volume V, *Charged Particle Equilibrium* (CPE) is obtained [26]. In radiotherapy with photon beams, the role of the secondary electrons predominates the other charged particles involved. Hence, CPE is often referred to as only *electronic equilibrium*. The basic concept of CPE is illustrated in figure 2.15. KERMA (*Kinetic Energy Released per unit Mass*) is defined as the sum of the initial kinetic energy of all the charged particles released by uncharged ionizing radiation. Assuming negligible photon attenuation (implying constant KERMA) and only considering one electron generated per volume, moving in the direction of the photon beam, the electron tracks can be drawn. As seen in the left part of figure 2.15, only a fraction of the electron tracks deposits energy in the first voxels, resulting in a *bulid-up region* or *electronic disequilibrium*.

The electronic disequilibrium can also occur perpendicular to the beam direction, a phenomenon called *lateral electronic disequilibrium* (LED). When the lateral range of the electrons becomes equal or greater than the radius of the field, the electrons liberated from the beam's central-axis will scatter beyond the field edge. As they are not replaced, this leads to a reduced dose along the beam's central-axis. Due to the long electron range, the effect is most prominent in low-density medium [13].
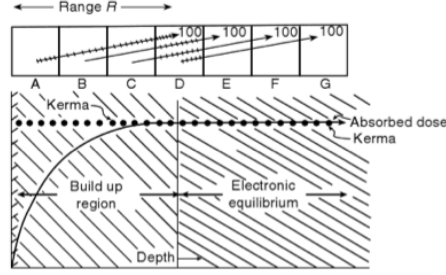
Figure 2.15: Schematic illustration of a electronic equilibrium[26].

2.4.5   Verification

For verification purposes, phantom measurements or a high-precision simulation algorithms can be utilised. Examples of such algorithms are ETRAN, EGSnrc and MCNP. Due to their precision, they are common tools for verification of different approximations and performance of pencil-beams algorithms [6].

Useful parameters to evaluate the dose is *dose deviation* and *distance to agreement* (DTA) . The DTA is defined as the minimum distance between a verification point and a point from the treatment plan that has a dose deviation of zero:

$$d(\mathbf{r}_v) = \min\{r(\mathbf{r}_v, \mathbf{r}_p)\} = \min\{|\mathbf{r}_p - \mathbf{r}_v|\},$$

where

$$\delta(\mathbf{r}_v, \mathbf{r}_p) = D_p(\mathbf{r}_p) - D_v(\mathbf{r}_v) = 0.$$

The p and v denotes *planned* and *verification*, respectively, and $D(\mathbf{r}_x)$ is the received dose in the given position. The *gamma index* [24] is a quality index taking into account both these parameters, as follows:

$$\gamma(\mathbf{r}_v) = \min\{\Gamma(\mathbf{r}_v, \mathbf{r}_p)\}\forall\{\mathbf{r}_p\},$$

where

$$\Gamma(\mathbf{r}_v, \mathbf{r}_p) = \sqrt{\frac{r^2(\mathbf{r}_v, \mathbf{r}_p)}{\Delta d_V^2} + \frac{\delta^2(\mathbf{r}_v, \mathbf{r}_p)}{\Delta D_V^2}}.$$

The Δd_V^2 and ΔD_V^2 are the passing criteria for DTA and dose deviation, respectively. The calculation passes if $\gamma(\mathbf{r}_v) \leq 1$ [24].

2.4.6   Deformable Registration and Dose Accumulation

Even in the case of a moving target, e.g. treatment of lung cancer, the treatment planning is performed on a static image (recall subsection 2.4.3). Hence, the image used for planning is only an approximation of the real situation.

One way to simulate the real dose distribution is to accumulate the dose with respect to all the phases of the 4D CT scan. That is, for each phase of the irradiated tissue's motion, the dose is

deformed to a mutual registration reference to be accumulated. Several different approaches have been proposed for this purpose [57] [46] [17].

The process of image registration involve the identification of corresponding elements from two different images and the determination of a transformation field to match these elements. The determination of the corresponding elements can be based on different criteria such as voxel intensity, pattern similarity or features like implanted markers. Figure 2.16 illustrates the two types of registration; *rigid* and *non-rigid*. In the case of a deformed shape of the subject, rigid registration is not sufficient, as it only has the opportunity of rotational and translational alignment of the images. The non-rigid registration type adjusts to the subject, enabling a mapping the local details ([53] and references therein).

(a) Input shapes

(b) Rigid T   (c) Non-rigid T
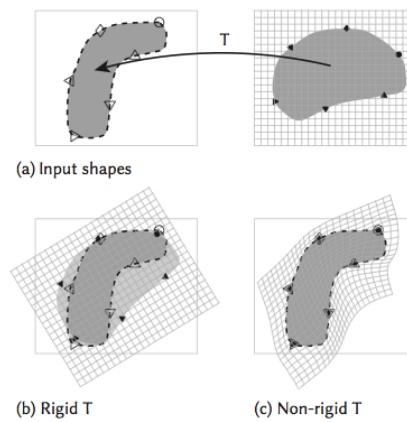
Figure 2.16: Registation types. The identification of corresponding elements (circles, triangles, etc.) and the transformation T to align the images. (a) Images to be aligned by either (b) rigid or (c) no rigid registration[53].

By deforming the dose distributions of each the motion phases to a reference image, accumulated dose can be calculated. However, in the case of lung cancer, the breathing pattern can be quite irregular and a weighting factor should be assigned each image according to the time fraction spent in that phase. An illustration of the procedure is given in figure 2.17.
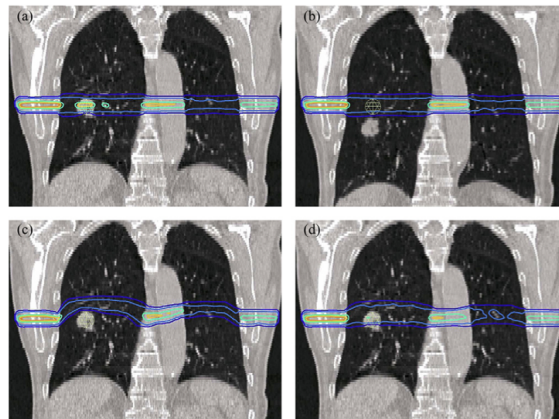
Figure 2.17: An example of 4D dose accumulation. Beamlet doses are calculated in eight phases, where the exhale and inhale CT dose distributions are shown in figure *a* and *b*, respectively. Figure *c* illustrates the warping of the dose of the inhale CT to the exhale reference geometry. Adding the reference images of all phases together results in the accumulated dose distribution in figure *d* [47].

3   Materials and Methods

3.1   Patient and Phantom Material

Five patients with non-small-cell primary lung cancer treated with SBRT at Haukeland University Hospital during 2014 were retrospectively chosen for this study. The patients were selected based on tumour motion larger than 5 mm, as seen on 4D CTs. Sex and specific age (all were adults) were not regarded as necessary information related to this project. Tumour motion and tumour characteristics are listed in table 3.1.

Table 3.1: Tumour motion and characteristics: The maximum tumour amplitude was in the craniocaudal plane, denoted by the *Motion* column.

Case	Tumour location	Amplitude [cm]	ITV [cm^3]	PTV [cm^3]	Vol. ratio (ITV/PTV)
sbrt01	Right lung, inferior posterior part. Close to thorax and diaphragm.	1.3	33.6	73.0	0.46
sbrt05	Right lung, centred in all directions.	0.7	10.0	28.5	0.35
sbrt12	Right lung, centre posterior part.	0.5	6.7	23.9	0.28
sbrt13	Left lung, centred in all directions.	1.4	58.6	117.9	0.50
sbrt14	Right lung, lateral central part.	0.5	1.7	9.8	0.17

For the phantom study, a virtual water phantom and the homogeneous, cylindrical *Delta4* phantom (ScandiDos AB, Uppsala, Sweden) was used. In *Eclipse^{TM}* the density of *Delta4* was set to 1.1433 g/cm^3 (202 HU). The treatment couch utilised in all investigation is the Exact IGRT treatment couch(Varian Medical Systems, Palo Alto, CA)

3.2   CT post-processing and delineation

Each of the patients had a 4D CT scan (obtained through *low pitch helical scan*) and a static exhalation (*breath hold*) CT scan (*Phillips Brilliance CT Big Bore*, Cleveland, OH, USA). In each case, the couch speed was adjusted individually to the patient regarding the patient's breathing pattern, monitored by the pressure measuring belt (*Phillips Pulmonary Toolkit*, Cleveland, OH, USA). The slice thickness was set to 3 mm and the plane size to 512×512 pixels. The scanner sorted the images into eight phases by amplitude binning, where the maximum inhale (0%) and maximum exhale (50%) phases were the average maximum and minimum amplitudes of the respiratory curve, respectively. The remaining breathing phases were equally distributed in-between these references (Chap. 2.4.3).

Three different post-processing techniques were examined in the present study; the maximum intensity projection (MIP), the average intensity (AI), and a version of the density overwrite (DO) techniques (Chap. 2.4.3). These techniques will be referred to as *St*, *Avg* and *DO*, respectively (figure 3.1).

Contouring of both target volumes (TVs) an organs at risk (OARs) was performed by the responsible oncologist on the *St* images (Chap. 2.4.1). The dose given the OARs and the dose close to OARs were carefully minimised. For the purpose of this study, the patient outline (BODY), skin, costa and lung structures were specially recontoured on the *Avg* images, while copy/paste was used for the remaining structures. The 4D CT scans were performed differently from the 3D CT scans taken during breath hold, causing a small difference in resolution that resulted in a small difference in volumes. Still, this was considered as a negligible deviation (Appendix 8.2 table 8.1).

(a)   **(b)**   **(c)**
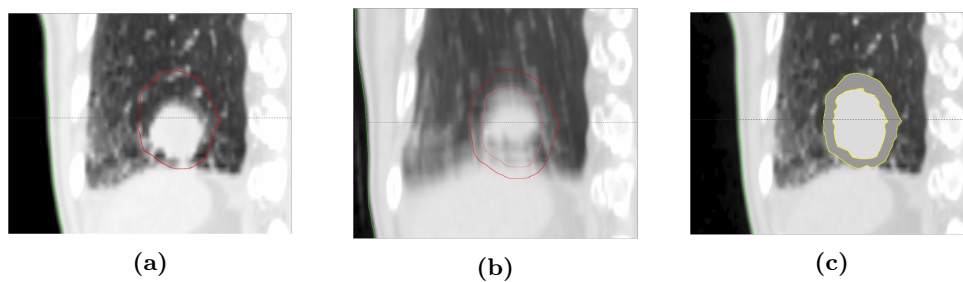
Figure 3.1: Overview of the investigated CT bases; (a) St, (b) Avg, and (c) DO.

3.3   Treatment Planning and Simulation

Treatment planning and simulations were performed in a commercial treatment planning system ($Eclipse^{TM}$, Varian Medical systems, Palo Alto, USA). Following the clinical protocol at HUH, the patients were planned to receive 55 Gy in 5 fractions (2 patients) or 54 Gy in 3 fractions (3 patients). All treatment plans were planned with the Volumetric Modulated Arc Therapy (VMAT) technique and flattening filter free (FFF) beams (Chap. 2.2.1 and 2.1.2) for the *TrueBeam* linac (Varian Medical systems, Palo Alto, USA). For all five patients, one treatment plan utilising 10 MV and one treatment plan utilising 6 MV beams were created for each of the CT bases (*St*, *Avg* and *DO*), comprising 30 new treatment plans in total (5×2×3). These were used in comparison with the original (clinical) plans, which were planned with the 3D-CRT technique on the *St* CTs using a beam quality of 6 MV. An overview of the treatments is given in table 3.2.

Table 3.2: Treatment characterisation overview.[a]

	CT basis			Energy		Fields	Planning		Techn.	
	St	Avg	DO	6 MV	10 MV		Forward	Inverse	FF	FFF
Original plan	×			×		9-15	×		×	
VMAT	×	×	×	×	×	Partial or full arcs		×		×

[a]St=Maximum Intensity Projection, Avg=Average Intensity, DO=Density Overwrite, FF=Flattening Filter, FFF=Flattening Filter Free.

Partly arcs were used for patients with laterally situated tumours (patient 13 and 14) to avoid

collision. All other treatments were performed with full arcs with the isocentres in $x = 0$, using an avoidance sector when passing the contra lateral lung. The static fields and arc trajectories are illustrated in figure 3.2. More details of the plans are given in table 3.3.
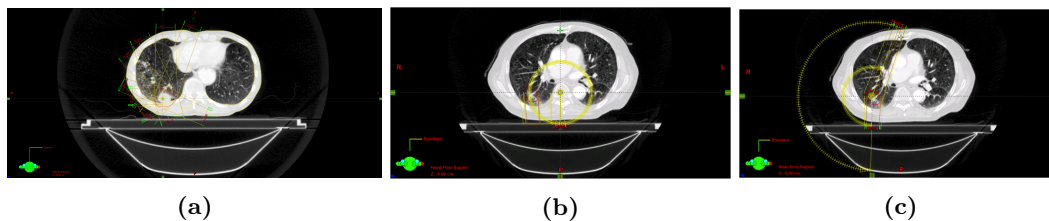

| (a) | (b) | (c) |

Figure 3.2: Treatement of lung cancer using (a) static fields, (b) full arcs and (c) partly arcs.

Table 3.3: Details of the treatment setup.

Case	Frac.	Original plan	VMAT
sbrt01	5×11Gy	Fields: 7×6MV, 3×15MV	Arc: Full
			Avoidance sector: 21°-114°
sbrt05	3×18Gy	Fields: 11×6MV	Arc: Full
			Avoidance sector: 27°-133°
sbrt12	3×18Gy	Fields: 11×6MV	Arc: Full
			Avoidance sector: 23°-122°
sbrt13	5×11Gy	Fields: 10×6MV	Arc: Partly, iso. x: 9 cm
			Arc span: 340°-179°
sbrt14	3×18Gy	Fields: 9×6MV	Arc: Partly, iso. x: -10 cm
			Arc span: 181°-20°

In all VMAT cases, the collimator was rotated 20° and 340° for the first and second arc, respectively, to increase the degrees of freedom when optimising the MLC configurations. The MLC of the Varian linac device had 5 mm width of leaves in the inner 20 cm of the field, and leaves with a width of 10 mm on each side, spanning 20 cm. The configuration had 120 MLC leaves (60 pairs).

The same guidelines as for the original plan were used as initial basis for VMAT optimisation (Appendix 8.3). Individual adjustments were made by changing the priority of objectives when possible to improve sparing of healthy tissue without compromising target coverage. All plans were approved by a responsible oncologist.

The optimisation algorithm was the Progressive Resolution Optimiser (PRO) including multi-resolution dose calculation (MRDC), whereas the intermediate and finalising algorithm that calculated the dose was the Anisotropic Analytic Algorithm (AAA) (Chap. 2.4.4). The calculation grid was set to 2.5 mm.

Jaw tracking and standard settings of the auxiliary function "Normal tissue objective" were utilised for all VMAT plans to reduce dose to healthy tissue. The VMAT plan normalisation was set to

95%, i.e. 100% of the prescribed dose covered 95% of the volume.

3.4 Monte Carlo System

For Monte Carlo simulations a Monte Carlo Treatment Planning System, Hyperion [14], was utilised (Chap. 2.4.4). Hyperion allows inverse Monte Carlo treatment optimisation and provides a separate plan verification tool, *MCverify*. *MCverify* uses a treatment plan in the form of the DICOM RTPlan and the density grid in the *Pinnacle* format (Phillips Healthcare, Cleveland, OH, USA)) created based on the 3D CT image.

Hyperion uses an MC dose calculation system optimised for use in radiotherapy, which is comprised of three main components:

1. A particle generator - a virtual source model (VSM) of therapeutic photon beams.

2. A transmission filter - an analytical model of the beam modified as described in reference [43].

3. A Monte Carlo dose engine, XVMC, which is an efficient and accurate MC dose calculation algorithm [15].

A crucial part of this system is the beam model, as it provides the input Phase Space data for MC dose calculation and hence cause wrong dose calculation if incorrectly implemented. The beam models used in this project was commissioned for the purpose of this study by Marcin P. Sikora, but is not yet validated for clinical use. This process, referred as commissioning of the system, still requires extensive validation of simulation results with measurements.

The beam models used in this project were commissioned by measurements in water earlier performed at HUH for 3×3 cm^2 to 40×40 cm^2 at a source-surface-distance (SSD) of 100 cm. The normalisation point is the reference calibration of each linac at HUH, which is at $SSD = 90$ cm for 130 MU, with fields of 10×10 cm^2 and a depth of 10 cm in water.

3.5 Data Processing

In order to decrease calculation time, a higher statistical variance was permitted for the VMAT plans. This was a reasonable simplification, considering that the total plan statistical uncertainties are dependent on the number of simulated histories in the volume of interest, not the variance per segment (Chap. ??). For water phantom measurements, the variance criterion was set even lower for precision, with MU values of 130 and prescribed dose of 1 Gy (only one fraction). The MC variation criteria and simulation geometry settings are listed in table 3.4, where the choice of density in the treatment couch is based on the work of Teke et. al [48].

3.5.1 Verification

The *Delta4* phantom (ScandiDos AB, Uppsala, Sweden) with its respective software was used for verification of the treatment delivery (Chap. 3.1). The phantom consists of two crossing detector-arrays that detect the three dimensional dose, illustrated in figure 3.3. In these measurements the

Table 3.4: MC variation and simulation geometry settings added to patient specific data.

Dose grid size	
All plans	$2.5 \times 2.5 \times 2.5$ mm^3
Mass density couch surface	
AAA	0.7109 g/cm^3
MC	0.4000 g/cm^3
Mass density couch interior	
AAA	0.0174 g/cm^3
MC	0.0520 g/cm^3
MCvariance	
Delta4 vertical fields	0.005
3D-CRT	0.01
VMAT	0.05

detectors in the dose range 20 % to 500 % were included. For Patient Quality Assurance (QA) with *Delta4* at HUH, the DTA criterion is set to $\pm$ 3.0 mm and the dose deviation limit to $\pm 3\%$ (relative to global maximum) (Chap. 2.4.5). The treatment passes if at least 95 % fulfil the $\gamma \geq 1$ criterion.

| (a) | (b) |
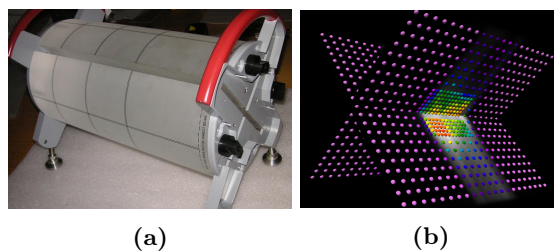
Figure 3.3: The (a) *Delta4* phantom uses (b) crossing planes of detectors to measure the three dimensional dose distribution (images from respective software).

In addition, the Electron Gamma Shower (EGSnrc)[19] Monte Carlo algorithm was used for verification of dose distribution in a water phantom (Chap. 2.4.5). The Phase Space data was simulated using fields of jaws only (i.e. no MLCs) with a BEAMnrc MC system using the Phase Space data above the beam modulators (jaws) provided in the MC package offered by Varian (Varian Medical Systems, Palo Alto, CA). A new Phase Space data were stored at $SSD = 100$ for further dose calculation by a *dosexyznrc* [20] program with settings listed in table 8.3, Appenix 8.4.

3.6   4D Dose Calculation

3.6.1   Deformable registration

To be able to accumulate the dose in the dynamic patient model, correspondence between anatomical points from one CT phase to another had to be established, requiring deformable registration (Sec. 2.4.6). In this study a non-rigid intensity-based method developed specifically for lung registrations provided by developer M. Söhn (*Matcher 3D*)[46] was use for this purpose.
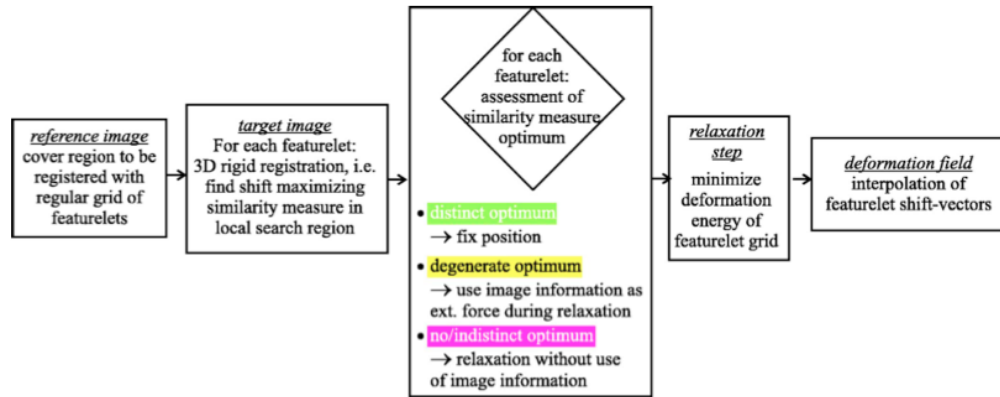
Figure 3.4: Flow chart representing the work flow of the *Matcher 3D* program, which is a featurelet based image registration algorithm. The resulting deformation field was used to adjust the geometry of a phase image into the reference geometry [46].

The workflow of the *Matcher 3D* program is presented in figure 3.4. The model divided the irradiated volume into regularly distributed small subvolumes ("featurelets"). Then, each featurelet of the chosen phase image was assigned to the optimal featurelet of the reference image based on the anatomical image information and iterative minimisation of the local deformation energy, as illustrated in figure 3.5. Selecting phase 0% (CT0) as reference image, the deformation fields between each phase and the reference image were calculated. As a result, a global displacement field was calculated from the shifts of the featurelets by interpolation. Due to the lack of fixed reference points, there was no quantitative accuracy measure. Visualisation of dose deformation was used to assure the quality of the dose positioning.
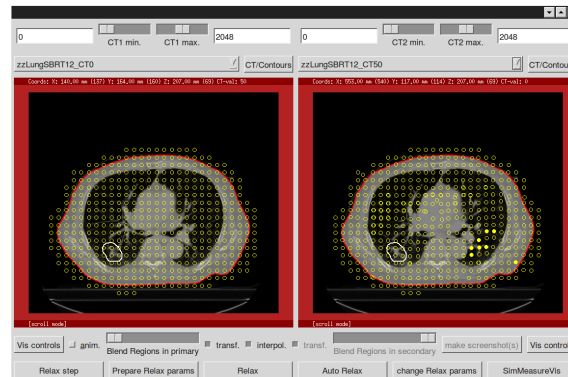
Figure 3.5: *Matcher 3D*: Example of the distribution of subvolumes in an axial plane of the lungs. To the left, the CT0 phase (the maximum inhale CT) is chosen as reference image. The CT50 phase (the maximum exhale CT) image to the right have been assigned subvolumes corresponding to the subvolumes of the reference image. The circles are the centres of the subvolumes, where the filled circles are the ones centred in plane. The white contour depicts the PTV structure.

Contemporary, each of the treatment plans were calculated on each CT phase of the 4D CT scan, i.e. eight MC simulations per treatment plan. When both processes were finished, the MC calculations of each treatment plan were transferred to *Matcher 3D*. For each phase (except the reference phase) the simulated dose was warped by the deformation field, so that the dose given in the spe-

cific phase was displayed on the anatomy of the reference image. The result was eight different dose distributions on the reference image per plan that could simply be added together as a weighted sum. The process is illustrated in figure 3.6.
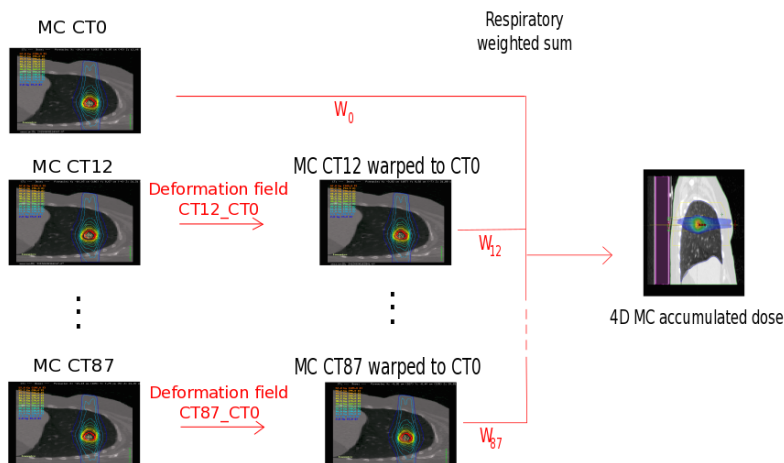
Figure 3.6: Illustration of the accumulation process. The treatment plan is MC simulated on each phase of the 4D CT scan and then warped to the reference CT set (CT0). A weighted sum make up the total 4D MC accumulated dose.

3.6.2   Summation of dose

The weighting of each phase in the summation was dependent on the time the tumour spent in that position. Unfortunately, the breathing patterns were no longer available, as this was a retrospectively study. Therefore, the weighting was based on a generalisation of the respiratory curve; That the inhale-exhale ratio was of 1:2[2]. Approximately, this resulted in expiration phases of double weight (2/12) compared to the inhalation phases (1/12), and maximum inhalation and expiration phase weights of the mean value of these (1.5/12), as illustrated in figure 3.7. It has to be emphasised that this approach is a very generalised approximation. However, as the breathing curve of a patient can by quite varying [34], a more specific approach could be misleading.
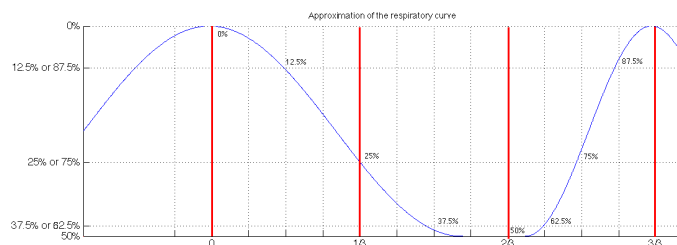
Figure 3.7: An approximation of the respiratory curve created by combining two harmonic curves and dividing into phases based on amplitude [4]. Exhalation happens between phase 0% and 50%, while the inhalation occurs faster between the 50% and 0% phases. The red lines illustrates the inhale-exhale ratio of 1:2 [2].

3.7   Data Handling

The time consuming process of transferring data from $Eclipse^{TM}$ to *MCverify* and *Matcher 3D*, including data type transformations from *DICOM* to *Pinacle* format (Hyperion), and further to *Matcher 3D* compatible format, was performed manually using a combination of graphical interfaces and scripting in Python [1]. Size adjustments and positioning handling were validated visually and processing scripts, mainly based on the *pydicom* and *numpy* packages, were developed on-demand to validate and increase the efficiency of the process.

3.8   Evaluation

The visual evaluation of the results was performed using $Eclipse^{TM}$ TPS, including built-in dose profile funitons. DVHs was exported and used as data basis for the MATLAB calculation and grapical representations [4].

3.9 Experiments

An overview of the present study's experiments is listed in table 3.5, and a work flow is shown in figure 3.8.

Table 3.5: Study outline.

Chapter	Experiment
3.9.1	Phantom study
3.9.2	Static model MC calculation
3.9.3a	Verification: 4D MC dose accumulation
3.9.3b	Verification: Comparison of the planned and MC accumulated dose

3.9.1 Phantom Study

Aim: Benchmark the AAA and MC calculation algorithms.

Calibration investigation. One 3×3 cm^2 and one 10×10 cm^2 static open field were simulated by AAA and MC for all the beam settings (6 MV FF, 15 MV FF, 6 MV FFF and 10 MV FFF) on a water phantom. This investigation was performed for both water density and with the density set to 1.1433 g/cm^3 (density of the *Delta4* phantom). To further verify the simulations, an EGSnrc simulation was performed for both densities on a water phantom (Chap. 3.5.1).

Impact of treatment couch. Calculated with two opposing 3×3 cm^2 vertical fields for the *Delta4* phantom was performed for the same beam settings as in the calibration step(Chap. 3.5.1). This was performed both with and without the treatment couch. A 6 MV 3D-CRT (FF), a 6 MV VMAT (FFF) and a 10 MV VMAT (FFF) verification plan were generated in *Eclispe^{TM}* for the *Delta4* phantom (Chap. 3.5.1). The plans were then copied and added the couch structure in the structure set before AAA recalculation. The field setup for the phantom was the same as for the sbrt05 Original, 6MV St and 10MV St treatments (Chap.3.5). All plans were transferred to *MCverify* for MC recalculation (Chap. 3.4) and then transferred back to *Eclipse^{TM}* for comparison (Chap. 3.8).

Verification of planned treatments. Using the AAA calculated treatments of patient sbrt13 (Chap. 3.3), phantom measurements of the VMAT treatments was performed on the *Delta4* phantom (Chap. 3.5.1). Analysing the results, the MC calculated dose distributions (Chap. 3.4) of sbrt13 were transferred to the *Delta4* software for comparison.

Heterogeneity correction. Two crossing fields were simulated on a patient CT set with angle of incidence based on tissue density variations and recalculated by MC (Chap. 3.4). The beam evaluation was performed in *Eclipse^{TM}*(Chap. 3.8)

The use of sbrt05 and sbrt13 treatments as bases for verification simulations were chosen due to their general representation of the remaining treatments.

3.9.2   Static Patient Model MC Simulation

Aim: Determine calculation accuracy using different CT bases.

For all patients, 6 MV and 10 MV FFF VMAT treatment plans were generated using the *St*, *Avg* and *DO* CT bases (Chap. 3.3). The chosen version of the different DO techniques involved that the ITV was given the density of the GTV, while the margin between the ITV and the PTV was given the average of the GTV and the lung density (Appendix 8.2 table 8.1). The treatment plans were then recalculated with *MCverify* (Chap. 3.4). All MC static patient models were then transferred back to $Eclipse^{TM}$ for comparison with AAA (Chap. 3.8).

3.9.3   Verification

a) 4D MC Dose Accumulation

Aim: Determine a tenable approximation of the "**true dose distribution**".

For each treatment plan, the dose distribution was recalculated by MC on each of the eight phases of the 4D CT scan. The dose distributions were then warped to the reference CT set and accumulated based on respiratory weighting (Sec. 3.6). This process was quite time consuming as it included the processing of 240 MC simulations ($5 \times 2 \times 3 \times 8$).

b) Comparison of the Planned and MC Accumulated Dose

Aim: Evaluate CT bases of treatment planning.

The MC accumulated dose distributions were transferred to $Eclipse^{TM}$ to be compared with the planned AAA dose distribution (Sec. 3.8).
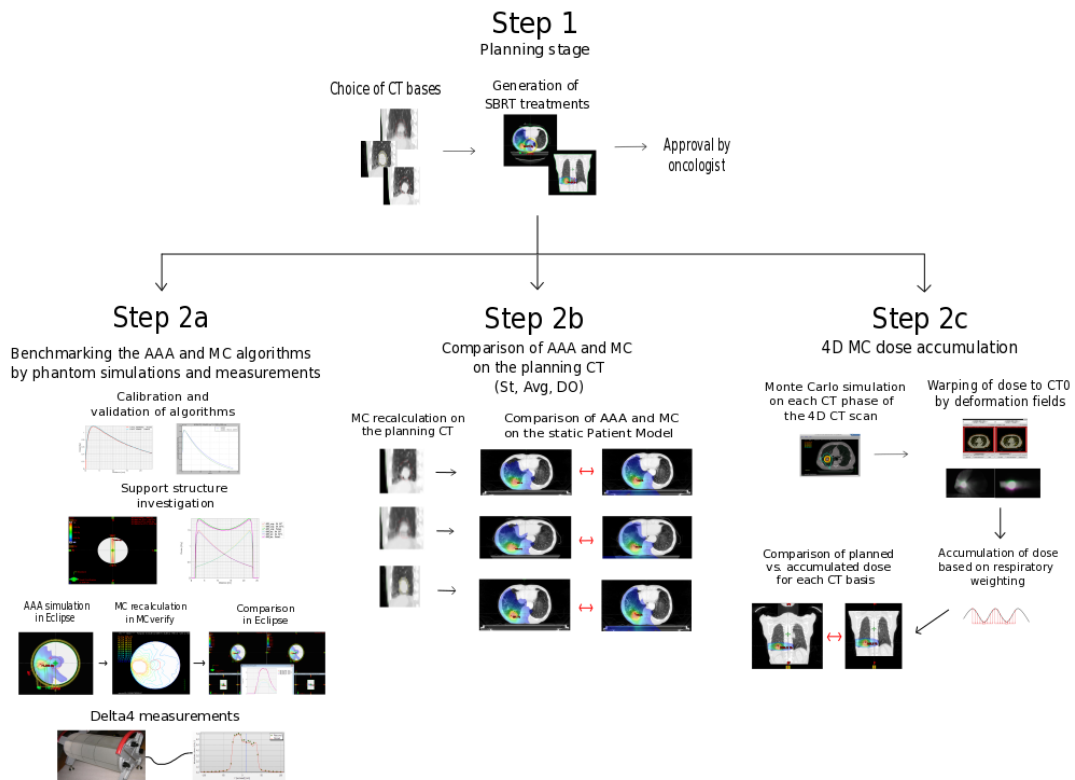
Figure 3.8: Schematic illustration of the work flow of this study [3]. Three CT bases were chosen. Both 6MV and 10MV radiation were utilised, resulting in six new VMAT SBRT treatment plans per person. All treatment plans, in addition to simulations on homogeneous phantoms, were recalculated with the MC algorithm. The treatments regarding patients were also simulated on each CT phase of the 4D CT scan for accumulation of dose distribution. The results were transferred back to $Eclipse^{TM}$ for evaluation.

4 Results

4.1 Phantom Study

4.1.1 Monte Carlo Commissioning

The water phantom depth dose curves are shown in figures 4.1 and 4.2. In addition, the relative dose differences are shown in red. Both 15 MV FF simulations and the 10 MV FFF 3×3 cm^2 simulation have particularly high mean relative dose differences of more than 1 %, with MC results being lower for the 15 MV FF and higher for the 10 MV FFF. The 6 MV FF treatments and the 6 MV FFF 10×10 cm^2 treatments have relative dose differences of about 0.5 %, where the MC values are higher than the AAA for the 10×10 cm^2 modalities and lower for the 3×3 cm^2 modality. The most coincident curves are the 6 MV FFF 3×3 cm^2 and 10 MV FFF 10×10 cm^2 simulations, with a relative dose difference of 0.37 % and 0.36 %, respectively.

    (a)   (b)   (c)   (d)
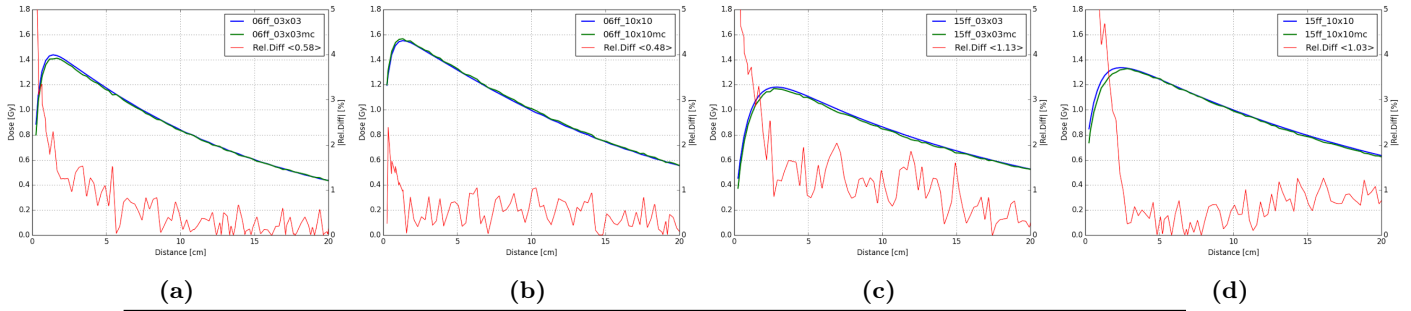
Figure 4.1: Water phantom calibration of beam models including a flattening filter. Relative dose difference is shown in red, where the maximum value of the respective AAA curve is chosen as reference. Settings: (a, b) 6 MV FF and (c, d) 15 MV FF, (a, c) 3×3 cm^2, (c, d) 10×10 cm^2, MU=130, single fraction, total dose of 1 Gy, no normalisation.

    (a)   (b)   (c)   (d)
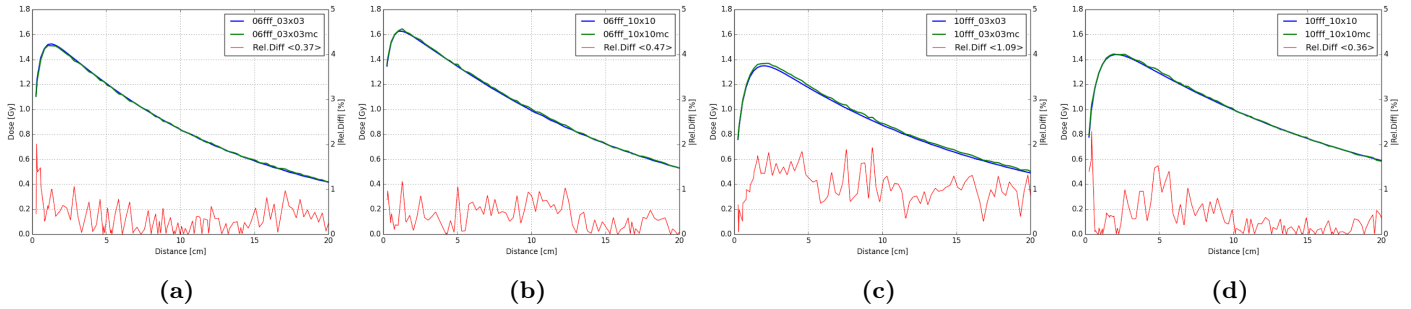
Figure 4.2: Water phantom calibration of flattening filter free beams. Relative dose difference is shown in red, where the maximum value of the respective AAA curve is chosen as reference. Settings: (a, b) 6 MV FFF and (c, d) 10 MV FFF, (a, c) 3×3 cm^2, (c, d) 10×10 cm^2, MU=130, single fraction, total dose of 1 Gy, no normalisation.

Figure 4.3a shows 6 MV FFF 3×3 cm^2 AAA and MC simulations from when the phantom density was changed from water to 1.1433 g/cm^3. It illustrates the different density handling by the algorithms. In figure 4.3b the EGSnrc simulation is given. Beam quality values are listed in table 4.1 (Chap. 2.1.2).
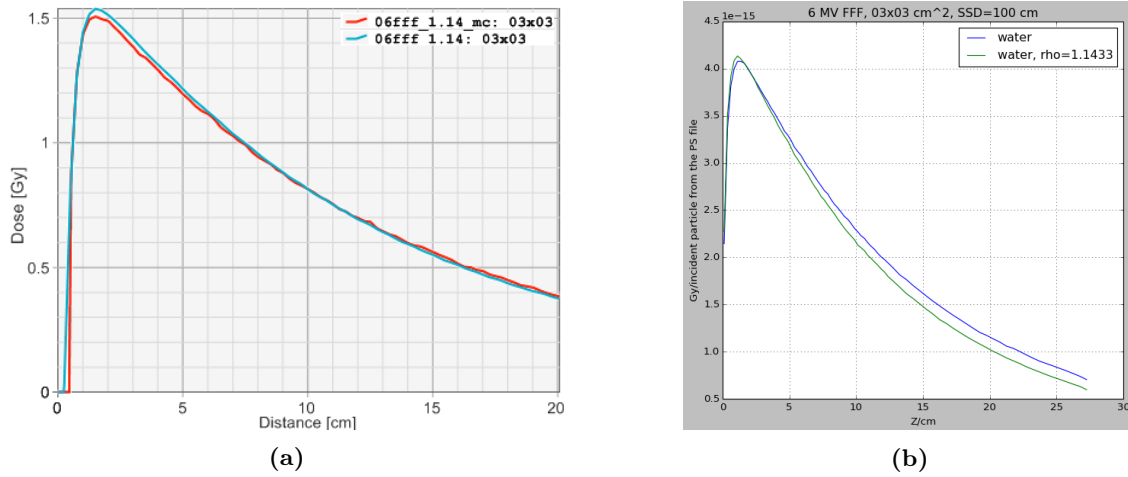
Figure 4.3: Water phantom simulations. (a) Phantom density of 1.1433 g/cm^3, 6 MV FFF beams with field of 3×3 cm. The (red) MC simulation results in approximately the same maximum dose as in water (Fig. 4.2). The maximum dose increases compared to water calculation regarding the AAA simulation (blue). (b) EGSnrc simulation in phantom with water density and density of 1.1433 g/cm^3. The different scaling makes the comparison qualitative. The maximum dose increases with denser material, which coincides with the change in dose calculated by AAA.

Table 4.1: Beam quality values.

|	AAA	MC	EGSnrc
$Q_{\text{water density}}$	0.50	0.50	0.50
$Q_{1.1433g/cm^3}$	0.46	0.47	0.47

4.1.2   Delta4 Simulations, Opposing Fields

Figure 4.4 illustrates the setup when two opposing beams are crossing the *Delta4* phantom. In figure 4.5, the dose profiles of the setup without the treatment couch is shown. In general, the MC algorithm results in lower doses than the AAA calculated distribution. The beams coincides the least for the 15 MV FF beams, while they are almost identical for the 10 MV FFF beams.
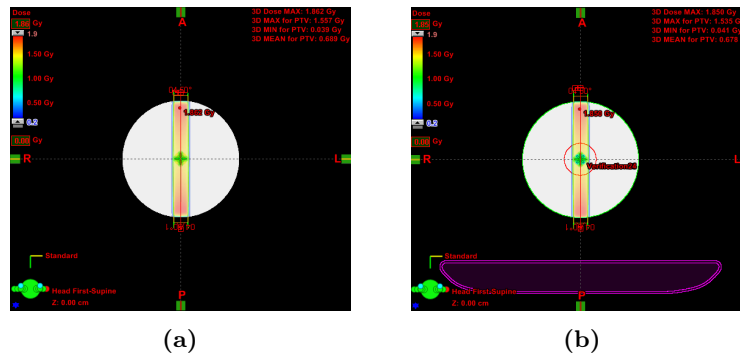
Figure 4.4: Illustration of field setup for opposing fields. (a) No couch, (b) treatment couch included. The dose profiles in figures 4.5 and 4.6 follow the red arrows. $Eclipse^{TM}$ does not show the AAA calculated dose in table by default.

In figure 4.6 the setup also includes the treatment couch. The AAA calculated beam profiles are practically the same as without the couch (fig. 4.5), while the build-up region as well as the local
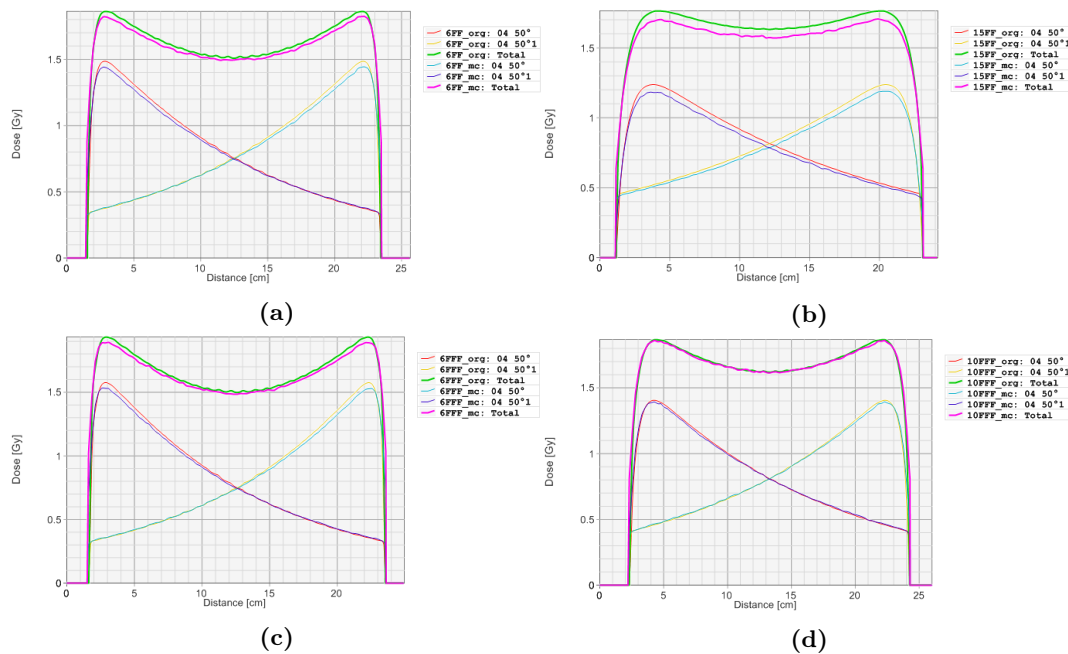
Figure 4.5: Dose profiles along the vertical fields (illustrated in figure 4.4). The treatment couch is not included. (a) 6 MV FF, (b) 15 MV FF, (c) 6 MV FFF, and (d) 10 MV FFF. The green (AAA) and pink (MC) profiles are the sums of their respective fields shown below in the graph. The MC doses are lower or equal to the AAA calculated doses.

maximum towards the table has changed for the MC calculations. The 15 MV FF calculations still deviates the most, while the 10 MV FFF shows the best agreement of total dose.

The relative dose deviations of the vertical simulations are listed in table 4.2. In the profiles of 6 MV FF, 6 MV FFF and 10 MV FFF with treatment couch and 6 MV FFF and 10 MV FFF without, the dose deviation of the total field is lowered due to the crossing of dose profiles towards lower values. For the FF treatments without couch and the 15 MV FF treatment when the couch is included, the AAA dose is always larger than or equal to the dose calculated by MC. On average, the relative dose deviation percentage decreases with 0.35 and increases with 0.65 in the anterior and posterior part of the phantom, respectively, when the treatment couch is included.

Table 4.2: Relative dose deviation in dose profiles of vertical fields. *A* and *P* denotes *anterior* and *posterior* part of the phantom, respectively. The maximum dose of Field 2 lies in the posterior part, i.e. closest to the treatment couch.

	No treatment couch			Couch included		
Treatment	Total [%]	Field1 [%]	Field2 [%]	Total [%]	Field1 [%]	Field2 [%]
6 MV FF	A: 2.1, P: 2.3	2.9	2.8	A: 1.4, P: 2.7	2.3	4.4
15 MV FF	A: 3.4, P: 3.2	4.3	3.8	A: 3.0, P: 3.9	4.0	5.1
6 MV FFF	A: 2.1, P: 2.2	2.6	3.0	A: 1.7, P: 2.9	2.7	4.2
10 MV FFF	A: 0.3, P: 0.4	0.8	0.7	A: 0.4, P: 1.2	1.4	2.4
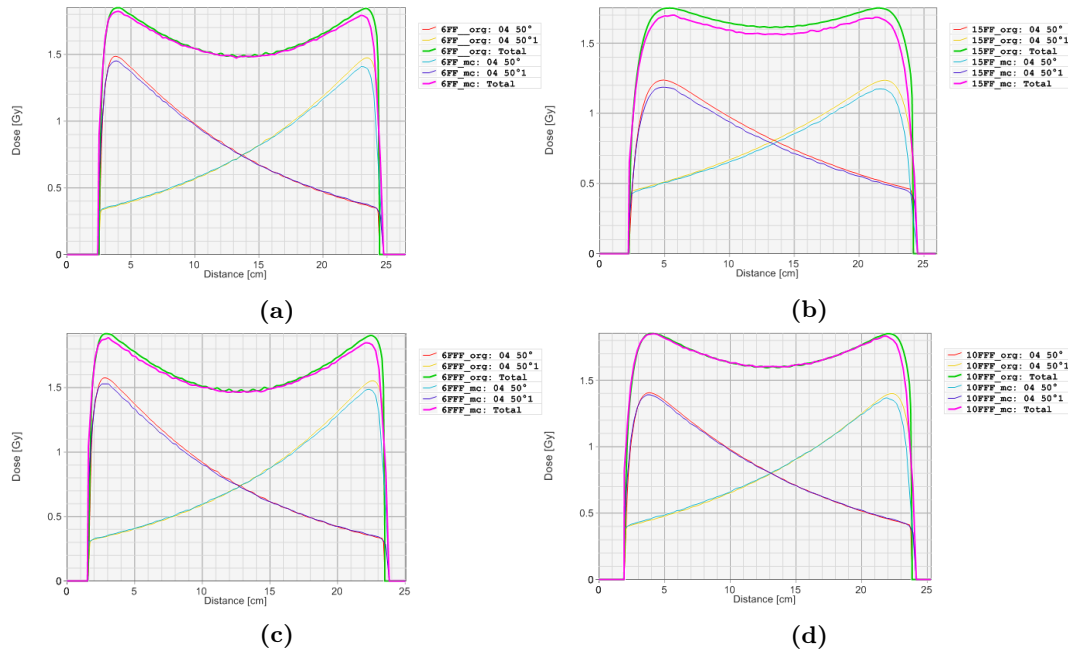
Figure 4.6: Dose profiles along the vertical fields (illustrated in figure 4.4) when the treatment couch is included. (a) 6 MV FF (b) 15 MV FF, (c) 6 MV FFF, and (d) 10 MV FFF. The green (AAA) and pink (MC) profiles are the sums of their respective fields shown below in the graph. The right side of the graphs (posterior part of phantom) is towards the treatment couch.

4.1.3   Delta4 Simulations, Planned Treatments

Figures **??** and 4.5a show a dose distribution calculated on the homogeneous phantom by AAA and MC, respectively. The fields and beam setting are the same as for sbrt05 Original, which comprises only stereotactic 3D-CRT beams and includes the treatment couch. The dose profiles are very similar, but the MC calculated dose distribution has the tendency of being higher (approximately 4 %). The largest deviations are close to the treatment couch. The shifts at the edges are caused by different interpretation of boundary CT pixels by $Eclipse^{TM}$ and MCverify.

Figures 4.8 and 4.9 show two VMAT plans, 6 MV St and 10 MV St, dose simulations on the *Delta4* phantom, respectively. In these cases, the dose profiles and DVHs of AAA and MC are more similar than for the 3D-CRT treatment.

(a) **(b)**

(c) **(d)**

(e)

Figure 4.7: Simulations on a homogeneous phantom to illustrate the agreement between the AAA and MC calculation algorithms. The field setup is the same as for sbrt05 Original. (a) AAA calculated dose distribution, (b) MC calculation. $Eclipse^{TM}$ does not show the AAA calculated dose in table by default. The dose profiles along the (c) horizontal and (d) vertical red arrows illuminates an on average higher dose calculated by AAA than MC. The blue dose profiles are from the MC calculation, while the red profiles are from the calculation by $Eclipse^{TM}$ (AAA). (e) The DVH of the dose distribution shows the homogeneity of the PTV (red) and BODY (green) structures, where AAA are represented by the squares and MC by the triangles.

The maximum values of the distribution in the phantom and the mean value of the PTV structure is listed in table 4.3. Values from simulations when the treatment couch is not included are listed in table 4.4 for comparison. In addition, the relative dose deviations between the AAA and MC calculations, where the respective AAA value is chosen as reference, are presented. The average change in relative dose deviation concerning the max value when the treatment couch is included a 0.20 lower percentage. The percentage of the mean dose is lowered by 0.07.

(a) **(b)**

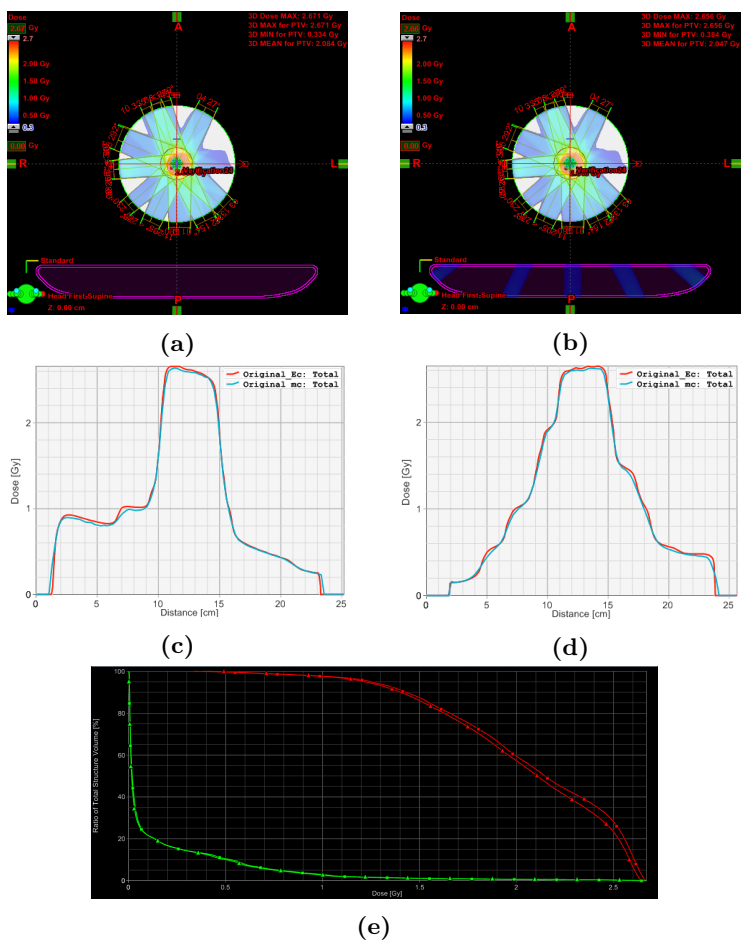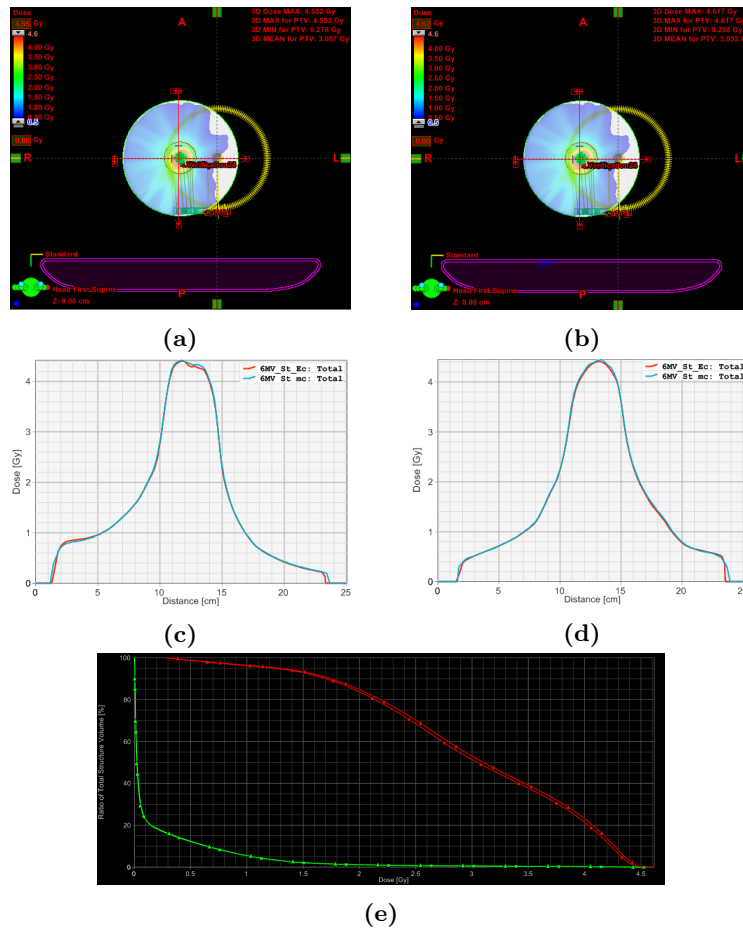**(c)** **(d)**

(e)

Figure 4.8: Simulations on a homogeneous phantom to illustrate the agreement between the AAA and MC calculation algorithms. The field setup is the same as for sbrt05 6 MV St. The (a) AAA calculated dose distribution corresponds well to the (b) MC calculation, more precisely illustrated by the dose profiles along the (c) horizontal and (d) vertical red arrows. The deviation is in the high dose area, where the MC dose is the highest, and at the phantom edges. The blue dose profiles are from the MC calculation, while the red profiles are from the calculation by $Eclipse^{TM}$ (AAA). (e) The DVH of the dose distribution shows the homogeneity of the PTV (red) and BODY (green) structures, where AAA are represented by the squares and MC by the triangles. $Eclipse^{TM}$ does not show the AAA calculated dose in table by default.

Table 4.3: Maximum dose in phantom, mean dose in PTV and the relative dose deviations of each. The deviation reference is set to the respective AAA value and the treatment couch is included in setup.

Treatment	Max$_{AAA}$ [Gy]	Max$_{MC}$ [Gy]	Rel. dev. [%]	Mean$_{AAA}$ [Gy]	Mean$_{MC}$ [Gy]	Rel. dev. [%]
Org	2.671	2.656	0.6	2.084	2.047	1.8
6 MV St	4.552	4.617	1.4	3.007	3.052	1.5
10 MV St	4.675	4.781	2.3	2.814	2.880	2.4

4.1.4 Heterogeneity Correction

The different heterogeneity handling is illustrated by the two fields in figure 4.10. One beam was set to pass through the heart for demonstration of the influence of the density heterogeneities on the dose calculation algorithms. For both plans the prescribed dose was halved to get representative rays.
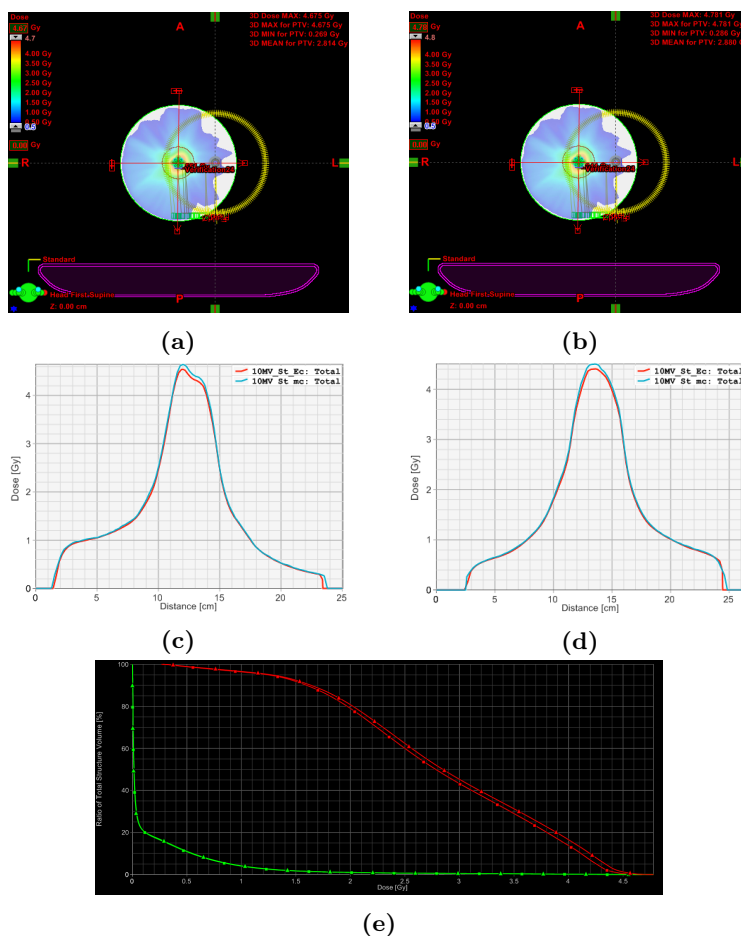
(a)

(b)

(c)

(d)

(e)

Figure 4.9: Simulations on a homogeneous phantom to illustrate the agreement between the AAA and MC calculation algorithms. The field setup is the same as for sbrt05 10 MV St. As for 6 MV FFF (fig. 4.8), the (a) AAA calculated dose distribution corresponds well to the (b) MC calculation, but results in MC doses larger than the AAA calculated doses, illustrated by the (c) horizontal and (d) vertical dose profiles along the red arrows. The blue dose profiles are from the MC calculation, while red blue profiles are from the calculation by $Eclipse^{TM}$ (AAA). (e) The DVH of the dose distribution shows the homogeneity of the PTV (red) and BODY (green) structures, where AAA are represented by the squares and MC by the triangles. $Eclipse^{TM}$ does not show the AAA calculated dose in table by default.

Table 4.4: Maximum dose in phantom, mean dose in PTV and the relative dose deviations of each. The deviation reference is set to the respective AAA value. The treatment couch is not included in the setup.

Treatment	Max$_{AAA}$ [Gy]	Max$_{MC}$ [Gy]	Rel. dev. [%]	Mean$_{AAA}$ [Gy]	Mean$_{MC}$ [Gy]	Rel. dev. [%]
Org	2.727	2.706	0.8	2.121	2.073	2.3
6 MV St	4.597	4.508	1.9	3.029	2.983	1.5
10 MV St	4.734	4.836	2.2	2.844	2.903	2.1

The dose profiles along the arrows in 4.10 are shown in figure 4.11. Along both arrows, the dose profiles show that the MC dose is either lower or the same as the AAA calculated dose. Especially in the low density media in the lungs the MC is lowered.

The perpendicular dose profiles in figure 4.12 clarify the effect of LED. The dose profile in figure 4.12a shows that the electron range is shorter in the costa tissue than in the less dense lung tis-
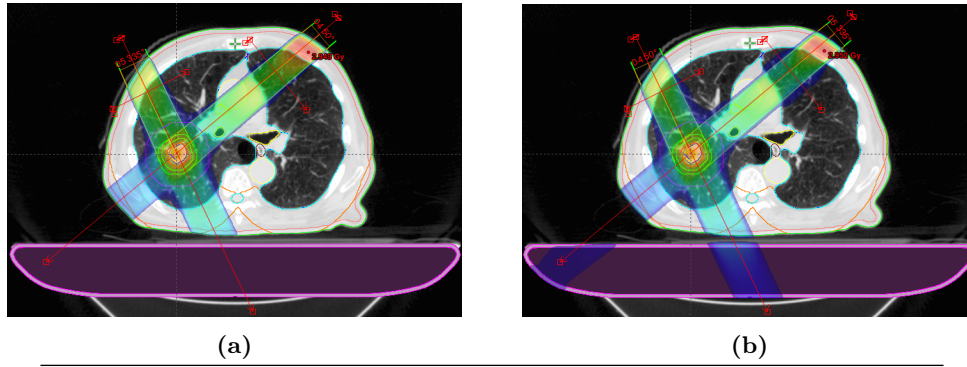
Figure 4.10: Dose distributions calculated by (a) $Eclipse^{TM}$ and (b) MC. There are four red arrows for dose profiles; For each field, one profile that aligns with, and one profile perpendicular to the incoming ray. $Eclipse^{TM}$ does not show the AAA calculated dose in table by default.
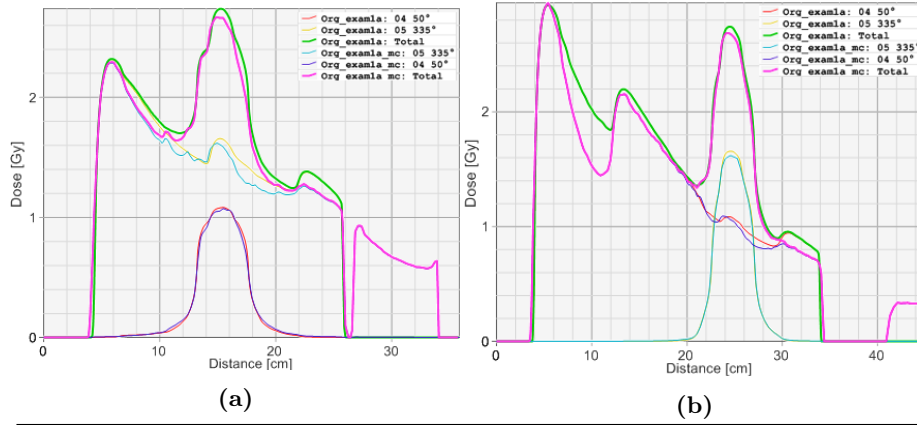
Figure 4.11: Dose profiles showing dose profiles from both separate fields and the total dose. Equally weighted fields from the angles (a) $335°$ and (b) $50°$. The total $Eclipse^{TM}$ and MC calculation are shown in green and pink, respectively.

sue, resulting in reduced absorbed dose towards the lung tissue when calculated by MC. Figure 4.12b, where the profile is spanning through mostly lung tissue, illustrates how the lateral electron movement contributes to a considerably lower maximum MC dose with respect to AAA calculated dose. In this case, the lateral spread of dose deviates significantly between AAA and MC.

4.1.5   Delta4 Measurements

The *Delta4* measurements resulted generally in a measured dose slightly higher than the AAA planned dose. Figure 4.13 shows a representative illustration of the planned (AAA) and measured dose comparison.

The γ indices of all treatment plans are listed in table 4.5. A prominent result is that the AAA calculated dose resulted in higher γ indices than the MC calculated predicted. No total MC treatment plans have high enough gamma indices to be approved, even though each separate field fulfil the criterion. The lowered gamma index is mostly caused be the *distance to agreement* criterion (± 3 mm), where the sum of the errors results in the unapproved total plan.

(a)   **(b)**

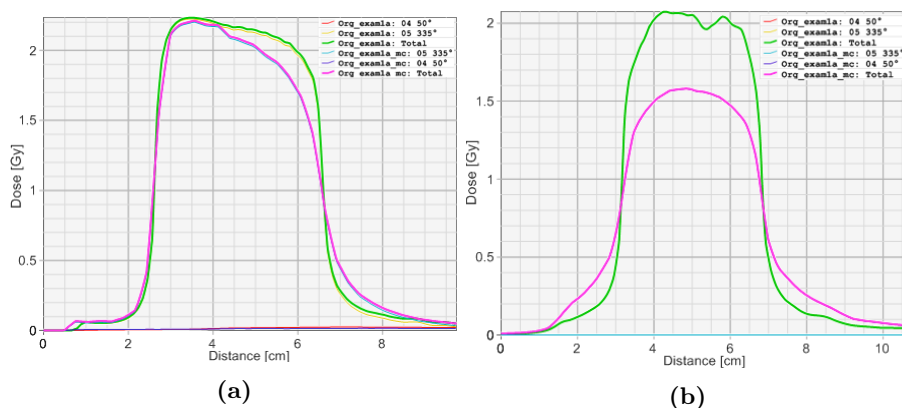**Figure 4.12:** Dose profiles perpendicular to the (a) $335°$ filed and (b) $50°$ field, illustrating the lateral diffusion in lung tissue. The total $Eclipse^{TM}$ and MC calculation are shown in green and pink, respectively.

Table 4.5: Gamma indices, VMAT treatments, patient sbrt13. The gamma indices falling below the 95% limit are marked in red.

Treatment	Field	AAA persentage with $\gamma \leq 1$ [%]	MC persentage with $\gamma \leq 1$ [%]
6 MV Avg	Total	95.6	89.9
	$340°$ to $179°$	99.5	95.4
	$179°$ to $340°$	98.6	97.6
6 MV DO	Total	96.6	92.6
	$340°$ to $179°$	99.2	99.2
	$179°$ to $340°$	98.9	98.9
6 MV St	Total	97.1	90.5
	$340°$ to $179°$	99.2	97.2
	$179°$ to $340°$	99.5	97.5
10 MV Avg	Total	98.5	94.3
	$340°$ to $179°$	99.2	98.4
	$179°$ to $340°$	100.0	99.0
10 MV DO	Total	97.4	93.5
	$340°$ to $179°$	97.7	97.2
	$179°$ to $340°$	100.0	99.5
10 MV St	Total	98.1	92.8
	$340°$ to $179°$	100.0	99.7
	$179°$ to $340°$	100.0	98.9

4.2   Static Patient Model MC Simulation

In the case of patient calculations (where the treatment couch always was included), the heterogeneous media resulted in larger deviations between the AAA dose calculation and the calculation performed by MC. Figure 4.14 shows representative *sum plans*, where the dose distribution calculated by $Eclipse^{TM}$ is subtracted from the MC dose distribution. The purple areas are illustrating a lower dose calculated by MC, while the green areas are where the MC calculation results in a higher dose. The red and light blue areas, generally located in the same lung as the tumour, are areas where the dose calculated by MC deviates with up to $\pm 10\%$ of the maximum value of the AAA dose. The remaining sum plans of all patients can be found in Appendix 8.6.
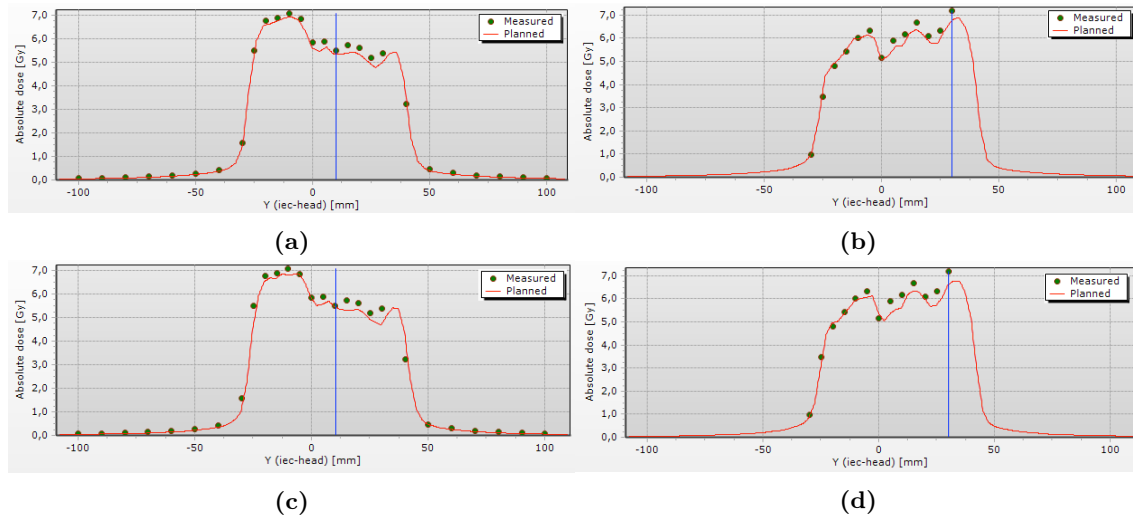
Figure 4.13: Dose profiles from central part of the Delta4 phantom for sbrt13, 6 MV Avg. (a, c) First detector plane and (b, d) second detector plane. The measured doses are represented by green dots and the predicted dose by the red line. (a, b) AAA calculated dose, 99.5% of points passing γ criterion (Chap. 2.4.5). (c, d) MC calculated dose, 95.4% passing the γ criterion.

In general, the dose calculated by MC in the target area is larger than the AAA calculation for small tumours and smaller than AAA doses for large tumours. Due to this observation, the field sizes were further investigated. Figure 4.15 depicts momentary field sizes of the sbrt05 10 MV Avg and sbrt13 6 MV Avg treatments. Figure 4.15a illustrates the field size of the sbrt05 treatment when the entire tumour is irradiated, with maximum field span of about 4-5 cm in each direction. In figure 4.15c the field size of the sbrt13 treatment is ranging from 5 cm to more than 7 cm in the directions aligning and perpendicular to the MLC leaves, respectively. However, as the MLC configuration is continuously changing during treatment, the field size can be very varying, illustrated my another momentary MLC configuration of sbrt05 in figure 4.15b.

4.3   Verification

Figure 4.16 shows a representative dose distribution that illuminates the core of this project. In figure 4.16a the dose distribution of sbrt01 6 MV St is calculated by MC on the CT0 basis. The yellow lines in figure 4.16b indicates the extent and direction of specific parts of the deformation field in that specific plane used to warp the CT50 dose to the CT0 anatomy. The result is shown in figure 4.16c, where the treatment plan is calculated on the CT50 basis, whereafter the dose distribution is warped to the CT0 anatomy. Compared to the dose distribution in figure 4.16a, the shape of the distribution is no longer as conform around the red PTV surface. The dose to the diaphragm has increased, while the dose to the superior part of the PTV has decreased.

The tumour shift in the CT images due to respiration could be visualised by the *Matcher 3D* program. The example in figure 4.17 is from sbrt01, CT phase CT50 (maximum exhalation). When starting out with two identical dose distributions, where one had the colour green and the other the colour pink, their colours cancelled each other out, which resulted in the completely white dose distribution shown in figure 4.17a. Then, after applying the deformation field, the dose of CT50
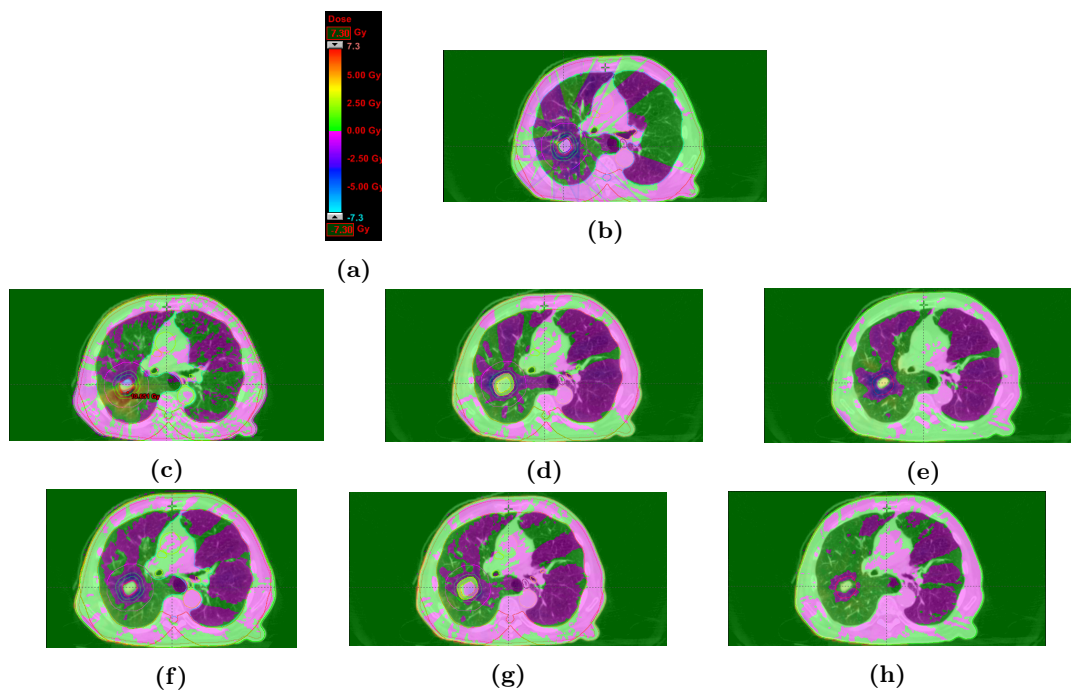
Figure 4.14: Sbrt12: Summed plans, where the Eclipse simulation is subtracted from the MC simulation. The colour scale is ranging from +10% to −10% of the maximum dose of the original plan. (a) Illustrating colour scale (varying slightly for each sum plan), (b) Original plan, (c) 6MV Avg, (d) 6MV DO, (e) 6MV St, (f) 10MV Avg, (g) 10MV DO, and (h) 10MV St.

was warped to the position of CT0 (the reference image), illustrated in figure 4.17b. The visualisation of these shifts where used to control that the dose from every CT phase was correctly shifted.

A visualisation of dose distributions and the corresponding vertical dose profile is shown in figure 4.18. This is a representative illustration of how the occurrence of conformity deviations (presented in figure 4.16) leads to an overall lack of high dose in the superior part of the PTV structure when accumulating the dose. In addition, the inferior part of the dose distribution gets a small shift towards the diaphragm.

Figure 4.19 shows coronal views of the accumulated dose, calculated for all treatments concerning patient sbrt01. In all cases, the superior part of the PTV structure has a lower dose than the prescribed dose value. For the Original treatment, a very small part of the superior volume of ITV also receives less than the prescribed dose. The dose distributions of the Original and 10MV Static treatments excels as the dose distributions with lowest values. Visualisations of the accumulated dose distributions for the remaining patients can be found in Appendix 8.7.
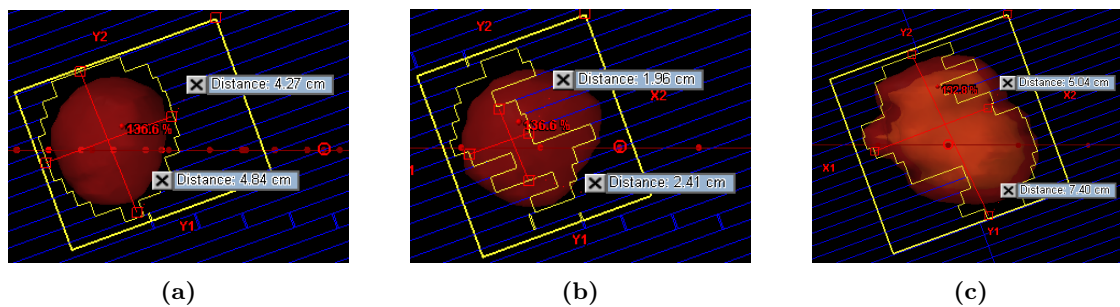
Figure 4.15: Illustration of variation in field size for the evaluated treatments. Momentary MLC configurations of (a, b) sbrt05 10 MV Avg and (c) sbrt13 6MV Avg.

4.4 Conformity Indices

Figure 4.20 shows box plots of the conformity indices, calculated by Paddick's definition (section 2.4.1)[1]. In figure 4.20a it is clear that the VMAT treatments are more conform than the Original treatments. The MC calculation leads to conformity indices both closer and further away from unity, seen in figure 4.20b, while the conformity indices resulting from the accumulated dose are all lower values than in the planned calculation. The outlier in accumulated dose origins from patient sbrt14, where the ITV size is 1.7 cm^3. As seen below in figure 4.21 and figure 8.10b in Appendix 8.7, the MC algorithm results in a less sharp penumbra than AAA in the lung-tumour density interface. It should be noted that the *Planned* dose distributions always are calculated on the planning CT set, while the *Accumulated doses* always are calculated on the CT0 phase set from the 4D-CT scan. A description of how the box plots are calculated can be found in Appendix 8.5.

4.4.1 PTV and ITV Coverage

The fraction of the PTV receiving the prescribed dose, averaged over each treatment modality, are presented in figure 4.21. In figure 4.21a, the statistics from the planned dose distributions are shown. The VMAT plans are normalised to 95% prescribed dose coverage of the PTV structure, and thus has no deviation. This normalisation value is one of the factors resulting in the deviation from unity for the VMAT treatments seen in figure 4.20a. Increasing the normalisation value to e.g. 98% could have improved the conformity of the VMAT plans. The large fraction of the PTV structure receiving the prescribed dose using the Original modality implies that the deviation from an index of unity is more due to spilling of dose to healthy tissue rather than lack of dose to the target volume.

Figure 4.21b describes the planned dose distribution calculated by MC, resulting in both elevated and decreased PTV coverage. Especially the dose coverage in the Original (3D-CRT), 6 MV Avg and 6 MV St treatments decreased, of which the VMAT treatments resulted in the lowest PTV fractions receiving the prescribed dose considering the deviation span. The outlier among the 10MV DO treatments is from patient sbrt14, where the deviation is more due to the the precision of the other treatments rather than an abnormal lack of dose coverage. Figure 4.21c shows statistics from the accumulated dose distribution, where all fraction values are considerably lowered compared to the planned treatments. The 6M DO treatment has the lowest mean value, while the

---

[1]The data presented in tables and graphs in this section are collected from the DVHs of the patients.
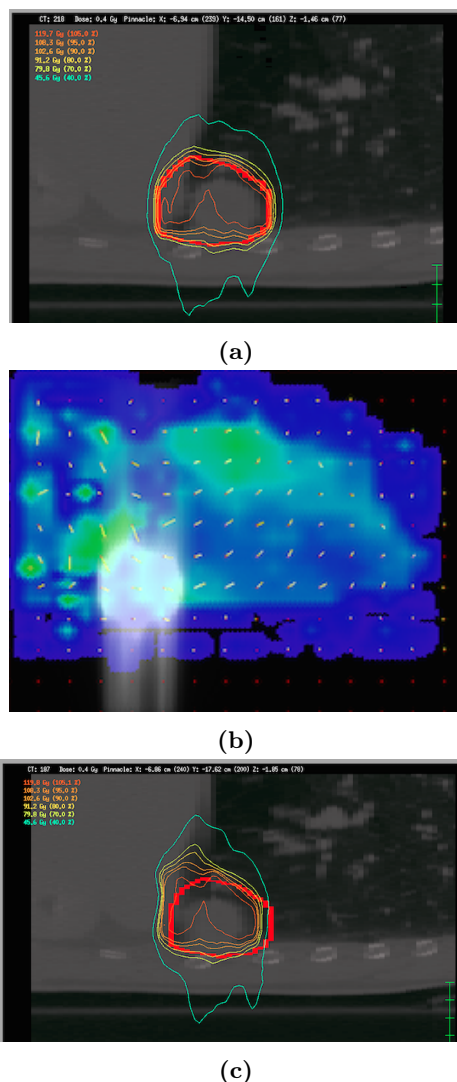
(a)

(b)

(c)

Figure 4.16: Sbrt01 6 MV St. (a) MC calculated dose distribution on the CT0 basis. (b) Deformation field between CT50 and CT0. (c) MC calculation on the CT50 basis warped to the CT0 anatomy by the deformation field. All are sagittal images from the same area, where the CT images (a and c) have the PTV structure marked in red. The dose distribution is marked with isodose lines in the images from *Hyperion*, while it is shown in white in the deformation field of *Matcher 3D*. The blue colours of the deformation field illustrates the absolute value of the 3D deformation while the yellow lines show the deformation direction and extent in the chosen plane.

Original treatment has the lowest values considering the deviations.

Figure 4.22 shows the mean dose to ITV, averaged over each treatment modality. The planned treatments calculated by $Eclipse^{TM}$ in figure 4.22a illustrates an in general higher dose to the ITV using VMAT treatments compared to the Original 3D-CRT treatment. When calculating with MC, all treatment modalities, except the 10 MV Avg, have elevated mean values, as shown in figure 4.22b. An accumulation of the MC dose distribution is shown in figure 4.22c. In all cases the mean dose is lowered compared to the planned MC simulation. In Appendix **??** DVHs give further illustration if the dose received by the ITV.

(a)   (b)
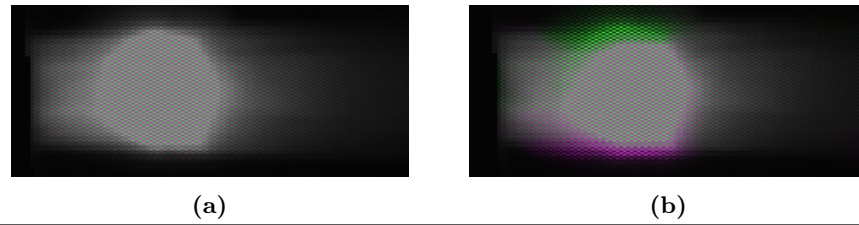
Figure 4.17: Deformed dose distribution example from sbrt01, 6MV Avg, CT50, illustrating the deformation of dose distribution performed by *Matcher 3D*, coronal view. Grey and white pixels show identical dose values of two dose distributions overlaid on each other. (a) Two identical dose distributions of CT50 cancel out their pink and green colour into white. (b) The dose distribution in pink was warped to the CT0 basis, while the dose distribution in green was kept aligned to CT50.

(a)   (b)   (c)
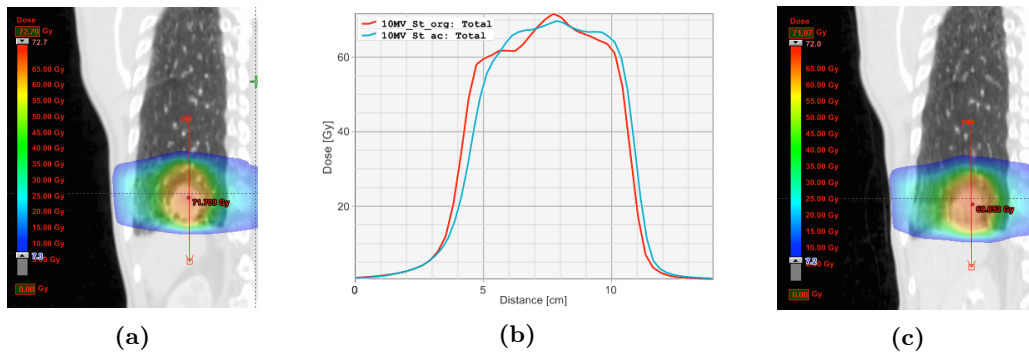
Figure 4.18: Coronal CT images from sbrt01 10MV StaticCT calculated by the MC algorithm (a) on the static CT basis and (c) on each CT basis, and then accumulated. The (b) dose profile illuminates the lack of dose in the superior part of PTV and how the dose is shifted to tissue inferior of the PTV.

4.4.2 Dose to Costa and Lung Tissue

The deviation from a conformity value of unity for the VMAT plans can also be illuminated by figure 4.23. It illustrates that the lack of dose to the PTV is in the same area as the Costa structure, provoked by the priority in the optimisation algorithm.

Table 4.6 summarises the dose statistics of all treatments. As implied by the conformity indices in figure 4.20, the VMAT treatments result in less dose to the adjacent lung and the Costa structure. Regarding the dose to the contralateral lung, the values are approximately equal.
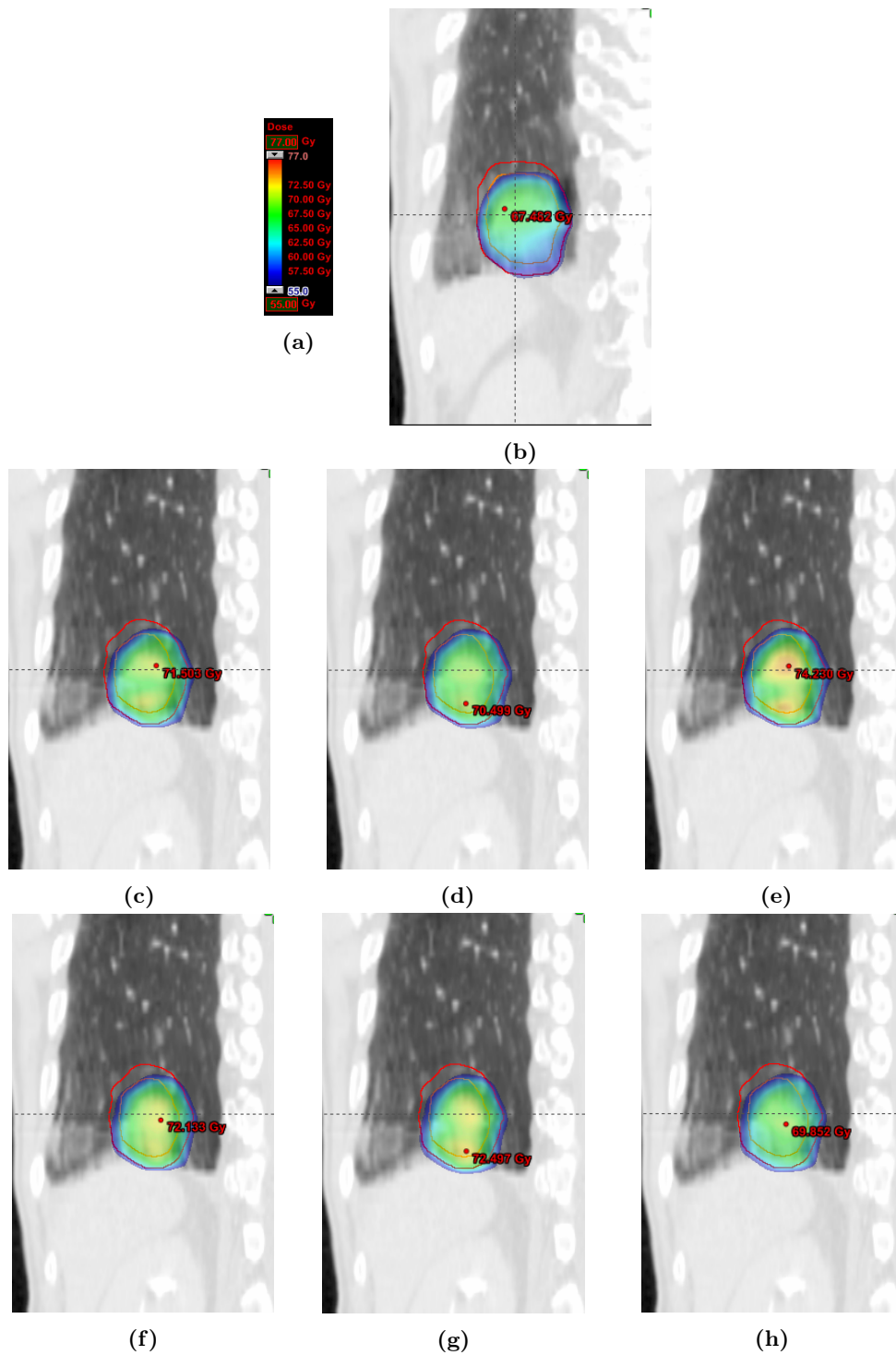
Figure 4.19: Sbrt01: Accumulated dose. (a) Colour scale, ranging from prescribed dose (55.0 Gy) to the maximum optimisation value of 140% (77.0 Gy). (b) Original plan, (c) 6MV Avg, (d) 6MV DO, (e) 6MV St, (f) 10MV Avg, (g) 10MV DO, and (h) 10MV St. The ITV structure is delineated in orange and the PTV structure in red.
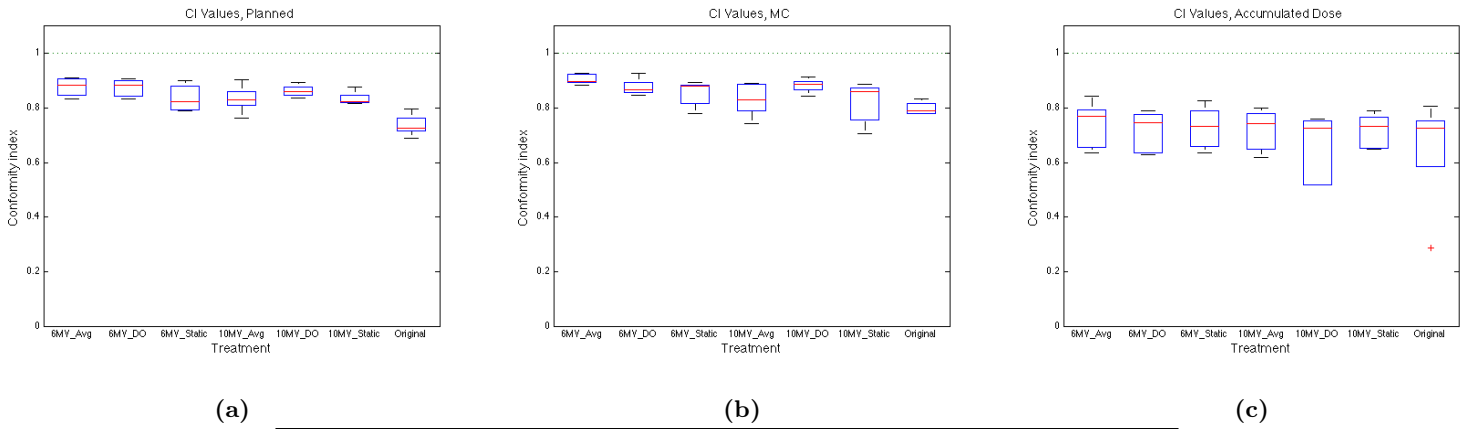
Figure 4.20: The conformity indices of the different treatment modalities. (a) Planned treatments calculated by AAA in $Eclipse^{TM}$, (b) planned treatments calculated by MC, and (c) accumulation of the MC calculation. The outliers of both the 10 MV DO and Original treatments are the CI values of patient sbrt14.
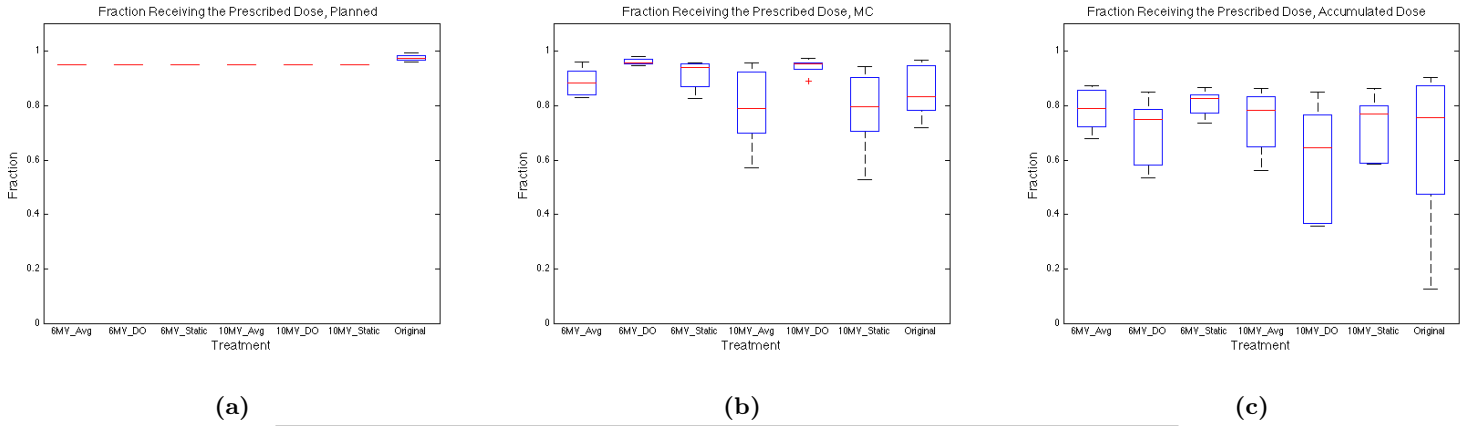
Figure 4.21: Fraction of PTV getting the prescribed dose. (a) Planned treatments (AAA), (b) MC calculated treatments and (c) the accumulated dose with CT0 as basis. The outlier origins from patient sbrt14.
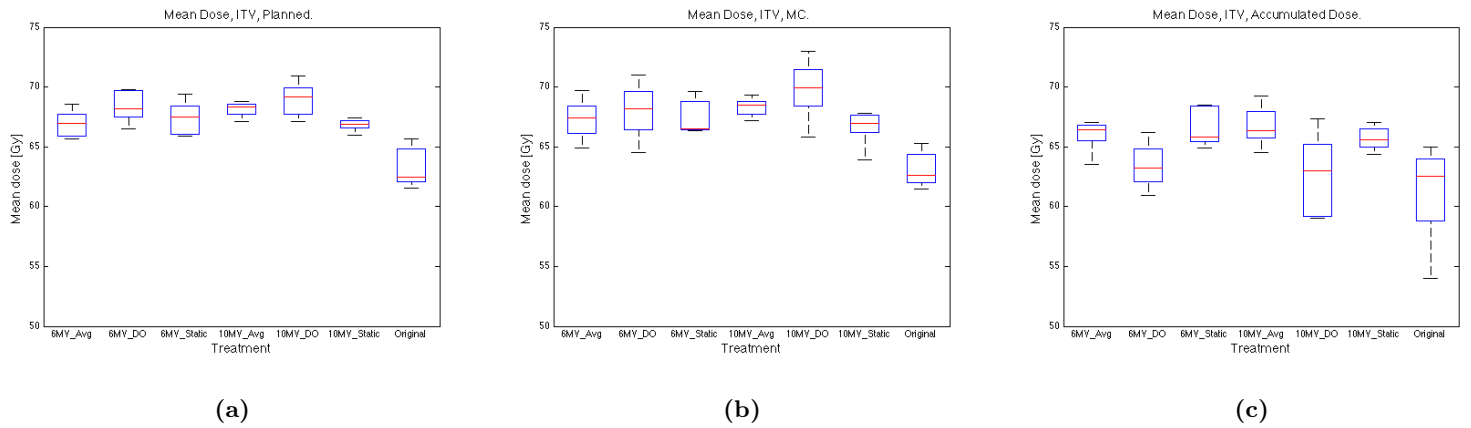
Figure 4.22: Mean dose to ITV. (a), Planned treatments (AAA), (b) MC calculated treatments and (c) accumulated MC dose distribution. The red line shows the median value, while the edges of the box are the 25th and 75th percentiles. The whiskers extend to the most extreme data points not considered outliers.
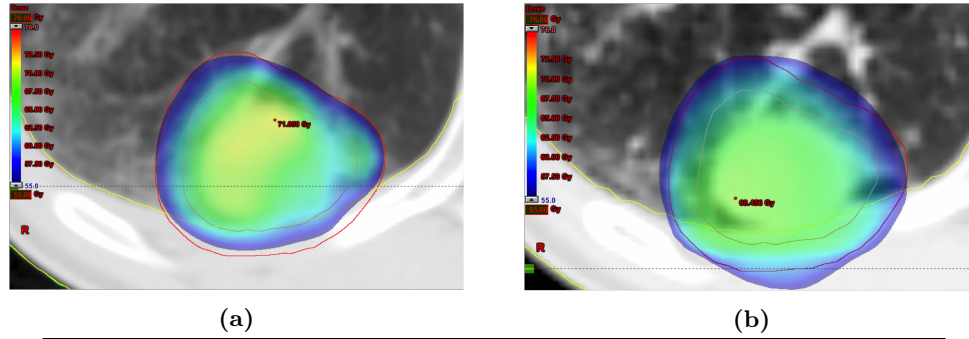
Figure 4.23: The dose shown in identical colour scales for patient sbrt01. The 10 MV Avg treatment is to the left, while the Original treatment is to the right. The lack of dose to the PTV by the VMAT treatment is in the same area as the Costa structure. The lower limit of the colour scale is the prescribed dose (55 Gy).

Table 4.6: Mean values with standard deviation of all treatment plans.

|	CI	PTV cover [%]	Mean ITV [Gy]	Adj. lung [Gy]	Con.lat. lung [Gy]	Costa [Gy]
Planned						
6MV Avg	0.88±0.03	95±0	66.9±1.2	5.0±2.1	0.9±0.4	3.1±1.7
6MV DO	0.87±0.03	95±0	68.4±1.4	5.3±2.3	0.9±0.3	3.1±1.7
6MV St	0.84±0.05	95±0	67.4±1.4	5.5±2.4	1.0±0.4	3.2±1.7
10MV Avg	0.83±0.05	95±0	68.1±0.6	5.3±2.1	1.0±0.4	3.2±1.8
10MV DO	0.86±0.02	95±0	68.9±1.5	5.4±2.2	1.0±0.4	3.1±1.7
10MV St	0.84±0.03	95±0	66.8±0.5	5.7±2.4	1.0±0.4	3.2±1.8
Original	0.74±0.04	98±1	63.3±1.7	6.6±2.7	0.9±0.7	3.7±2.0
MC						
6MV Avg	0.91±0.02	89±5	67.3±1.8	5.1±2.0	1.0±0.4	3.2±1.8
6MV DO	0.88±0.03	96±1	68.0±2.4	5.4±2.2	0.9±0.4	3.1±1.7
6MV St	0.85±0.05	91±6	67.5±1.5	5.6±2.3	1.0±0.4	3.2±1.7
10MV Avg	0.83±0.06	79±15	68.3±0.8	5.5±2.1	1.0±0.4	3.2±1.8
10MV DO	0.88±0.03	94±3	69.8±2.6	5.5±2.1	1.0±0.4	3.1±1.8
10MV St	0.82±0.08	79±16	66.7±1.6	5.8±2.3	1.1±0.4	3.3±1.9
Original	0.80±0.02	85±10	73±36	6.6±2.7	0.9±0.7	3.7±2.0
Accumulated						
6MV Avg	0.74±0.09	79±8	66.0±1.4	5.3±1.9	0.9±0.4	2.8±1.2
6MV DO	0.71±0.08	70±13	63.4±2.0	5.1±2.0	0.9±0.3	2.7±1.2
6MV St	0.73±0.08	81±5	66.7±1.7	5.4±2.1	1.0±0.4	2.8±1.2
10MV Avg	0.72±0.08	74±12	66.8±1.8	5.5±1.9	1.0±0.4	2.8±1.2
10MV DO	0.65±0.12	59±22	62.6±3.6	5.2±1.9	1.0±0.4	2.7±1.2
10MV St	0.72±0.06	72±12	65.7±1.0	5.6±2.1	1.0±0.4	2.9±1.2
Original	0.65±0.21	65±32	61.1±4.3	6.3±2.5	0.9±0.7	3.1±1.3

5 Discussion

5.1 Phantom Study

5.1.1 Monte Carlo Commissioning

All MC beam models, except the 15 MV FF beam model, shows good agreement with the AAA doses calculated. Among the treatment plans investigated only three beams of the 15 MV FF modality was used, which was in the case of the sbrt01 Original plan. The Original treatments using FF beams are mostly used as reference for the generated VMAT plans. Hence, the major part of the results are based on calculation with 6 MV FFF and 10 MV FFF beams, for which symmetric errors up to 2 % relative to maximum can be observed.

The sbrt01 and sbrt13 are the cases with the largest tumours, and the ones most probable to be affected by the 10×10 cm^2 calibration in our study. In that case, we can expect an MC dose with a relative dose deviation of about 0.3 % to 0.5 % higher than the AAA calculated dose. However, none of the treatments have field sizes of this extent, and would probably be most affected by the 3×3 cm^2 calibrations. For small fields, MC would be expected to have a relative dose deviation of about 0.3 % to 0.5 % lower than the AAA calculated dose for 3D-CRT and VMAT plans.

The EGSnrc calculation has coincident Q values with the AAA and MC calculations, implying that the slope of the dose tail simulations are similar. This ensures that the dose calculated with AAA and MC in a homogeneous phantom will result in resembling dose distributions. However, the MC calculation does not result in an elevated maximum dose when calculated in a denser material, which indicates that the MC algorithm has to be further developed regarding density handling in order to get a better agreement in the build-up region. Possibly, a lower MCvariance could be utilised to validate the algorithm. The AAA appears to correspond to the maximum dose shift in EGSnrc, implying that its density handling is suitable.

5.1.2 Delta4 Simulations, Opposing Fields and Planned Treatments

When the phantom is simulated without the treatment couch, the MC calculation results in lower doses than AAA, as would be expected from the calibration depth dose curves (Chap. 5.1.1). Introducing the treatment couch, the only change is in the dose normalisation factor regarding AAA calculations, while the MC calculations have changes in both build-up and maximum value. This implies a need for different material selection for AAA and MC in order to achieve similar attenuation effect of the couch[48].

Using several beams, the relative impact on the total dose by the treatment couch is reduced. This implies that the VMAT treatments evaluated in this study for the purpose of SBRT treatment can be expected to be influenced by the couch structure to a relative dose deviation of maximum value and mean value of less than 0.2 %, as illustrated in figure 4.9d. Further, the AAA calculated dose of the 3D-CRT treatment is larger than the MC dose in the high dose area, whereas the case is the opposite for the VMAT treatments. This can probably be explained by the field sizes, as the 3D-CRT modality has a static configuration in the range of the field sizes calibrated, while the VMAT MLC configuration is continuously changing and can result in very small field sizes (Chap. 4.2). Verification measurements at HUH regarding fields of 1×1 cm^2 illuminates an MC dose calculation slightly higher than the AAA calculated dose. This is due to the beam model used for MC calculations, which could be corrected by adjustment of the planning photon source size or

transmission parameters of the MLC such as leaf transmission and minimum leaf gap [44].

5.1.3   Heterogeneity Correction

The difference between AAA and MC regarding the LED effect is very prominent in the heterogeneous tissue evaluated, which was expected from literature [25]. Considering VMAT treatment of lung cancer, these tissue density variations are to be expected and should be carefully accounted for when planning. An unfavourable outcome if the effect is not considered is the underdosage of the target volume, as illustrated in figures 4.11 and 4.12, causing reduced tumour control probability.

5.1.4   Delta4 Measurements

The problem of the VMAT measured dose values by the *Delta4* phantom being slightly higher than the AAA predicted values are well known at HUH and under investigation. One hypothesis is that the HU values of the CT data in Eclipse are incorrect. Another hypothesis is that the beam data used to commission the beam model of AAA is insufficient, resulting in wrong estimation of the output factor for small and complex VMAT segments.

The MC calculated dose resulted in doses even lower than the AAA values and had no total treatments approved, though all individual arcs passed. As the DTA was the main cause of the low gamma indices, this can be related to the fact that the DTA criterion was ± 3 mm, while the dose grid size of the AAA and MC calculations was 2.5 cm^3. Decreasing the MC calculation dose grid size and MCvariance value, i.e. limiting the dose variance, the MC treatments could might obtain higher gamma indices. Reduction in dose grid size could also be performed for the AAA calculation, though it does not seem necessary due to the high percentage of dose points passing the gamma criterion.

5.2   Static Patient Model MC Simulation

5.2.1   Visual Inspection

Evaluating the *sum plans* visually, the larger tumours of sbrt01 and sbrt13 seem to have the most equal AAA and MC dose distributions. The rest of the patients with small tumours surrounded by low density lung tissue has larger deviations, as would be expected based on the observations of different heterogeneity corrections (Chap. 4.1.4), due to the larger impact of the LED effect. This is also found in the dose fall out, where the LED effect lead to a less step slope (Appendix 8.8). With the exception of patient sbrt13, the similarities between AAA and MC tend to decrease with increased energy, emphasised by the DVHs in Appendix 8.8, which corresponds to the findings of Aarup et. al.[5].

Comparing the AAA and MC doses, the fact that the MC dose is higher for small tumours and lower for larger tumours can be seen in relation to the *Delta4* simulations and measurements. For patient sbrt05, the field sizes utilised were adjusted to a tumour with an ITV size of 28.49 cm^3, and had thus small field sizes shaped by the MLCs, resulting in an MC dose higher than the AAA calculated dose in the target area. The *Delta4* measurements were performed with verification plans from sbrt13, designed to the treatment of an ITV size of 117.92 cm^3. The result was MC simulated doses of lower values than the measured doses. These observations corresponds well to

the findings in the *sum plans*.

An option to improve the dose calculation around the tumour is to set a smaller calculation grid in the PTV area, and thereby increase the dose accuracy without reaching an unacceptable simulation time.

5.2.2   Evaluation of CI and dose to PTV, ITV and OARs

Regarding CI values, all VMAT modalities appear to be a better option than the 3D-CRT treatment. Recall that the prescribed dose criterion was set to 95 % during planning, hence an elevated criterion could further improve these CI values. The DO treatment modalities have particularly good agreement between the AAA and MC calculated doses, with mean dose difference in CI values with less than 2 %. However, it appears to be no prominent difference among the CT bases, but rather between the choice of either 3D-CRT and VMAT technique. Figure 8.16 in Appendix ?? clearly illustrates the effect of a small ITV in relation to the PTV when using the DO CT basis. Even though the AAA and MC dose distributions become very similar using the DO basis, the change of lung density in such a large fraction of the target volume results in an unrealistic possibility of dose build-up.

Considering the lungs and costa, the 3D-CRT results in the highest dose to the adjacent lung and implies that the VMAT treatment is preferable. However, the differences are very small, and not conclusive when choosing modality.

5.3   Verification

5.3.1   Visual Inspection

As demonstrated in *Matcher3d* (Chap. 4.16), there is a distinguished difference in dose distribution when the target is in motion. The visualisations of the accumulated doses did all show the tendency of lacking dose in the outer part of the PTV. In the case of sbrt05 and sbrt13, all plans have less than prescribed dose to the ITV, while the Original treatment plan of sbrt14 has an alarmingly small dose to the tumour tissue. Both the Original and the DO treatments stand out from the others by having in general both low dose values to tumour volume and an insufficient ITV coverage.

5.3.2   Evaluation of CI and dose to PTV, ITV and OARs

Considering the CI values, all treatments show equal level of conformity with values approximately between 0.71 and 0.74. The exceptions are the 10 MV DO and Original treatments, having a CI value of about 0.05 lower. Regarding both PTV coverage and ITV mean dose, the DO and Original treatments appear to have lowest values. The dose given the OAR are regarded as negligible, as they are far below the dose limitation criteria at HUH.

5.4   Considerations

A challenge by evaluating the accumulated dose is that there is no CTV delineation. As the CTV is not utilised during clinical treatment planning, none of the treatments included the structure. Further, the delineation of the structure was considered as a potential deceptive basis of observation. Delineating the structure in the static breath hold and average image would possibly lead to two different volumes, as the anatomy in the 4D-CT images are less defined, resulting in a smeared out tumour presentation. In addition, the CTV described by the breath hold image may not be at the same position as a CTV delineated in any of the phases of the 4D-CT scan, as patients often find it difficult to precisely comply with breathing instructions. Therefore, the most specific definition of the tumour in these images is the ITV, which is more robust to these uncertainties. However, the main purpose of the ITV is to take into account the internal movement. By accumulating the dose, the aim is to eliminate the major part of the internal movement. Hence, accumulating the dose and then comparing the dose distribution to a target structure enlarged due to movement margins result in a misleading measure of dose coverage. "Shrinking" the target structure by regarding the ITV as the "new PTV" would not be a proper option, as the ITV has an elliptical shape due to the respiratory motion, and thus does not have symmetrical margins around the CTV.

It can be argued that the choice of reference images should have been CT50 instead of CT0. Even though all images of the 4D-CT phases are more blurred than the breath hold image, the CT0 images can be slightly more indistinct than the CT50 images, caused by the increased tumour velocity in the inhalation phases. In addition, the CT50 images are from the maximum exhalation of the free breathing respiration curve, and are thus from the phase that should coincide with the breath hold image. However, this is not necessarily the case. For instance, in the case of patient sbrt01, the breath hold images where most similar to the CT0 phase.

When accumulating the doses, we assume no variation from fraction to fraction, which would have lead to a more "smeared out" dose distribution than evaluated here. In that case, the high doses would decrease while the adjacent tumour or lung tissue would increase their received dose. This could result in a more conform dose to the target area, in the case of a centred high dose in the target, or a even lower dose coverage, in the case of dose distributions without a specifically high target dose.

In addition to the evaluation criteria evaluated above, the Avg modality in addition has the advantage of a scan taken during normal breathing. Avoiding the instruction of the patient's breathing pattern might lower the chance of an unnatural breathing cycle that is difficult to reconstruct. Especially when a target moves irregularly, there has previously been noted an underrepresented target motion using MIP [36]. Because of this, a reduction in ITV volume using Avg instead of St could be proposed, as the geometrical uncertainties could be considered as smaller. This would result in a higher score in coverage ratios for the Avg modalities.

None of the treatment plans included additional arcs or coplanar fields, which might would have improved the treatment's robustness or target coverage [38]. The decision of avoiding these setup possibilities was based on the fact that treatment efficiency is important, because patients with high morbidity are not able to endure long treatment sessions [9]. Using the Original 3D-CRT treatments as a reference of today's treatment, the treatment plans still gives satisfactory results.

It should be noted that the planning procedures related to the normalisation of dose is different for the VMAT and 3D-CRT treatments. The use of another dose criteria of the Original plans might have resulted in a dose distribution closer to the VMAT results. However, as the main

purpose of including the Original plans was to have a reference regarding the treatment utilised at HUH today, there have been no further optimisation or attempt of improvement of the Original plans. Nevertheless, as all treatment plans, both VMAT and the 3D-CRT, have been approved by a responsible oncologist, the treatments are regarded as fully comparable.

Regarding the box-plots, the reader should keep in mind that the basis of statistical analysis is limited, as only five patients were included in this study, and that the assumption of a gaussian distribution is rather untenable. The standard deviations should also be evaluated with this fact kept in mind, and preferably be regarded as a range measure.

Despite the distinguished well agreement between AAA and MC using the DO CT basis, the accumulated dose resulted in poorer tumour coverage than the other CT bases. This is the opposite of what was found by Wiant et al. [54]. The reason for these different evaluation results might be due to the fact that they calculated the dose using AAA, in addition to the use of simple phantom geometries instead of patients. In order to confirm this hypothesis additional experiments and commission of the MC system must by performed.

6   Conclusion

Compared to the conventional technique, VMAT results in lower dose to adjacent tissue, equivalent dose to contralateral lung and higher accumulated dose to the ITV. Regarding the different CT bases all treatment plans lead to accumulated doses with lower conformity index, less PTV covage and decreased mean dose to the ITV. The MID and AI bases were the ones with accumulated dose closest to the planned dose, wherein the tumours with medium or large size (relative to the tumours investigated) gave the most promising results. The density overwrite CT basis lead to similar AAA and MC dose distributions, but resulted in an accumulated dose deviating remarkably from the planned dose. Therefore, the DO CT basis is not to be recommended for the treatment planning of NSCLC.

The work performed in the project has established a solid optimal starting point for the clinical implementation of SBRT NSCLC FFF VMAT at Haukeland University Hospital. However, further development of the MC algorithm and automation of the treatment verification method for time reduction are required. The MCverify has the potential of being used as QA for future treatments, however it still requires more work to understand and correct the calculation before the method can be used clinically.

7   Future Progress

The MC algorithm utilised in this project is still only suitable for research and requires further developments and throughout testing before clinical use.

The *QUASAR phantom*(Modus Medical Devices, London, Canada) is a phantom that simulates tumour motion due to breathing. Intentionally, we wanted to include measurements on that phantom in this report, as a further investigation of the accumulation process. However, due to time-limitations, those measurements are left for a later occasion.

Further improvements of the project can be to investigate SBRT cases with the respective breathing curve or another more specific respiratory weighting. Also, as this project only include five patients, additional cases could profitably be investigated for more trustworthy and general statistics.

Regarding side effects, a separate delineation of the diaphragm could enlighten the impact of tumour motion in the inferior part of the lung. In the treatment plans evaluated in this project, the diaphragm is often included in the Costa structure or not included at all.

The deviation between the dose simulations of AAA and the *Delta4* measurements are still under further investigation.

8 Appendix

8.1 Approvals

The REK (Regional Committees for Medical and Health Research Ethics) did not find this project obliged to apply for the REK approval, as it is considered as a quality assurance project.

8.2　Specifications of the CT Images

Table 8.1 lists additional information about the delineation and fixed densities of all the tumours used in this investigation.

Table 8.1: Details of the PTV sizes and the fixed density values of the ITVs and PTV margins using the density overwrite (DO) techniqe. The resulting Hounsfield units of the fixed densities are calculated automaticly by *Eclipse*. There are two different volumes of the PTVs, as the 4D CT images used for delineation of the AvgCT basis have a different resolution compared to the regular CT images.

Case	PTV [cm^3]	DO [cm^3]	DO [HU]
sbrt01	St./MinDo: 73.03	ITV: 1.0292	ITV: 28
	Avg: 71.82	PTV m.: 0.5949	PTV m.: -399
sbrt05	St./MinDo: 28.49	ITV: 1.0135	ITV: 13
	Avg: 28.23	PTV m.: 0.5504	PTV m.: -437
sbrt11	St./MinDo: 30.20	ITV: 0.9958	ITV: -8
	Avg: 30.28	PTV m.: 0.7930	PTV m.: -230
sbrt12	St./MinDo: 23.90	ITV: 0.9932	ITV: -13
	Avg: 23.97	PTV m.: 0.5340	PTV m.: -451
sbrt13	St./MinDo: 117.92	ITV: 1.0600	ITV: 64
	Avg: 117.51	PTV m.: 0.6289	PTV m.: -370
sbrt14	St./MinDo: 9.84	ITV: 0.9917	ITV: -16
	Avg: 9.29	PTV m.: 0.5563	PTV m.: -432

8.3   Treatment Planning Guidelines

Figure 8.1 and 8.2 shows the guidelines for the treatment planning of 54 Gy and 55 Gy prescription doses, respectively, where the size of the PTV has an impact on the criteria. In addition, the dose to the contra lateral lung where specifically monitored by the volume receiving 5 Gy, V_{5Gy}. The guideline maximum limit of V_{5Gy} is not clear, but was recommended by VU University Medival Center Amsterdam to be maximum 10% if unavoidable, but preferable less than 5%. Only the structures included in the original treatment plan were taken into consideration.

Prescription dose: 54 Gy
Fractionation: 3 x 18 Gy
Volume PTV: 0-20 cm^3

	Criterium
$R_{100\%}$	< 1.25
$R_{50\%}$	< 9
D_{2cm} (%)	< 70
Lungs-ITV: $V_{20\,Gy}$ (%)	< 6
Costa	$V_{30\,Gy}$ < 30 cm^3

	(Gy/fr)
Spinal Cord	5,0-6,0
Oesophagus	8.5 Gy, D(5 cm^3) < 5,9 Gy
Heart	10 Gy, <15 cm^3 8 Gy
Skin	<7 Gy
Aorta	<10 cm3 13 Gy, pt. max. 15 Gy
Vena Cava	<10 cm3 13 Gy, pt. max. 15 Gy
Brachial Plexus	8
Trachea	10,0
Proximal Bronchial Tree	10
Ventricle/small intestine	<10 cm^3 7 Gy, pt. max. 8 Gy

(a)

Prescription dose: 54 Gy
Fractionation: 3 x 18 Gy
Volume PTV: 20-40 cm^3

	Criterium
$R_{100\%}$	< 1.15
$R_{50\%}$	< 12
D_{2cm} (%)	< 65
Lungs-ITV: $V_{20\,Gy}$ (%)	< 5
Costa	$V_{30\,Gy}$ < 30 cm^3

	(Gy/fr)
Spinal Cord	5,0-6,0
Oesophagus	8.5 Gy, D(5 cm^3) < 5,9 Gy
Heart	10 Gy, <15 cm^3 8 Gy
Skin	<7 Gy
Aorta	<10 cm3 13 Gy, pt. max. 15 Gy
Vena Cava	<10 cm3 13 Gy, pt. max. 15 Gy
Brachial Plexus	8
Trachea	10,0
Proximal Bronchial Tree	10
Ventricle/small intestine	<10 cm^3 7 Gy, pt. max. 8 Gy

(b)

Figure 8.1: Dose criteria guidelines used when planning patient (a) sbrt14 and (b) sbrt05 and sbrt12.

Prescription dose: 55 Gy **Fractionation: 5 x 11 Gy** **Volume PTV: 20-40 cm^3**	
	Criterium
$R_{100\%}$	< 1.15
$R_{50\%}$	< 9
D_{2cm} (%)	< 70
Lungs-ITV: $V_{20\,Gy}$ (%)	< 6
Costa	$V_{30\,Gy}$ < 30 cm^3
	(Gy/fr)
Spinal Cord	4,5-5,0
Oesophagus	6,5
Heart	7,5
Skin	6,4
Aorta	$V_{9,4\,Gy}$ <10 cm^3, pt. max. 105%
Vena Cava	$V_{9,4\,Gy}$ <10 cm^3, pt. max. 105%
Brachial Plexus	6
Trachea	7,5
Proximal Bronchial Tree	7,5
Ventricle/small intestine	5

Prescription dose: 55 Gy **Fractionation: 5 x 11 Gy** **Volume PTV: > 40 cm^3**	
	Criterium
$R_{100\%}$	< 1.10
$R_{50\%}$	< 6
D_{2cm} (%)	< 70
Lungs-ITV: $V_{20\,Gy}$ (%)	< 10
Costa	$V_{30\,Gy}$ < 30 cm^3
	(Gy/fr)
Spinal Cord	4,5-5,0
Oesophagus	6,5
Heart	7,5
Skin	6,4
Aorta	$V_{9,4\,Gy}$ <10 cm^3, pt. max. 105%
Vena Cava	$V_{9,4\,Gy}$ <10 cm^3, pt. max. 105%
Brachial Plexus	6
Trachea	7,5
Proximal Bronchial Tree	7,5
Ventricle/small intestine	5

(a)   **(b)**

Figure 8.2: Dose criteria guidelines used when planning patient (a) sbrt11 and (b) sbrt01 and sbrt13.

The MU values of all the treatments are given in table 8.2. In general, the VMAT plans have much higher MU values than the original plans. There are no strict upper limit of the MU values in the guidelines at HUS, however, as low MU values as possible are preferable.

Table 8.2: MU values of all treatments given in MU/Gy, rounded to the closest integer.

		10MV			**6MV**		
	Original	**Avg**	**DO**	**Static**	**Avg**	**DO**	**Static**
sbrt01	32	66	56	62	52	51	52
sbrt05	56	103	112	123	91	84	88
sbrt11	39	57	57	60	52	50	50
sbrt12	59	84	77	79	89	64	75
sbrt13	32	50	59	57	54	51	45
sbrt14	68	107	100	126	111	107	126

8.4 Phase Space simulation settings

Table 8.3: Phase Space simulation settings

Global ECUT	0.521
Global PCUT	0.01
Global SMAX	5
ESTEPE	0.25
XIMAX	0.5
Boundary crossing algorithm	PRESTA-I
Skin depth for BCA	0
Electron-step algorithm	PRESTA-I
Spin effects	On
Brems angular sampling	Simple
Brems cross sections	BH
Bound Compton scattering	Off
Compton cross sections	default
Pair angular sampling	Simple
Pair cross sections	BH
Photoelectron angular sampling	Off
Rayleigh scattering	Off
Atomic relaxations	Off
Electron impact ionization	Off
Photon cross sections	xcom
Photon cross-sections output	Off

8.5   Description of the Box Plot MATLAB function

All box plots in this project are calculated by MATLAB R2014a [4].

The box plot function sets the central red mark as the median, while the edges of the box are the 25th and 75th percentiles. The maximum whisker length (w) is by default set to 1.5 and extends to the most extreme data value that is not an outlier. Points are defined as outliers if they are larger than $q_3 + w(q_3 - q_1)$ or smaller than $q_1 - w(q_3 - q_1)$, where q_1 and q_3 are the 25th and 75th percentiles, respectively.

8.6   Sum plans
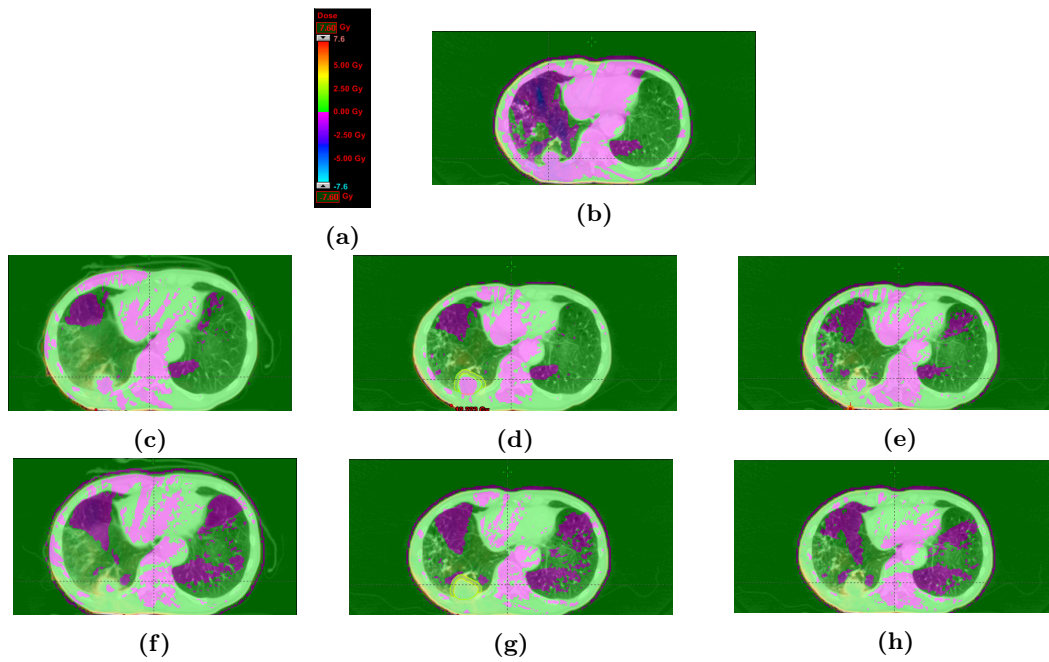
Figure 8.3: Sbrt01: Summed plans, where the Eclipse simulation is subtracted from the MC simulation. The colour scale is ranging from +10% to −10% of the maximum dose of the original plan. (a) Illustrating colour scale (varying slightly for each sum plan), (b) Original plan, (c) 6MV Avg, (d) 6MV DO, (e) 6MV St, (f) 10MV Avg, (g) 10MV DO, and (h) 10MV St.
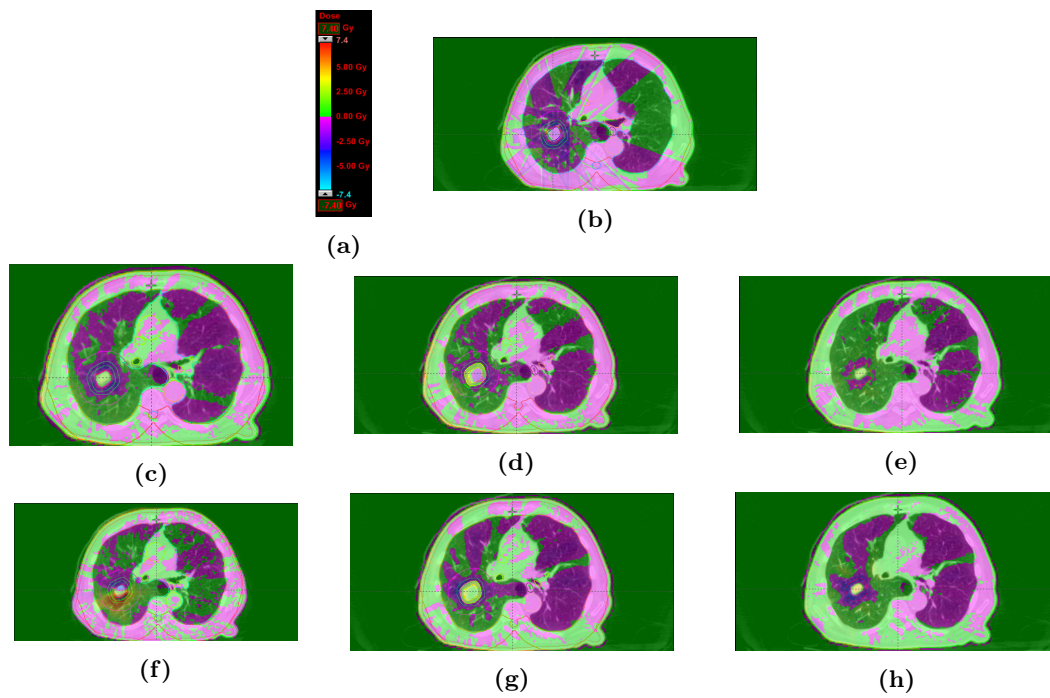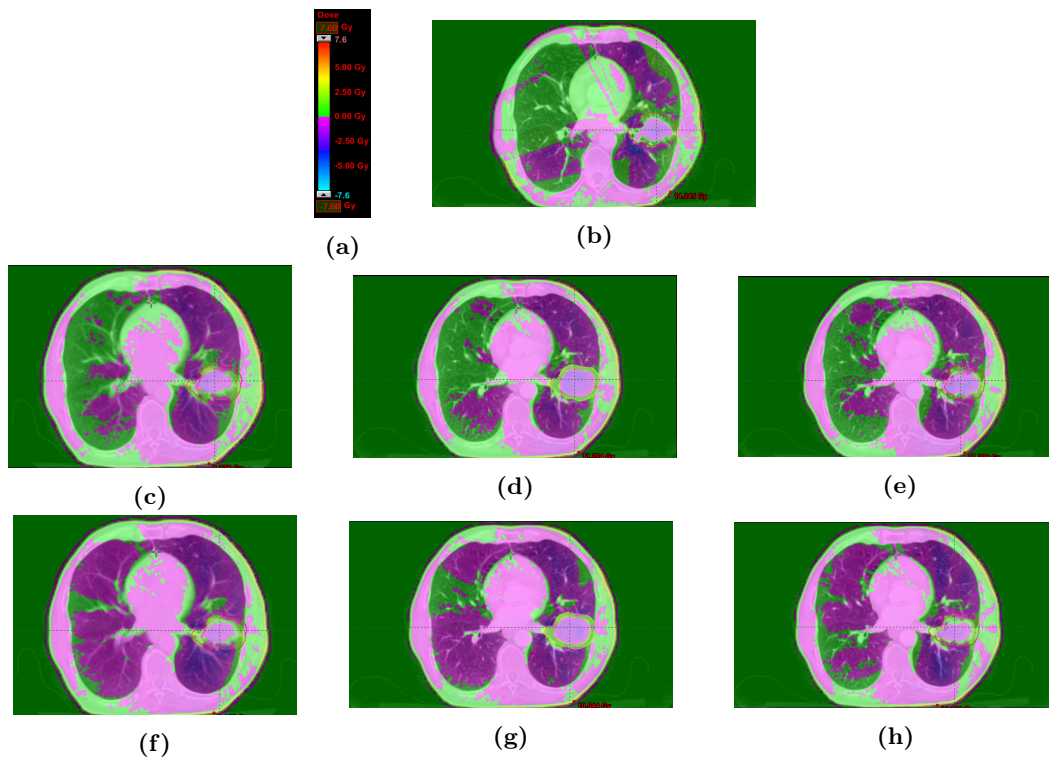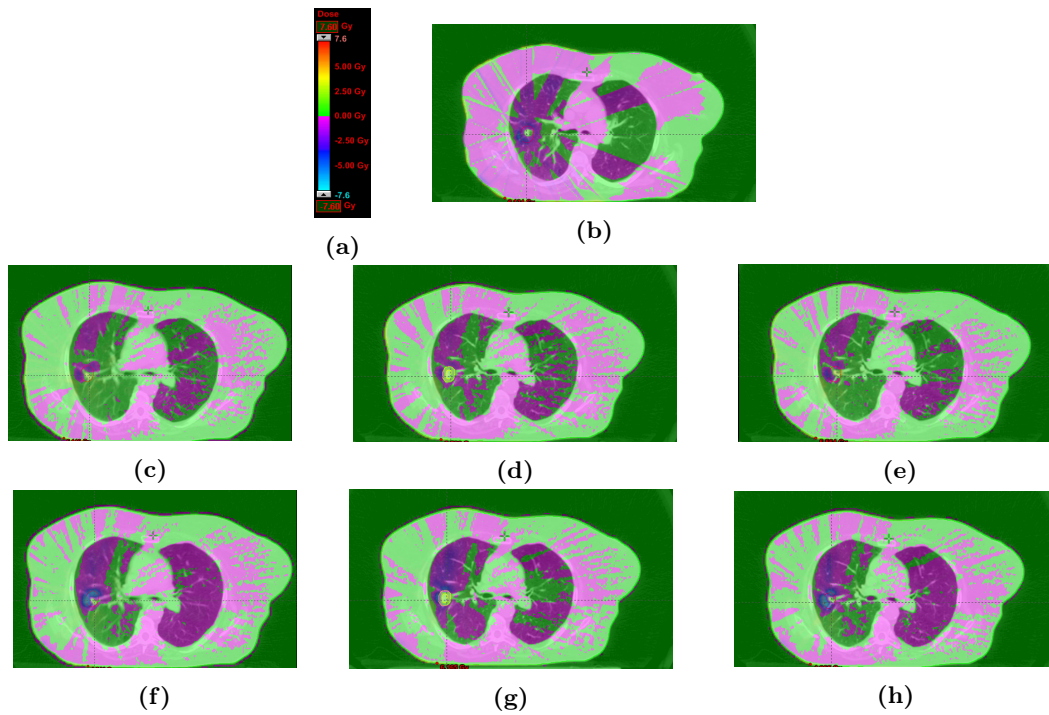
Figure 8.4: Sbrt05: Summed plans, where the Eclipse simulation is subtracted from the MC simulation. The colour scale is ranging from +10% to −10% of the maximum dose of the original plan. In the case of CT image colour, the dose difference is larger than 10%. (a) Illustrating colour scale (varying slightly for each sum plan), (b) Original plan, (c) 6MV Avg, (d) 6MV DO, (e) 6MV St, (f) 10MV Avg, (g) 10MV DO, and (h) 10MV St.

Figure 8.5: Sbrt13: Summed plans, where the Eclipse simulation is subtracted from the MC simulation. The colour scale is ranging from +10% to −10% of the maximum dose of the original plan. (a) Illustrating colour scale (varying slightly for each sum plan), (b) Original plan, (c) 6MV Avg, (d) 6MV DO, (e) 6MV St, (f) 10MV Avg, (g) 10MV DO, and (h) 10MV St.

Figure 8.6: Sbrt14: Summed plans, where the Eclipse simulation is subtracted from the MC simulation. The colour scale is ranging from +10% to −10% of the maximum dose of the original plan. In the case of CT image colour, the dose difference is larger than 10%. (a) Illustrating colour scale (varying slightly for each sum plan), (b) Original plan, (c) 6MV Avg, (d) 6MV DO, (e) 6MV St, (f) 10MV Avg, (g) 10MV DO, and (h) 10MV St.

8.7   Accumulated dose distributions
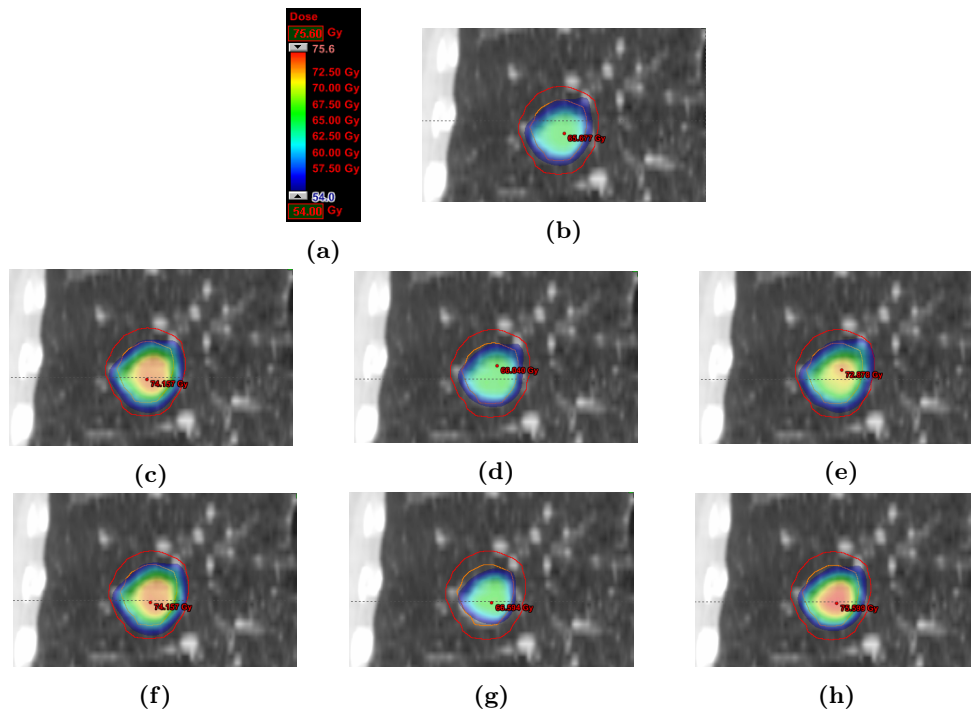
Figure 8.7: Sbrt05: Accumulated dose. (a) Colour scale, ranging from prescribed dose (54.0 Gy) to the maximum optimisation value of 140% (75.6 Gy). (b) Original plan, (c) 6MV Avg, (d) 6MV DO, (e) 6MV St, (f) 10MV Avg, (g) 10MV DO, and (h) 10MV St.
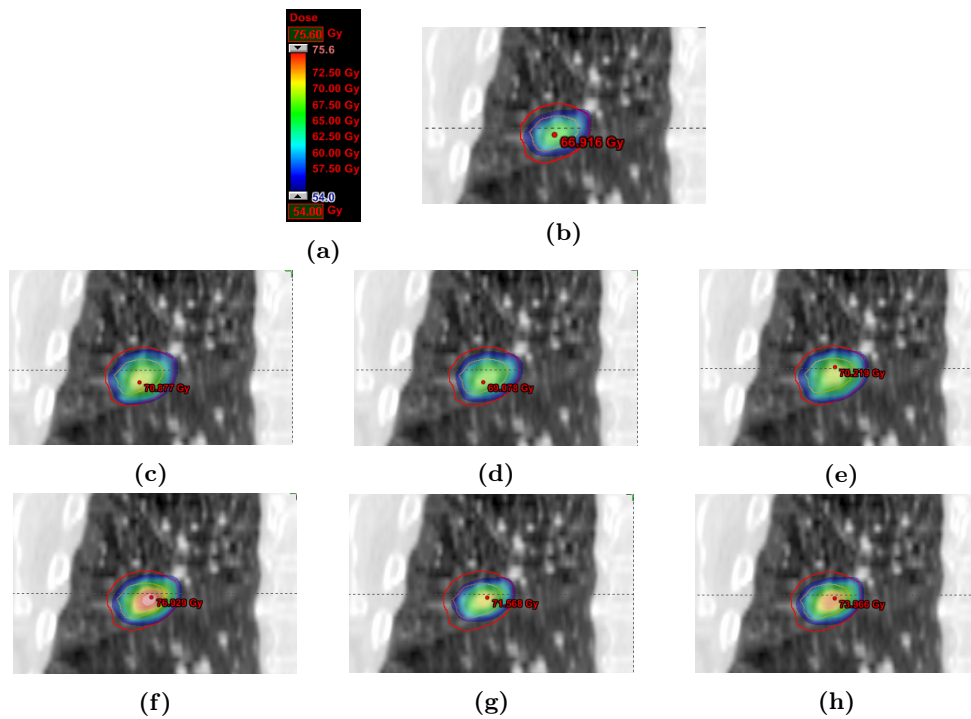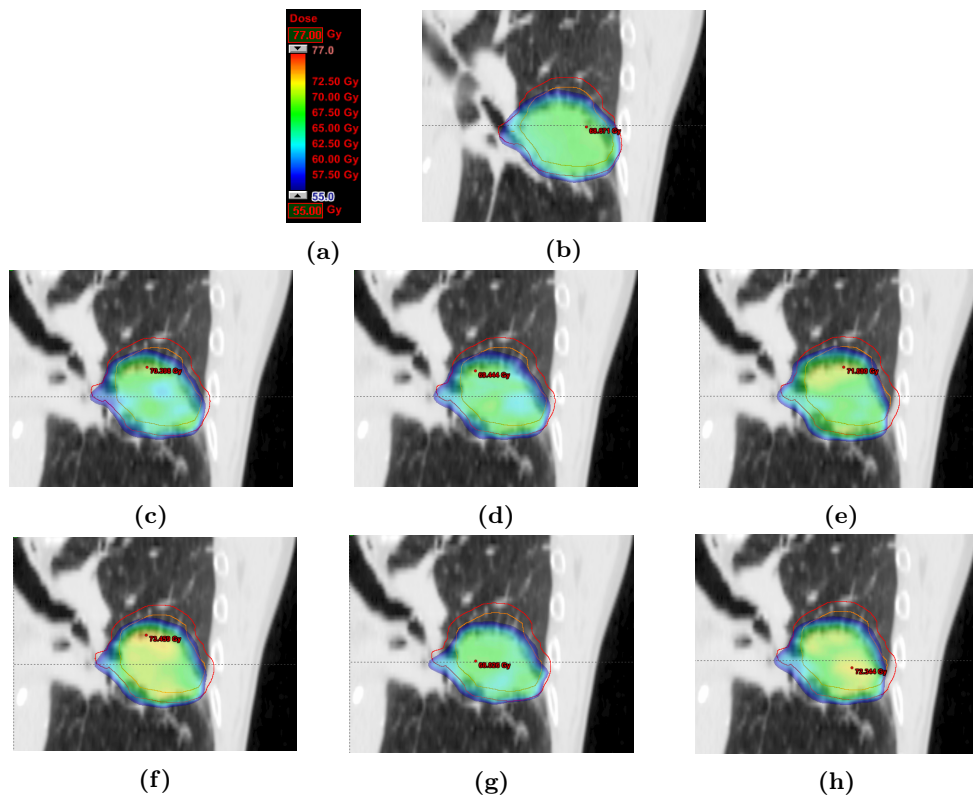
Figure 8.8: Sbrt12: Accumulated dose. (a) Colour scale, ranging from prescribed dose (54.0 Gy) to the maximum optimisation value of 140% (75.6 Gy). (b) Original plan, (c) 6MV Avg, (d) 6MV DO, (e) 6MV St, (f) 10MV Avg, (g) 10MV DO, and (h) 10MV St.
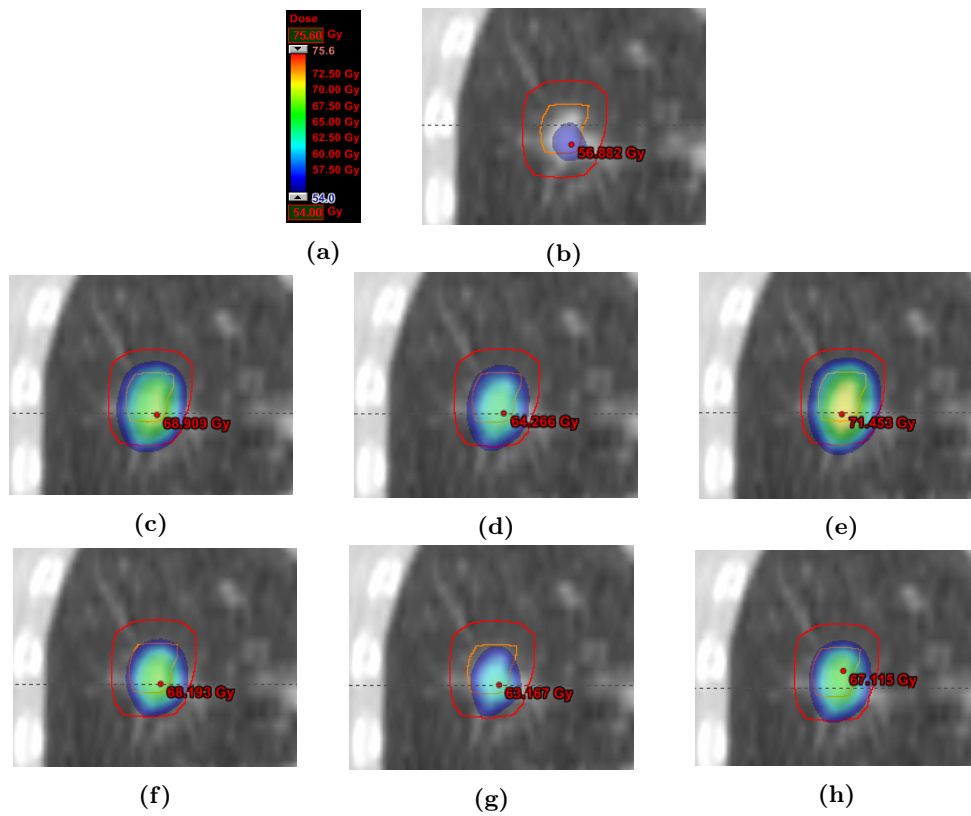
Figure 8.9: Sbrt13: Accumulated dose. (a) Colour scale, ranging from prescribed dose (55.0 Gy) to the maximum optimisation value of 140% (77.0 Gy). (b) Original plan, (c) 6MV Avg, (d) 6MV DO, (e) 6MV St, (f) 10MV Avg, (g) 10MV DO, and (h) 10MV St.

Figure 8.10: Sbrt14: Accumulated dose. (a) Colour scale, ranging from prescribed dose (55.0 Gy) to the maximum optimisation value of 140% (77.0 Gy). (b) Original plan, (c) 6MV Avg, (d) 6MV DO, (e) 6MV St, (f) 10MV Avg, (g) 10MV DO, and (h) 10MV St.
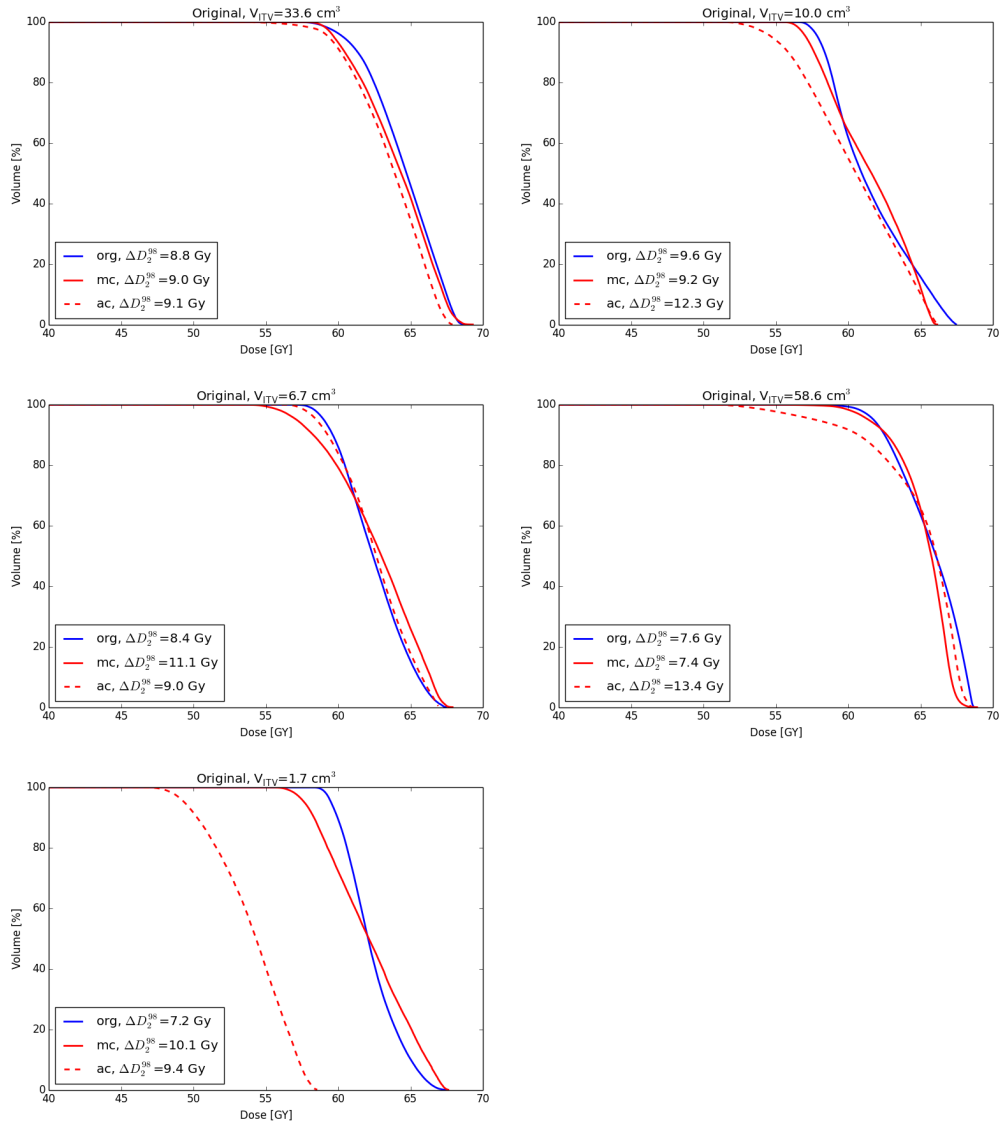
8.8 DVH of the ITV coverage

Figure 8.11: Relative DVHs of the ITV structure for all Original treatments. The blue line (org) is calculated by AAA and the red line (mc) by MC. The dashed line (ac) is the result from the accumulation of MC dose.
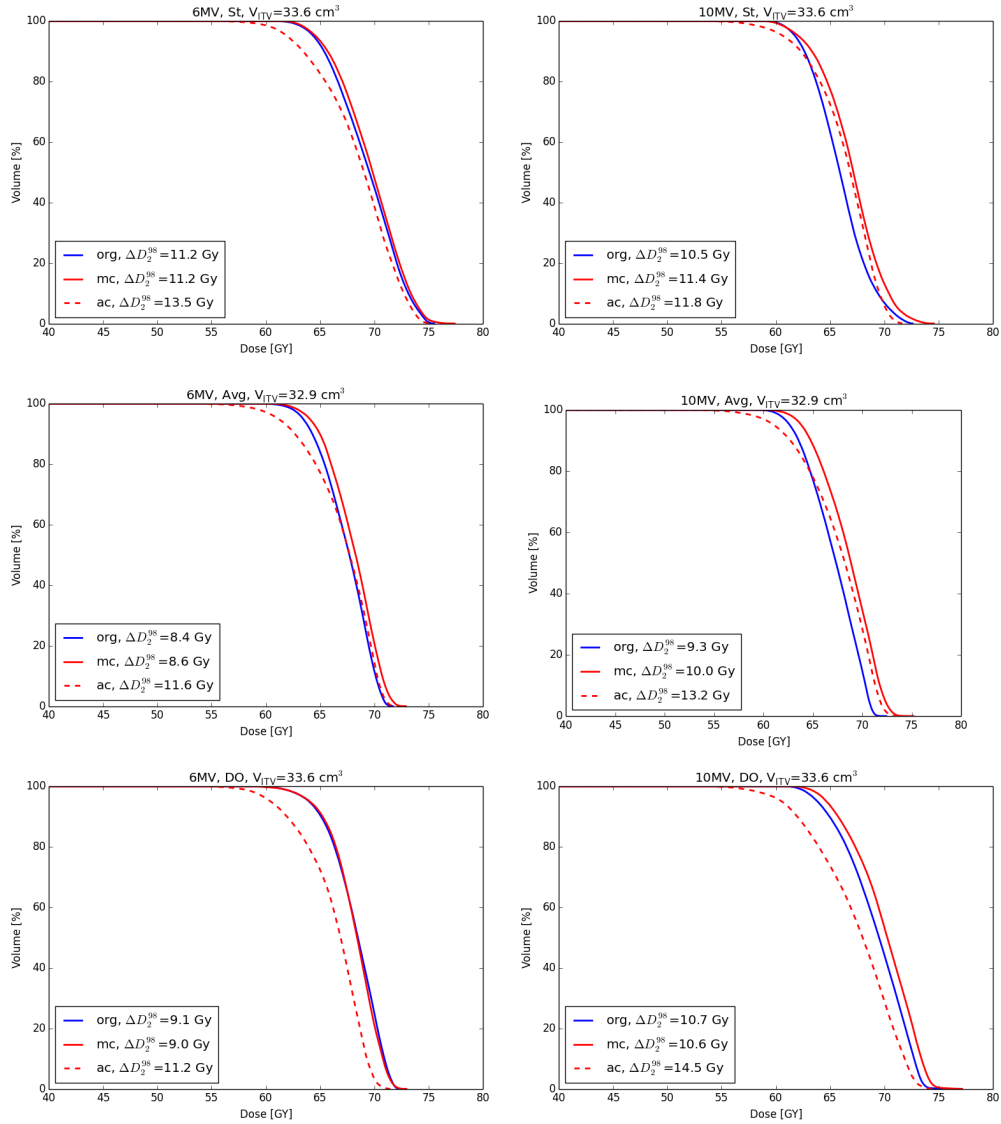
Figure 8.12: Relative DVHs of the ITV structure for all sbrt01 VMAT treatments. The blue line (org) is calculated by AAA and the red line (mc) by MC. The dashed line (ac) is the result from the accumulation of MC dose. The volume of the Avg structures deviates with at small fraction as these are calculated on the CT0 CT set.
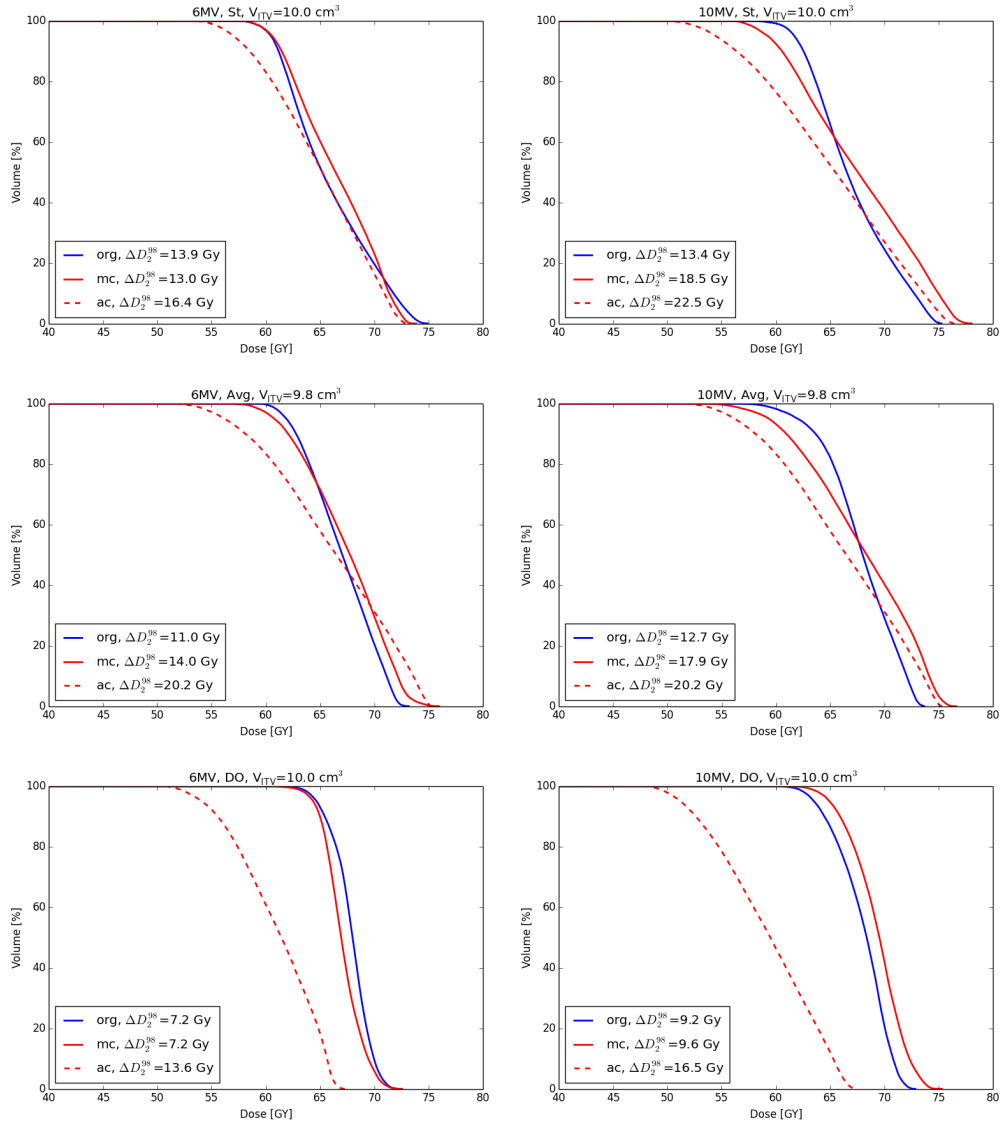
Figure 8.13: Relative DVHs of the ITV structure for all sbrt05 VMAT treatments. The blue line (org) is calculated by AAA and the red line (mc) by MC. The dashed line (ac) is the result from the accumulation of MC dose. The volume of the Avg structures deviates with at small fraction as these are calculated on the CT0 CT set.

Figure 8.14: Relative DVHs of the ITV structure for all sbrt12 VMAT treatments. The blue line (org) is calculated by AAA and the red line (mc) by MC. The dashed line (ac) is the result from the accumulation of MC dose. The volume of the Avg structures deviates with at small fraction as these are calculated on the CT0 CT set.
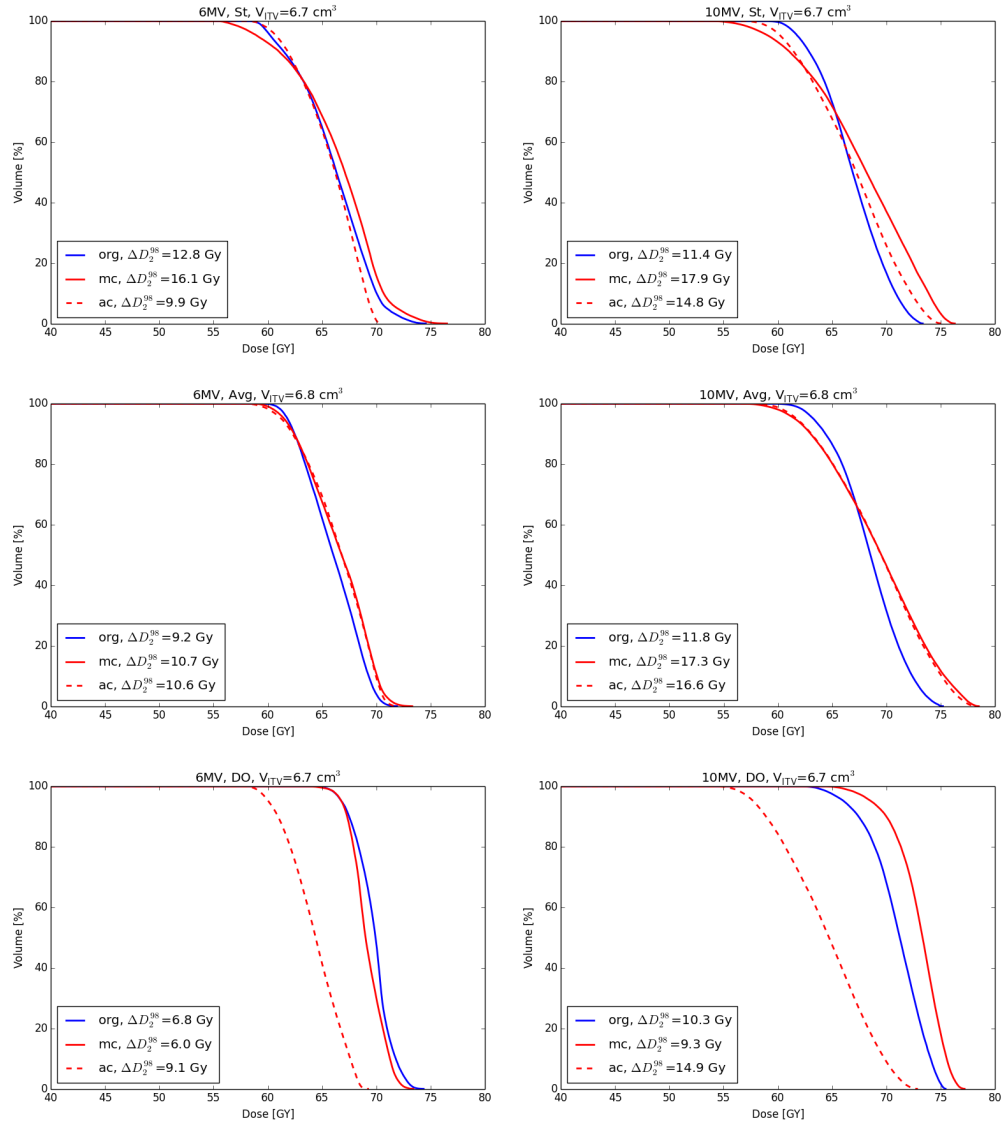
Figure 8.15: Relative DVHs of the ITV structure for all sbrt13 VMAT treatments. The blue line (org) is calculated by AAA and the red line (mc) by MC. The dashed line (ac) is the result from the accumulation of MC dose. The volume of the Avg structures deviates with at small fraction as these are calculated on the CT0 CT set.
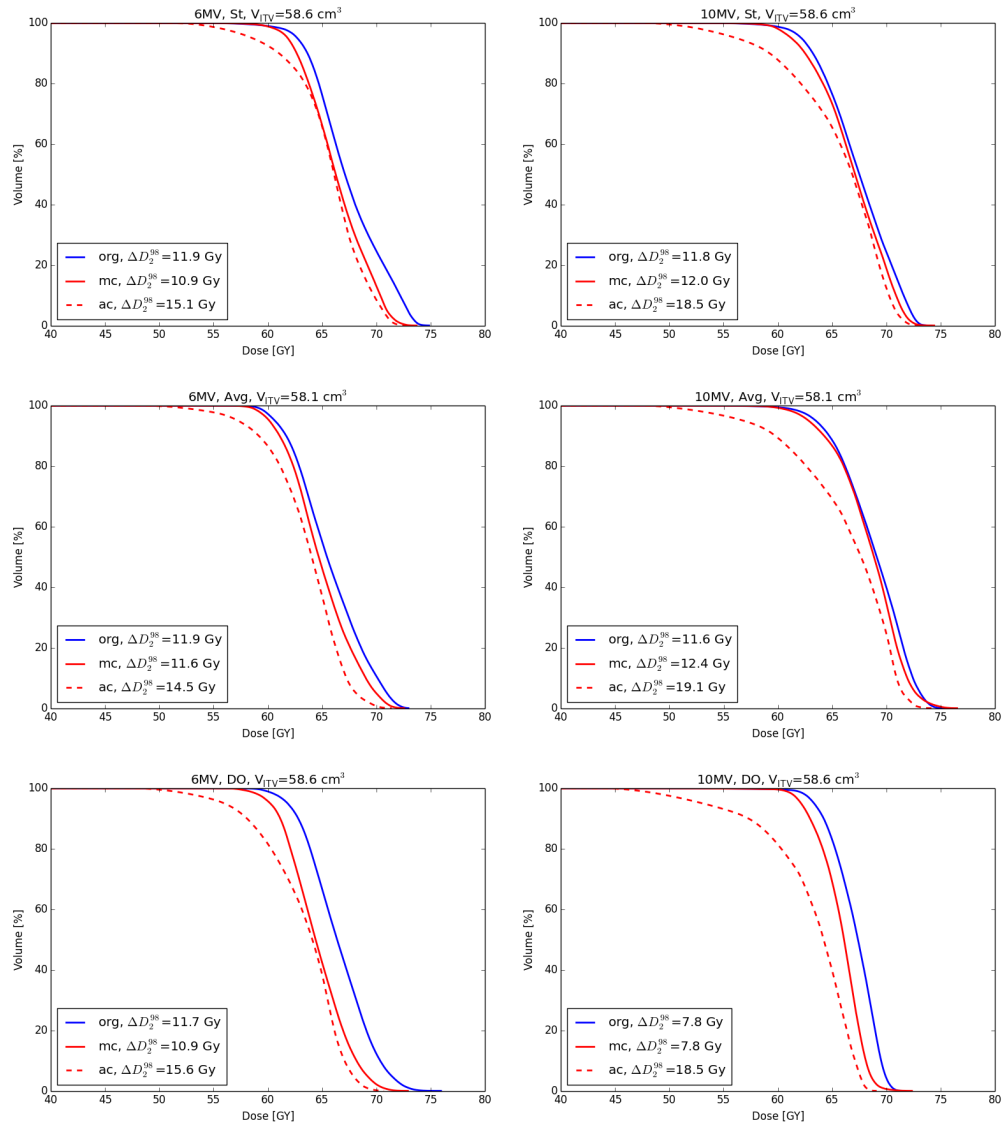
Figure 8.16: Relative DVHs of the ITV structure for all sbrt14 VMAT treatments. The blue line (org) is calculated by AAA and the red line (mc) by MC. The dashed line (ac) is the result from the accumulation of MC dose. The volume of the Avg structures deviates with at small fraction as these are calculated on the CT0 CT set.
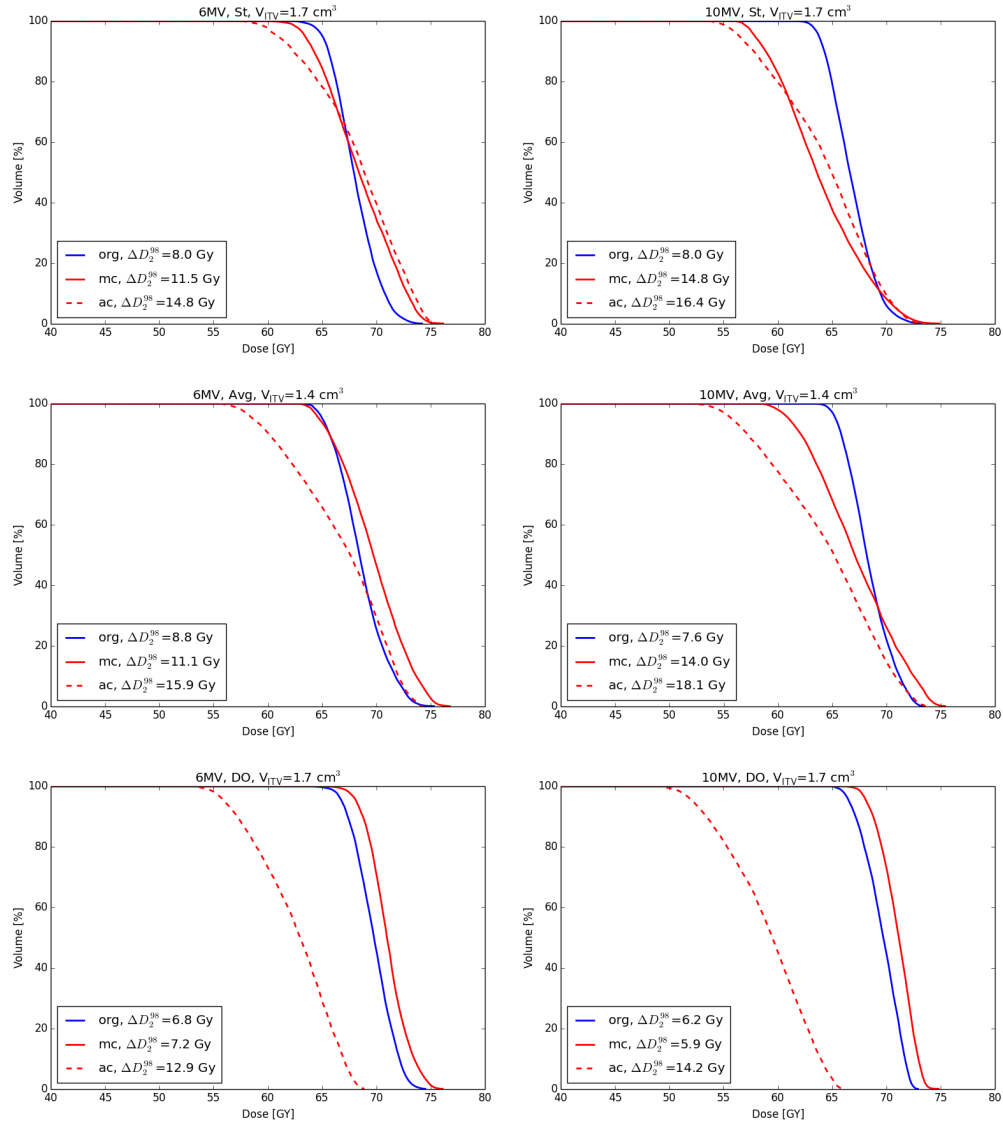
Bibliography

[1] *Python* official website. `https://www.python.org`. Accessed: 2015-22-06.

[2] UpToDate Overview of Mechanical Ventilation. `http://www.uptodate.com/contents/overview-of-mechanical-ventilation?source=machineLearning&search=normal+respiratory+cycle&selectedTitle=3$%$7E150&sectionRank=4&anchor=H24#H24`. Accessed: 2015-05-05.

[3] Inkscape, Copyright 2014 Inkscape Developers, GNU General Public License.

[4] MATLAB R2014a, February 11, 2014.

[5] L. R. Aarup, A. E. Nahum, C. Zacharatou, T. Juhler-Nøttrup, T. Knöös, H. Nyström, L. Specht, E. Wieslander, and S. S. Korreman. The effect of different lung densities on the accuracy of various radiotherapy dose calculation methods: Implications for tumour coverage. *Radiotherapy and Oncology*, 91(3):405–414, 2009.

[6] P. Andreo. Monte Carlo techniques in medical radiation physics. *Physics in Medicine and Biology*, 36(7):861, 1991.

[7] T. Bortfeld, K. Jokivarsi, M. Goitein, J. Kung, and S. B. Jiang. Effects of intra-fraction motion on IMRT dose delivery: Statistical analysis and simulation. *Physics in Medicine and Biology*, 47(13):2203–2220, 2002.

[8] T. Bortfeld, R. Schmidt-Ullrich, W. Neve, and D. E. Wazer. *Image-Guided IMRT*. Springer Berlin Heidelberg, Berlin, Heidelberg, 2006.

[9] J. D. Bradley, A. N. Nofal, I. M. El Naqa, W. Lu, J. Liu, J. Hubenschmidt, D. A. Low, R. E. Drzymala, and D. Khullar. Comparison of helical, maximum intensity projection (MIP), and averaged intensity (AI) 4D CT imaging for stereotactic body radiation therapy (SBRT) planning in lung cancer. *Radiotherapy and Oncology*, 81(3):264–268, 2006.

[10] J. Cashmore, M. Ramtohul, and D. Ford. Lowering whole-body radiation doses in pediatric intensity-modulated radiotherapy through the use of unflattened photon beams. *International Journal of Radiation Oncology Biology Physics*, 80(4):1220–1227, 2011.

[11] S. H. Cho and S. Krishnan. *Cancer nanotechnology: principles and applications in radiation oncology*. Taylor & Francis, Boca Raton, 2013.

[12] J. Deng, T. Pawlicki, Y. Chen, J. Li, S. B. Jiang, and C. M. Ma. The MLC tongue-and-groove effect on IMRT dose distributions. *Physics in Medicine and Biology*, 46(4):1039–1060, 2001.

[13] B. Disher. The Impact of Lateral Electron Disequilibrium on Stereotactic Body Radiation Therapy of Lung Cancer. *University of Western Ontario - Electronic Thesis and Dissertation Repository, Paper 1517*, 2013.

[14] O. S. Dohm. Monte-Carlo simulation of small field dosimetry in radiotherapy with high-energy photons. *PhD thesis, Eberhard Karls Universität Tübingen*, 2005.

[15] M. Fippel. Fast Monte Carlo dose calculation for photon beams based on the VMC electron algorithm. *Medical Physics*, 26(8):1466–1475, 1999.

[16] D. Georg, T. Knöös, and B. McClean. Current status and future perspective of flattening filter free photon beams. *Medical Physics*, 38(3):1280–1293, 2011.

[17] M. C. Han, Y. S. Yeom, C. H. Kim, S. Kim, and J. W. Sohn. New approach based on tetrahedral-mesh geometry for accurate 4D Monte Carlo patient-dose calculation. *Physics in Medicine and Biology*, 60(4):1601–1612, 2015.

[18] Philips Healthcare. *Respiratory motion management for CT (white paper)*. Koninklijke Philips Electronics N.V., printed in The Netherlands, 2013.

[19] I. Kawrakow and DW. Rogers. TheEGSnrc code system: Monte Carlo simulation of electron and photon transport. *Technical report PIRS-701. Ottawa: NRCC*, 2000.

[20] I. Kawrakow and B. R. B. Walters. Efficient photon beam dose calculations using DOSXYZnrc with BEAMnrc. *Medical Physics*, 33(8):3046–3056, 2006.

[21] F. M. Khan. *The physics of radiation therapy*. Lippincott Williams & Wilkins, Philadelphia, 2003. 3rd ed.

[22] S. G. Levernes. *Volum og doser i ekstern stråleterapi: definisjoner og anbefalinger*, volume 2012:9. Statens strålevern, Østerås, 2012.

[23] S. S. Lo, B. S. Teh, J. J. Lu, and T. E. Schefter. *Stereotactic Body Radiation Therapy*. Springer Berlin Heidelberg, Berlin, Heidelberg, 2013.

[24] D. A. Low, W. B. Harms, S. Mutic, and J. A. Purdy. A technique for the quantitative evaluation of dose distributions. *Medical Physics*, 25(5):656–661, 1998.

[25] T. R. Mackie, E. El-Khatib, J. Battista, J. Scrimger, J. Van Dyk, and J. R. Cunningham. Lung dose corrections for 6- and 15-MV x rays. *Medical Physics*, 12(3):327–332, 1985.

[26] P. Mayles, A. E. Nahum, and J. Rosenwald. *Handbook of radiotherapy physics: theory and practice*. Taylor & Francis, New York, 2007.

[27] H. G. Menzel. ICRU Report 83, Prescribing, Recording, and Reporting Photon-Beam Intensity-Modulated Radiation Therapy (IMRT). *Journal of the ICRU*, 10(1):1–106, 2010.

[28] Ditte Sloth Møller, Azza Ahmed Khalil, Marianne Marquard Knap, and Lone Hoffmann. Adaptive radiotherapy of lung cancer patients with pleural effusion or atelectasis. *Radiotherapy and Oncology*, 110(3):517–522, 2014.

[29] J. J. Ojala, M. K. Kapanen, S. J. Hyödynmaa, T. K. Wigren, and M. A. Pitkänen. Performance of dose calculation algorithms from three generations in lung sbrt: Comparison with full Monte Carlo-based dose distributions. *Journal of Applied Clinical Medical Physics*, 15(2):4–18, 2014.

[30] C. L. Ong, M. Dahele, B. J. Slotman, and W. F. A. R. Verbakel. Dosimetric impact of the interplay effect during stereotactic lung radiation therapy delivery using flattening filter-free beams and volumetric modulated arc therapy. *International Journal of Radiation Oncology Biology Physics*, 86(4):743–748, 2013.

[31] C. L. Ong, W. F. A. R. Verbakel, J. P. Cuijpers, B. J. Slotman, F. J. Lagerwaard, and S. Senan. Stereotactic radiotherapy for peripheral lung tumors: A comparison of volumetric modulated arc therapy with 3 other delivery techniques. *Radiotherapy and Oncology*, 97(3):437–442, 2010.

[32] C. L. Ong, W. F. A. R. Verbakel, M. Dahele, J. P. Cuijpers, B. J. Slotman, and S. Senan. Fast arc delivery for stereotactic body radiotherapy of vertebral and lung tumors. *International Journal of Radiation Oncology Biology Physics*, 83(1):e137–e143, 2012.

[33] K. Otto. Volumetric modulated arc therapy: IMRT in a single gantry arc. *Medical Physics*, 35(1):310–317, 2008.

[34] C. Ozhasoglu and M. J. Murphy. Issues in Respiratory Motion Compensation During External-Beam Radiotherapy. *International Journal of Radiation Oncology Biology Physics*, 52(5):1389–1399, 2002.

[35] I. Paddick. A simple scoring ratio to index the conformity of radiosurgical treatment plans. technical note. *Journal of Neurosurgery*, 93:219–222, 2000.

[36] K. Park, L. Huang, H. Gagne, and L. Papiez. Do Maximum Intensity Projection Images Truly Capture Tumor Motion? *International Journal of Radiation Oncology Biology Physics*, 73(2):618–625, 2009.

[37] N. Reynaert, S. van der Marck, and D. Schaart. Monte Carlo Treatment Planning — An Introduction, Nederlandse Commissie Voor Stralingsdosimetrie. *Report 16 of the Netherlands Commission on Radiation Dosimetry Netherlands, Commission on Radiation Dosimetry Subcommission Monte Carlo Treatment Planning.*, 2006.

[38] T. A. Ritter, D. Owen, C. M. Brooks, and M. H. Stenmark. Treatment planning for sbrt using automated field delivery: A case study. *Medical Dosimetry*, 40(1):44–46, 2015.

[39] W. Schlegel, T. Bortfeld, and A. Grosu. *New Technologies in Radiation Oncology*. Springer Berlin Heidelberg, Berlin, Heidelberg, 2006.

[40] M. L. Schmidt, L. Hoffmann, M. Kandi, D. S. Moller, and P. R. Poulsen. Dosimetric impact of respiratory motion, interfraction baseline shifts, and anatomical changes in radiotherapy of non-small cell lung cancer. *Acta Oncologica*, 52(7):1490–1496, 2013.

[41] J. Seco and F. Verhaegen. *Monte Carlo Techniques in Radiation Therapy*. Taylor & Francis, Boca Raton, Fla., 2013.

[42] J. Sievinen, W. Ulmer, and W. Kaissl. AAA photon dose calculation model in eclipse. *Varian Medical Systems*, 2005.

[43] M. Sikora, J. Muzik, M. Söhn, M. Weinmann, and M. Alber. Monte Carlo vs. Pencil Beam based optimization of stereotactic lung IMRT. *Radiation Oncology*, 4(1), 2009.

[44] M. P. Sikora. Virtual Source Modelling of Photon Beams for Monte Carlo Based Radiation Therapy Treatment Planning. *PhD thesis, Eberhard Karls Universität Tübingen*, 2005.

[45] B. W. Stewart and C. P. Wild. *World cancer report 2014*. International Agency for Research on Cancer, Lyon, France, 2014.

[46] M. Söhn, M. Birkner, Y. Chi, J. Wang, D. Yan, B. Berger, and M. Alber. Model-independent, multimodality deformable image registration by local matching of anatomical features and minimization of elastic energy. *Medical Physics*, 35(3):866–878, 2008.

[47] M. Söhn, M. Weinmann, and M. Alber. Intensity-Modulated Radiotherapy Optimization in a Quasi-Periodically Deforming Patient Model. *International Journal of Radiation Oncology Biology Physics*, 75(3):906–914, 2009.

[48] T. Teke, B. Gill, C. Duzenli, and I. A. Popescu. A Monte Carlo model of the Varian IGRT couch top for RapidArc QA. *Physics in Medicine and Biology*, 56(24):N295–N305, 2011.

[49] R. Timmerman, R. Paulus, J. Galvin, J. Michalski, W. Straube, J. Bradley, A. Fakiris, A. Bezjak, G. Videtic, D. Johnstone, J. Fowler, E. Gore, and H. Choy. Stereotactic body radiation therapy for inoperable early stage lung cancer. *JAMA - Journal of the American Medical Association*, 303(11):1070–1076, 2010.

[50] R. D. Timmerman, B. D. Kavanagh, L. C. Cho, L. Papiez, and L. Xing. Stereotactic body radiation therapy in multiple organ sites. *Journal of Clinical Oncology*, 25(8):947–952, 2007.

[51] R. W. M. Underberg, F. J. Lagerwaard, B. J. Slotman, J. P. Cuijpers, and S. Senan. Use of maximum intensity projections (MIP) for target volume generation in 4DCT scans for lung cancer. *International Journal of Radiation Oncology Biology Physics*, 63(1):253–260, 2005.

[52] W. F. A. R. Verbakel, S. Senan, J. P. Cuijpers, B. J. Slotman, and F. J. Lagerwaard. Rapid delivery of stereotactic radiotherapy for peripheral lung tumors using volumetric intensity-modulated arcs. *Radiotherapy and Oncology*, 93(1):122–124, 2009.

[53] E. Vásquez Osorio. *Improving Feature-based Non-rigid Registration for Applications in Radiotherapy*. Ph.d. thesis, 2012.

[54] D. Wiant, C. Vanderstraeten, J. Maurer, J. Pursley, J. Terrell, and B. J. Sintay. On the validity of density overrides for VMAT lung SBRT planning. *Medical Physics*, 41(8), 2014.

[55] A. B. Wolbarst, L. M. Chin, and G. K. Svensson. Optimization of radiation therapy: Integral-response of a model biological system. *International Journal of Radiation Oncology, Biology, Physics*, 8(10):1761–1769, 1982.

[56] J. W. H. Wolthaus, C. Schneider, J. J. Sonke, M. van Herk, J. S. A. Belderbos, M. M. G. Rossi, J. V. Lebesque, and E. M. F. Damen. Mid-ventilation CT scan construction from four-dimensional respiration-correlated CT scans for radiotherapy planning of lung cancer patients. *International Journal of Radiation Oncology Biology Physics*, 65(5):1560–1571, 2006.

[57] P. Zhang, G. D. Hugo, and D. Yan. Planning Study Comparison of Real-Time Target Tracking and Four-Dimensional Inverse Planning for Managing Patient Respiratory Motion. *International Journal of Radiation Oncology Biology Physics*, 72(4):1221–1227, 2008.